

**INTEGRATION OF MICRO-GAS CHROMATOGRAPHY SYSTEM  
FOR DETECTION OF VOLATILE ORGANIC COMPOUNDS**

A Dissertation  
Presented to  
The Academic Faculty

by

Milad Navaei

In Partial Fulfillment  
of the Requirements for the Degree  
Doctor of Philosophy in the  
G.W. Woodruff School of Mechanical Engineering

Georgia Institute of Technology  
August 2015

Copyright © August 2015 by Milad Navaei

**INTEGRATION OF MICRO-GAS CHROMATOGRAPHY SYSTEM  
FOR DETECTION OF VOLATILE ORGANIC COMPOUNDS**

Approved by:

Dr. Peter Hesketh, Advisor  
School of Mechanical Engineering  
*Georgia Institute of Technology*

Dr. Oliver Brand  
School of Electrical and Computer  
Engineering  
*Georgia Institute of Technology*

Dr. Mostafa Ghiaasiaan  
School of Mechanical Engineering,  
*Georgia Institute of Technology*

Dr. Albert Frazier  
School of Electrical and Computer  
Engineering,  
*Georgia Institute of Technology*

Dr. Todd Sulchek  
School of Mechanical Engineering  
*Georgia Institute of Technology*

Dr. Jean-Marie Dimandja  
School of Chemistry  
*Spelman College*

Date Approved: July 21<sup>th</sup> 2015

*To my parents  
Kamal, Farzaneh, for their love, endless support and encouragement.*

## **ACKNOWLEDGEMENTS**

I would like to express my sincere appreciation to my advisor, Dr. Peter Hesketh for his endless support and guidance during my studies. I am grateful for having him as my advisor for his insight and career advice. I would like to thank the committee members Dr. Oliver Brand, Bruno Frazer, Dr. Todd Sulchek, Dr. Mostafa Ghiaasiaan and special thanks to Dr. John Dimandja for providing valuable research advice and insightful comments for the improvement of work.

I would like to thank GTRI for supporting my PhD work through the IRAD program and Gary McMurray and Jie Xu for their continuous support and guidance, I would not have had the opportunity to learn and accomplish my project tasks without their support.

I am grateful for my friends, Ali Hemmati, Kipp Schoenwald, Yaser Bastani, Alireza Mahdavifar, Heather Turney, Heather Legget, and Dan Potter for your friendship and the great times we share together.

Finally, I would like to thank my family for their endless support and encouragement during my studies.

## TABLE OF CONTENTS

<b>ACKNOWLEDGEMENTS</b>	<b>IV</b>
<b>LIST OF TABLES</b>	<b>IX</b>
<b>LIST OF FIGURES</b>	<b>X</b>
<b>SUMMARY</b>	<b>XV</b>
<b>CHAPTER 1 INTRODUCTION AND BACKGROUND</b>	<b>1</b>
<b>1.1 Methods of pathogen and fungal detections</b>	<b>1</b>
<b>1.2 Gas Chromatography</b>	<b>5</b>
1.2.1 Elution Gas Chromatography	6
1.2.2 Injection Port.	7
1.2.3 Column	7
1.2.3.1 Stationary Phase	8
1.2.3.2 Column Heating Techniques	10
1.2.4 Detector	14
1.2.4.1 Flame Ion Detector (FID)	14
1.2.4.2 Thermal Conductivity Detector (TCD)	15
1.2.4.3 Electron Capture Detector	15
1.2.5 Overview of Miniature Gas Chromatography	16
<b>1.3 Proposed Solution: Development of a novel bonding method using eutectic- fusion bonding for micro-fabrication of all silicon GC column</b>	<b>22</b>

1.4	<b>Proposed Solution: integrating a novel Axial heating</b>	22
1.5	<b>Proposed Solution: integrating an Ultra-low power TCD sensor</b>	23
1.6	<b>Proposed Solution: Study the VOC Gases Released by <i>Armillaria</i></b>	23
<b>CHAPTER 2 COLUMN PERFORMANCE THEORY</b>		<b>25</b>
2.1	<b>Retention Time</b>	<b>25</b>
2.2	<b>Column Efficiency</b>	<b>27</b>
2.3	<b>Gas Flow in MEMS Channel</b>	<b>28</b>
2.4	<b>Maximum Column Efficiency</b>	<b>30</b>
2.4.1	Column width theoretical calculations	31
2.4.2	Column Length	32
2.5	<b>Final Design Considerations:</b>	<b>34</b>
<b>CHAPTER 3 PROCESS DEVELOPMENT OF ALL SILICON GC</b>		
<b>COLUMN</b>		<b>37</b>
3.1	<b>Introduction</b>	<b>38</b>
3.2	<b>Micro Fabrication Process of all Silicon GC column</b>	<b>40</b>
3.2.1	Nano Port Bonding Setup	46
3.2.2	Column Stationary Phase Coating	48
3.3	<b>Bond Quality Characterization</b>	<b>50</b>
3.3.1	SEM Imaging	50
3.3.2	Mechanical Shear Test	52
3.3.3	Chromatograph	55
3.3.4	Column Efficiency	56
3.4	<b>Summary and Conclusion</b>	<b>58</b>

<b>CHAPTER 4 : AXIAL HEATING DESIG</b>	<b>60</b>
<b>4.1 Introduction</b>	<b>61</b>
<b>4.2 Experimental Section</b>	<b>64</b>
4.2.1 Thermal Analysis and Computational Modeling	64
4.2.2 Current Device Fabrication and Characterization	68
4.2.2.1 Chip Fabrication	68
4.2.2.2 Stage Assembly	70
<b>4.3 Results and Discussion</b>	<b>70</b>
4.3.1 Computational Modeling	70
4.3.2 Heater characterization	73
4.3.3 Coefficient of Convection Characterization	75
4.3.4 Experimental Setup	77
<b>4.4 Column Performance Evaluation for Focusing of Wide Injections</b>	<b>81</b>
<b>4.5 Conclusions/Outlook</b>	<b>86</b>
<b>CHAPTER 5 THERMAL CONDUCTIVITY DETECTOR (TCD)</b>	<b>87</b>
<b>5.1 Introduction</b>	<b>87</b>
<b>5.2 Experimental Implementation of Micro-TCD in GC system</b>	<b>91</b>
5.2.1.1 Relation between TCD resistance change and flow rate	93
5.2.1.2 Relation between pressure and TCD response	94
5.2.1.3 TCD Level of Detection	95
5.2.2 TCD Response Compared to a Commercial FID Detector	97
<b>5.3 Summary</b>	<b>99</b>
<b>CHAPTER 6 DETECTION OF <i>ARMILLARIA</i></b>	<b>100</b>
<b>6.1 Introduction</b>	<b>100</b>

6.2	<i>Armillaria</i> Sample Preparation _____	101
6.3	Gas chromatography-mass Spectrometry (GC-MS) Sampling _____	101
6.4	Experimental setup: _____	104
6.5	System Integration _____	107
6.6	Summary: _____	109
<b>CHAPTER 7 CONCLUDING REMARKS _____</b>		<b>111</b>
7.1	Conclusions _____	111
7.2	Recommended future work _____	113
<b>APPENDIX A: WAFER PROCESING RUN SHEET FOR THE MEMS GC</b>		
<b>WAFERS _____</b>		<b>116</b>
<b>REFERENCES _____</b>		<b>117</b>

## LIST OF TABLES

Table 1-1: Different stationary coatings and their application .....	10
Table 1-2 MicroGC background Carrier Gas .....	21
Table 2-1: Average linear flow velocity for fixed parallel plates, circular tubes, and rectangle channels .....	29
Table 2-2: Van Deemter equation parameters .....	30
Table 2-3: Golay's Equation parameters for the MEMS GC system .....	34
Table 2-4: Column properties for the different column lengths .....	36
Table 3-1: Etching Rate STS HRM.....	41
Table 3-2: Shear Test Parameters.....	53
Table 3-3: Shear Test Results.....	55
Table 3-4 Column test mixture components.....	57
Table 4-1: The dimensions and resistance of the designed heater.....	66
Table 4-2: The dimensions of the three heater designs and the theoretically calculated the platinum resistance.....	72
Table 4-3: Peak focusing calculated for Temperature gradient GC (TGGC) and Temperature programmed gradient GC(TPGGC).....	83
Table 5-1: Base resistance of the TCD at different pressure levels.....	94
Table 5-2: List of compounds in the mixture .....	98
Table 6-1: Purge and trap setup conditions .....	103
Table 6-2: Mixture compounds .....	107

## LIST OF FIGURES

Figure 1-1: ELISA method for detection of pathogen .....	2
Figure 1-2: (a) PCR method [3] (b) DNA microassay. ....	3
Figure 1-3: Principle of elution chromatography .....	7
Figure 1-4: Static coating setup.....	9
Figure 1-5: Convectional GC oven.....	11
Figure 1-6: IR heating methods using a lamp.....	12
Figure 1-7: Resistive heating principle.....	13
Figure 1-8 (A) Micro-devices, (B) SEM images showing micro-posts in $\mu$ PC, (C and D) polydimethylsiloxane coating on the interior wall of the column channel.[14] .....	17
Figure 1-9: Photo of hybrid device together with a cell phone.[31] .....	18
Figure 1-10: Photograph of the prototypal miniGC system: single components (a), assembled miniGC (b), complete packaged prototype (c) and close-up on the pneumatic interconnections (d) [32].....	19
Figure 1-11: Block diagram of the MEMS $\mu$ GC prototype analytical system: (a) calibration-vapor source before (left) and after (right) assembly; diffusion channel and headspace aperture can be seen in the top section and macro- Porous Silicon(PS) reservoir can be seen in the bottom section; (b) 3-stage adsorbent $\mu$ PCF prior to loading and sealing (top left), with close-up SEM images of each section loaded with adsorbents (lower left) and assembled structure with capillary interconnects on a U. S. penny; (c) 3 m separation-column chip (left) with close up views of the channel cross-sections prior to (top right) and after (lower right) sealing; (d) detector assembly with 4-chemiresistor array chip (right), Macor lid (white square structure), and sealed detector with connecting capillaries mounted on a custom mounting fixture (left). The dashed line is a flow-splitter [13] .....	20
Figure 2-1: Chromatogram of a two component mixture .....	25
Figure 2-2: (a) Parallel plate system, (b) circular column and (c) rectangular column .....	29
Figure 2-3: Effect of column with for a 3 meter column.....	31
Figure 2-4: Plot of the optimum velocity and plate height for the 50 $\mu$ m channel column. ....	32

Figure 2-5: Plot of height equivalent to the theoretical plate versus average carrier gas (Helium) velocity for a different length of the column. ....	33
Figure 2-6: (a) Schematic of 2 and 3 meters GC column and the final column (b) mask layout of the column (c) final column (d) etch profile of the column .....	35
Figure 2-7: Effect of column width and length for 2 and 3 meters column with 50 and 75 diameter width (Height is 300 $\mu$ m, k=5, P=8.5 psi) .....	36
Figure 3-1: MEMS Column MASK Design layout.....	40
Figure 3-2: STS HRM etch quality for different power and etch rates .....	42
Figure 3-3: Temperature and pressure programming of SB6 wafer bonder .....	44
Figure 3-4: Process flow for fabrication of micro-GC column: A) 500 $\mu$ m (100) silicon wafer; B) Resist spin coating; C) Channel lithography; D) STS HRM Deep RIE; E) Resist stripping; F) Back side resist spin-coating; G) Alignment and lithography; H) Deep IRE of input hole; I) Resist stripping; and J) 200 nm gold deposition on a wafer and wafer bonding.....	45
Figure 3-5: LEXT imaging A) Top View, B) 3-D view C) profile measurement .....	46
Figure 3-6: (a) Schematic of 2 and 3 meters GC column, (B) 3 meters MEMS GC column, and (C) etch profile of the column. ....	47
Figure 3-7: NanoPort Adaptor attachment setup .....	48
Figure 3-8: Stationary coating setup.....	49
Figure 3-9: SEM images of cross-section of the gold fusion bonded column. ....	50
Figure 3-10: a) SEM images of the bonded interface of gold eutectic bonded; b) Energy dispersive X-ray showing the Au richness around the bonded area; and c) Location of gold atoms at the interface, d) Location of silicon atoms, e) location of oxygen.....	52
Figure 3-11: Die Shear Test setup .....	53
Figure 3-12: Shear test results of seven samples .....	54
Figure 3-13: Chromatographs showing retention time of 1 $\mu$ l of butane with split ratio of 150:1 .....	56
Figure 3-14 : Chromatograph achieved using the 3-meter HP-1 column at pressure 10 psi and inlet temperature of 240 $^{\circ}$ C .....	57

Figure 3-15: Chromatograph achieved using a 3 meter MEMS GC at pressure 16 psi and inlet temperature of 240 °C and isothermal at 80 °C for the first 2 min and ramp 10 °C/min to 120 °C .....	58
Figure 4-1: MEMS GC thermal programming A) Isothermal B) Temperature-programmed C) 2-D Axial heating .....	63
Figure 4-2: A) Side view of GC Column with heat losses B) layout the heater .....	67
Figure 4-3: A) 200 nm oxide grown thermally B) the top-side is coated with photoresists C) 115 nm of Ti/Pt deposited using E-beam evaporator D) wire bonded the heaters to the package .....	69
Figure 4-4: Experimental setup .....	70
Figure 4-5: Temperature distribution with 6 W of electrical power dissipated in the heating element on the GC silicon column and surrounding air at ambient temperature of 20°C and b) sensors location c) temperature profile .....	71
Figure 4-6: Mask designs of the radial heater and the temperature sensor: (a) Design a (b) Design b (c) Design c .....	72
Figure 4-7: Simulated transient response of temperature over time after applying 6W of electrical dissipation to the heater, for the three designs.....	73
Figure 4-8: Experimental setup for TCR measurement.....	74
Figure 4-9: Temperature calibration data for the heater, where each data point was obtained by subjecting the column to a uniformly heated glass plate surface.....	75
Figure 4-10: Forced convection heat transfer coefficient for 4000 rpm and a fan to plate distance of 15 mm[47].....	76
Figure 4-11: Plot of simulated average temperature transient response of the resistor film with 2W electrical power applied to the heater compared to experimentally measured temperature on the micro-GC column with convection heat transfer coefficient in air as a parameter. ....	77
Figure 4-12: 2-D Experimental Setup A) Top View B) Side view with the location of the fan from the chip .....	78
Figure 4-13: Transient response of heater design b to a 0.5 A constant current.....	79
Figure 4-14: Transient response of the heater at two different power levels.....	80

Figure 4-15: Temperature distribution in Kelvin, estimated from IR thermal imaging with an applied voltage of 13 volts applied to heater b with forced convection present.....	81
Figure 4-16: Chromatograph achieved using the 3 meter column at pressure 16 psi and inlet temperature of 240 °C with OV-1 stationary phase using A) 60°C isothermal temperature B) temperature gradient with center temperature of 60 °C C) Temperature gradient programmed at 250 °C/min from 60°C to 110 °C...	82
Figure 4-17: Separation of a hydrocarbon mixture A) Temperature gradient programmed ramped at 150° C/min B) Temperature gradient programmed ramped at 250°C/min.....	85
Figure 5-1: Summary of ultra-low power TCD fabrication process [43] .....	89
Figure 5-2: Scanning electron microscope image of the fabricated micro sensor; a 100:1 bridge with 50:1 μm narrow center region .....	90
Figure 5-3: sensor packaging with flow ports and electrical connections .....	91
Figure 5-4: Schematic of the experimental setup for μTCD testing in GC system .....	93
Figure 5-5 A) Circuit interface B) experimental setup .....	93
Figure 5-6: TCD response for different pressure levels. ....	95
Figure 5-7: Response of the MEMS TCD for different sample concentrations .....	96
Figure 5-8: the concentration hexane vs. the area under the curve.....	97
Figure 5-9: FID responses, B) TCD responses.....	98
Figure 6-1: Infected tree with <i>Armillaria</i> .....	100
Figure 6-2: SPME adsorbent station.....	104
Figure 6-3: A) Inoculated <i>Armillaria</i> sample C) agar sample .....	104
Figure 6-4: Raw data collected for 4 days of sample and control .....	105
Figure 6-5: Chromatograms comparison for the inoculated <i>Armillaria</i> culture and the Agar nutrient media. ....	106
Figure 6-6: (A) Schematic diagram showing the key components of the proposed MEMS-GC system and the innovation. (B) Photograph of MEMS-GC system components. ....	108
Figure 6-7: Chromatograph achieved using the 3-meter column at 8.06 psi and inlet temperature of 240 °C and temperature at 80 °C and ramp rate 10 C/min .....	109
Figure 7-1: Nanotube structure.....	113

Figure 7-2: Chemiresistor sensors with 4  $\mu\text{m}$  spacing .....114  
Figure 7-3: convention coefficient as a function of radius .....115

## SUMMARY

The focus of this dissertation is on the design and micro-fabrication of an all silicon gas chromatography column with a novel two dimensional resistive heater and on its integration with an ultra-low power Thermal Conductivity Detector (TCD) for fast separation and detection of Volatile Organic Compounds (VOC). The major limitations of the current MEMS-GC column are: direct bonding of silicon to silicon, and peak band broadening due to slow temperature programming. As part of this thesis, a new gold eutectic-fusion bonding technique is developed to improve the sealing of the column. Separation of BETX, alkane mixture and VOCs were demonstrated with the MEMS GC column. The time and power required to ramp and sustain the column's temperature are very high for the current GC columns. To reduce the time required to separate the compounds, a new temperature gradient programming heating method was developed to generate temperature gradients along the length of the column. This novel heating method refocuses eluding bands and counteracts some of the chromatographic band spreading due to diffusion resulting in an improved separation performance. A low power TCD was packaged and tested in a GC by comparison against FID for the detection of a mixture of VOCs. It demonstrated low power operation of a few milliwatts and a very fast response. The MEMS-GC was also demonstrated for rapid detection of the VOC gases released by pathogenic species of *Armillaria* fungus.

## Chapter 1

### INTRODUCTION AND BACKGROUND

#### 1.1 Methods of pathogen and fungal detections

Infectious diseases induced by fungus and bacteria are the number one driving cost for farmers. Early detection of these fungi and bacteria is critical to control the rapid spread of the agents. There are currently several techniques used for detection of these infections; these include molecular techniques, spectroscopic and imaging techniques, profiling of plant VOC gases and Visual Tree Assessment (VTA).

Currently potentially infected trees are detected primarily using the Visual Tree Assessment (VTA), as farmers inspect trees visually for signs and symptoms associated with the disease.[1] However, this method can only be used to identify the infection at a late stage. Besides, it cannot identify the rotting fungi involved. Due to the inefficiencies of the VTA model and its effect on crop production, an accurate and early identification of fungal infection in orchards is critical to control the rapid spread of the fungal agents.

Currently, there are several molecular techniques adopted for early separation and detection of pathogens such as: impedimetric biosensors[2], microfluidic chemotaxis[3] ELISA[4], PCR, and DNA microassay. ELISA and PCR are the most commonly used detection methods. ELISA methods are based on the use of antibodies for detecting the source of infection by pathogenic species of *Armillaria*. Figure 1-1 summarizes the ELISA method of detection.

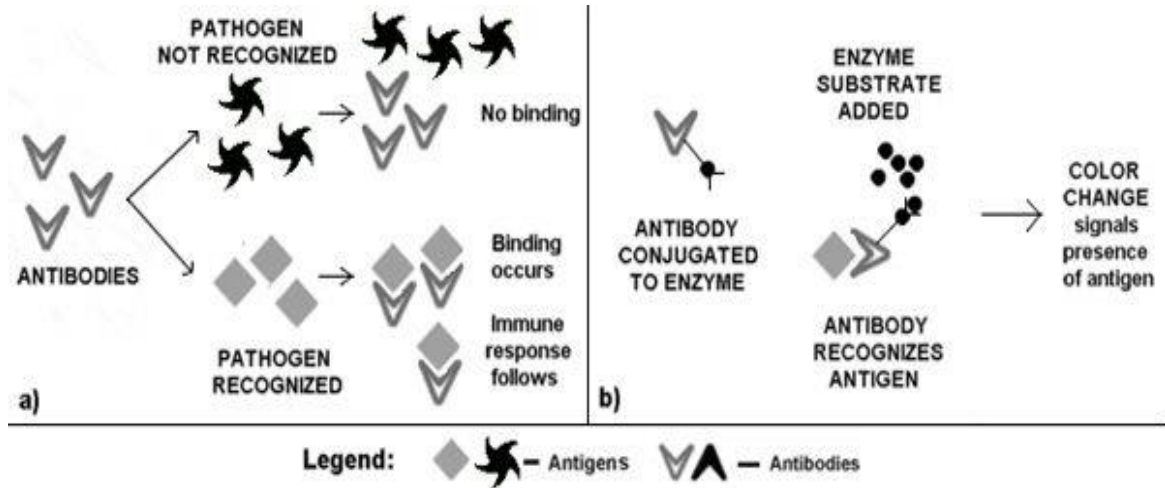


Figure 1-1: ELISA method for detection of pathogen

In this model, the wells are coated with specific antibodies, and in case the antibodies' specific antigens are present, they bind to the antibodies in the bottom of the wells. For this case only antigen specific antibodies bind to the wells. Next, the wells are washed out to remove the excessive antibodies. A solution of animal antibody against human antibody is added, and the second antibody is covalently conjugated to an enzyme. The wells are washed again to remove the enzyme conjugated antibody. Finally, a solution of the cryogenic enzyme substrate is added to generate visible color, which is evidence of substrate interaction with the enzyme on the second antibody.

The advantages of using this technique are that it is visible to the human eye, inexpensive, and easy to use. In addition, there are several ELISA test kits available for detection of root crops (e.g. cassava, beet, potato), ornamentals (e.g. lilies, orchids), fruits (e.g. banana, apple, grapes), grains (e.g. wheat, rice), and vegetables. ELISA techniques also can detect rotten stunting disease of sugarcane, tomato mosaic virus, papaya ringspot virus, banana bract mosaic virus, banana bunchy top virus, watermelon mosaic virus, and rice tungro

virus. However, the main difficulties facing these techniques are: to isolate specific antigens and to develop specific, either polyclonal or monoclonal antibodies to the antigens, so the development of the immunological technologies for detection of fungal pathogens has been poor.

Nucleic acid-based methods rely on DNA markers for pathogen species identification. [5] The methods are sensitive and specific. In this technique, multiple copies of a DNA segment of interest are generated; these segments are amplified to make pathogen and viruses detectable. However, these segments are prone to contamination, require lengthy sample preparations, skilled labor and expensive equipment. DNA microarrays are also used for simultaneous pathogen detection. After a DNA sample is replicated using PCR and is labeled with fluorescent dyes, it is hybridized in an array. This technique is very effective, but very expensive and requires expensive equipment.

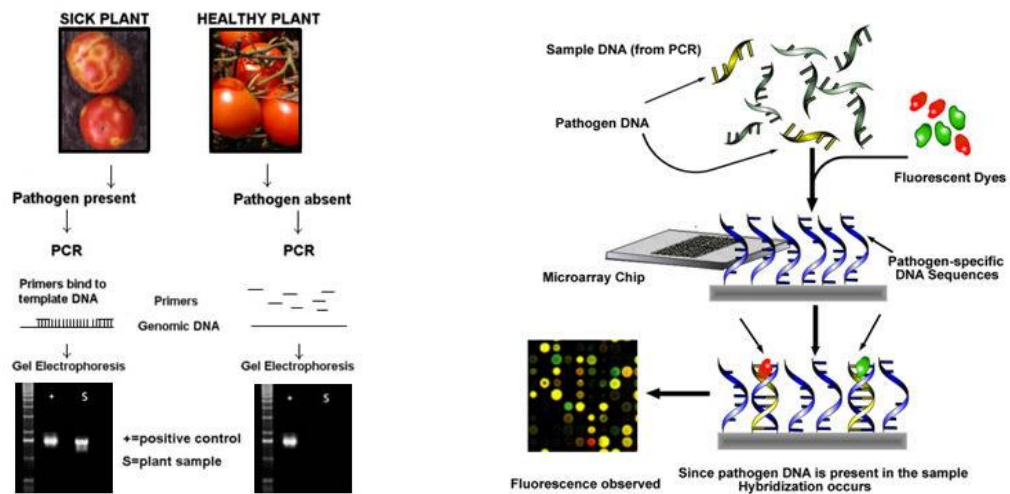


Figure 1-2: (a) PCR method [6] (b) DNA microarray.

Bioluminescence-based techniques exploited the light emitted from *Armillaria spp.* due to the presence of a NAD-dependent luciferin-luciferase system [7]. They are straightforward and can be field usable. Bioluminescence analysis is one of the low-cost and rapid methods for environmental monitoring and detection of toxic compounds. However, the luminescence emitted from *Armillaria* can be affected by environmental conditions [8, 9]. In addition, many non-*Armillaria* fungi and bacteria also emit bioluminescence around 520 nm, which could interfere with the *Armillaria* detection.

HPLC and GC/MS based fungi detection methods measure the composition of metabolites released from individual fungi, which are controlled largely by the genetic types and combinations of the metabolic pathways. In particular this includes volatile organic compounds (VOC) released by the decayed trees. Included in these metabolites are the fungus-induced tree antimicrobial defense compounds which could be used to develop a rapid and field usable fungal infection screening method.

The GC/MS based method currently is the gold standard for VOC analysis [10]. It contains a gas chromatography-based separation and mass spectroscopy-based compound identification. The method is very sensitive, with a detection limit of sub-ppb. However, it requires an expensive instrument and a relative long separation time if traditional separation columns are used (>20mins). Many low-cost and field usable VOC sensors have been developed to provide rapid results [11] including piezoelectric, colorimetric, fluorescence, and chemiresistors, etc. Although these systems have proved to be very powerful measurement tools, very few groups have measured real-life samples directly, mainly due to the following issues;

(a) Low detection sensitivities — for many sensor systems detection limits are in the low ppm range, whereas in environmental samples the analyses of interest are present at concentrations up to three orders of magnitude lower than this [12].

(b) They can't be used to analyze gas mixture reliably regardless of the transducer and coating materials. Pattern recognition on sensor arrays can be used to analyze the gas mixture; however, the number of VOCs in the mixture is very limited. The VOCs collected from the decayed samples could contain up to 120 compounds [13]; therefore, a simple VOC analyzer will not be able to provide detailed information for fungal species identification.

The goal of this research is to deliver an ultra-low power Micro-Gas Chromatography system utilizing MEMS technology to live-screen the VOC gases released by trees and plants, as well as their water stress level. The system consists of an all silicon MEMS GC column with integrated isothermal and two-dimensional heaters for fast temperature-programming of the column and ultra-low power  $\mu$ TCD.

## 1.2 Gas Chromatography

Gas chromatography is one the most common analytical methods for separation and detection of volatile and semi volatile organic compounds due to its sensitivity, separation efficiency, and simplicity. There has been considerable interest in miniaturizing the gas chromatography column system into a low power, portable system since its introduction by Terry [14] and subsequent efforts by Reston and Kolesar in 1990 [15]. Sandia National Lab was the first to integrate a MEMS GC column with chemical sensor arrays and a

preconcentrator into a hybrid system for fast detection of specific explosive markers, and for determining trace organic compounds in environmental samples. Chia- Juang Lu [16] developed a first-generation hybrid MEMS gas chromatograph system that uses air as the carrier gas and a silicon etched column sealed with glass anodic as the bonding. Also, Garg and et al. [17] has recently developed a compact mini-GC system for detection of hazardous pollutants in environmental air samples. However, the system is selective, and the heating system is not ideal. Despite significant progress by Enose [18, 19] to integrate all the components of micro-GC system into a small system, currently there is no fully integrated portable, low power, and low cost GC system capable of separating and detecting multiple VOCs in a short time.

### **1.2.1 Elution Gas Chromatography**

The most common technique for separating gases is the elution technique, where a stream of inert gases passes through the column and interacts with a stationary phase of choice. In theory, after injecting a mixture of compounds into the mobile phase, the mixture passes through the column while interacting with the stationary phase. Some compounds are more retained by the stationary phase; as a result, the compounds are separated based on their retention time. Figure 1-3 demonstrates this principle.

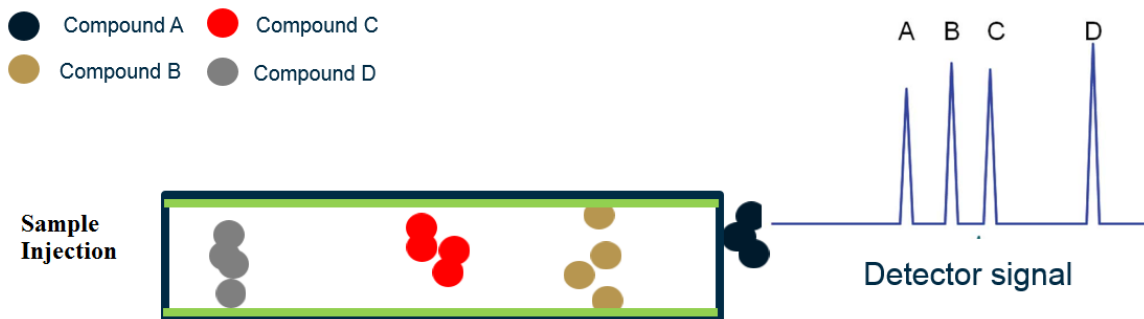


Figure 1-3: Principle of elution chromatography

### 1.2.2 Injection Port.

Fast and repeatable injections of samples into the GC system directly affect the column efficiency; therefore, an injector with a small dead volume and very fast valve is necessary to prevent band spreading and poor resolution. Standard GC columns require much smaller samples; therefore, a split ratio system has been employed to inject a small amount of sample into the system. The split ratio system injects just a fraction of the mixture into the system and the rest goes to waste. There has been a substantial amount of work undertaken historically in miniaturizing the injector port to a power-efficient and narrow injection time-width pulse [20].

### 1.2.3 Column

The GC column is the heart of the gas chromatography system, where most of the separation takes place. Conventional bench-top GC systems use 15-60 meter-long fused silica capillary columns coated with a very thin stationary phase for separating different compounds. To fill the need for a small and low power system, a standard GC column is miniaturized to a smaller size and shorter length column. These advancements facilitate

integration of the column into a single lab on a chip device that can provide rapid analysis of VOC gases.

Most of the previously microfabricated GC columns are fabricated on Si substrates [15, 21-29]. Initially, the columns were etched in silicon using a wet etch technique isotropically [14]. However, in the recent years, with advancement in MEMS fabrication, most microfabricated columns are fabricated using RIE etch processes (anisotropic etch). Isotropic etching provides smoother walls with shallower channels; in contrast, deep RIE etch increases surface roughness. The uniformity of the stationary phase coating consequently suffers significantly as a result of surface roughness. This is one of the main reasons that the efficiency of a MEMS GC is lower than that of a standard column.

#### 1.2.3.1 Stationary Phase

The stationary phase is the key component of a GC column; it is a coating inside the column that reacts with the gases and affects the rate of the diffusion in and out of the mobile phase. Commercial columns are sold with different thicknesses and coatings. Static and dynamic coatings are the two most common methods used for coating an open-tubular fused-silica column. In the static coating method, the column is first filled with a fixed concentration of stationary phase dissolved in a suitable solvent, and a vacuum is applied to the other end. The thickness of the stationary phase deposited using this method is a function of the solution concentration, surface area of the column, and the density of the stationary phase.



Figure 1-4: Static coating setup

In dynamic coating, the column is first filled with the stationary phase and the excessive solution is pushed out of the column using nonreactive gas such as nitrogen. The film thickness deposited using this method is a function of the air velocity and the concentration of the stationary phase.

$$d = \frac{r \times c}{200} \left( \frac{U\eta}{\gamma} \right)^{\frac{1}{2}} \quad \text{Equation 1-1}$$

where  $d$  is the coating thickness,  $r$  is the radius,  $c$  is the concentration,  $u$  is the average velocity,  $\eta$  is viscosity, and gamma is surface tension. Quartz crystal microbalance (QCM) method was used previously to investigate the absorption and the diffusion of organic chemicals in the materials. The distribution constants of representative volatile organic chemicals were also able to be calculated [30-32].

Stationary phase resistance time in the column is caused by the polarities of the solute and the stationary phase. The two main stationary phases are polar and nonpolar.

Nonpolar stationary phases such as dimethyl polysiloxane (PDMS), hydrocarbon, dialkyl

siloxanes, whereas, polyester phases are highly polar. A rule of thumb is that the sample polarity should always match the stationary phase polarity.

Table 1-1: Different stationary coatings and their application

<b>Stationary phase</b>	<b>Trade name</b>	<b>Application</b>
Dimethylsilicone Gum	Silicone OV®-1	Hydrocarbon,
Phenyl(10%) methylsilicone	Silicone OV®-3	Fatty acid methyl esters
Phenyl (20%) methylsilicone	Silicone OV®-7	Steroids, pesticides

Over time, non-cross-linked GC columns slowly lose their stationary phase coating because of the interaction between the coating and the solute. In commercial GC columns, the stationary phase is cross-linked to the column and treated to provide a long lasting coating. The smoothness and thickness of the column directly affects the resolution of the separation; therefore, coating a MEMS GC column is a critical step in successfully micro-fabricating a column.

### 1.2.3.2 Column Heating Techniques

Temperature is the prominent factor that affects the separation performance of the column and that could be easily controlled. Due to its importance, there have been many efforts to control the temperature of a standard GC column by implementing different heat transfer phenomenon such as conduction, convection and radiation.

### 1.2.3.2.1 Convective Air Oven

The most common approach for heating and cooling a gas chromatograph's column is by placing it inside an oven and carrying the heat by forced convection. In this method, the temperature inside the oven stays relatively uniform, and the temperature could be adjusted rapidly.

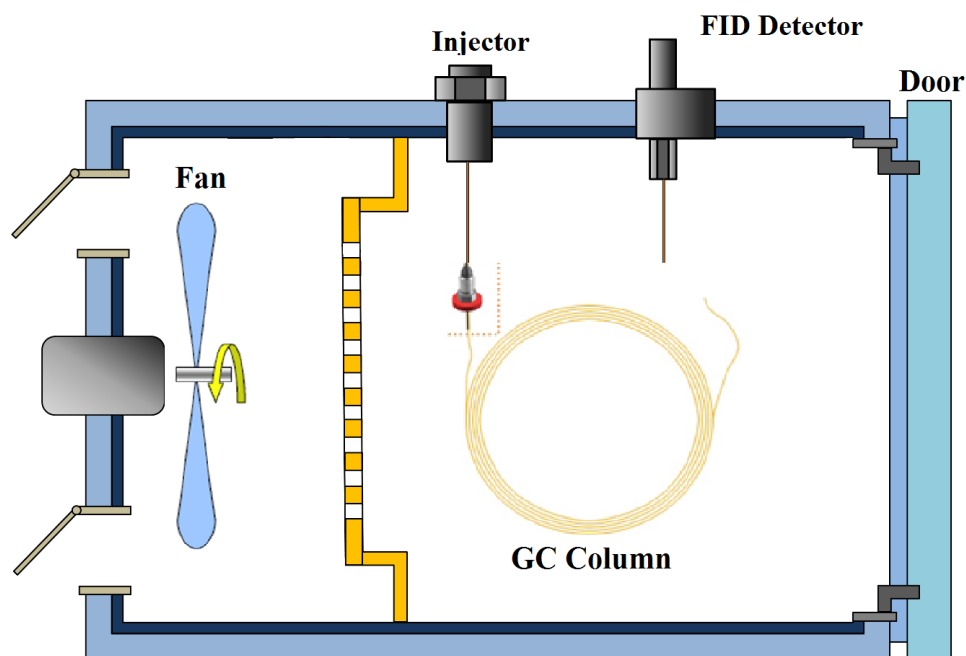


Figure 1-5: Convective GC oven

Heating the column using an oven is ideal for a commercial column since the columns are thin and could be heated quickly. However, ovens have a large internal volume and thermal mass; as a result, a large amount of energy and time are required to reach a temperature that is not practical for a portable application.

### 1.2.3.2.2 Infrared Heating

In infrared heating methods, electromagnetic waves are used to transfer the heat energy into the cold column. The amount of energy radiated by a heating filament is determined by the filament's temperature, and the filament temperature is controlled using the current applied. The disadvantage of using this method is that maintaining the rates of radiation and surface adsorption is difficult.

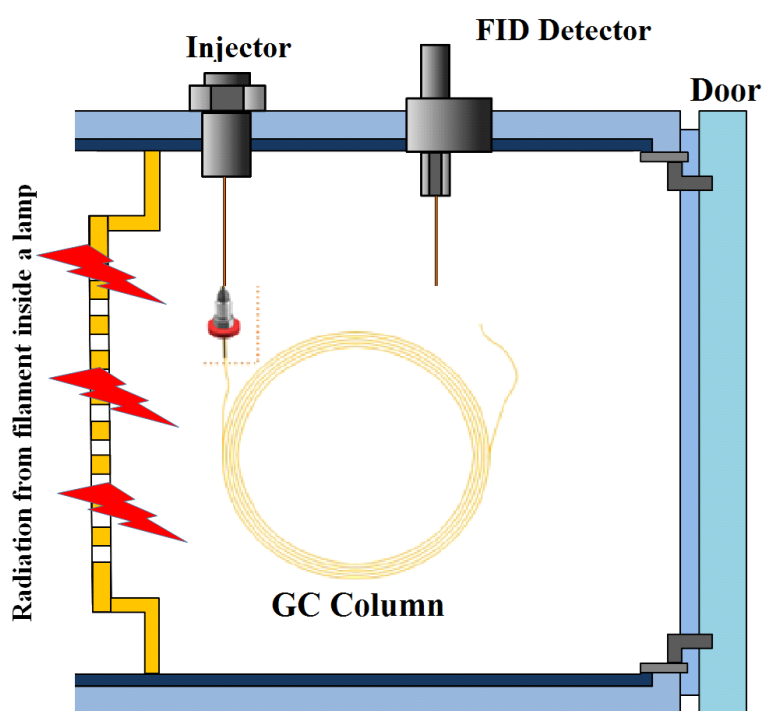


Figure 1-6: IR heating methods using a lamp

### 1.2.3.2.3 Resistive Heating

In resistive heating, the columns are coated with a conductive material, and the column is heated by applying an electrical current to the conductive layer. Resistive heating is

driven by joule heating, in which heat is generated by flow of electrical current through the layer and is driven by

$$P = I^2 R = j^2 \rho V \quad \text{Equation 1-2}$$

where  $P$  is the joule heating power,  $I$  is the current,  $R$  is the resistance,  $\rho$  is the resistivity, and  $V$  is the volume.

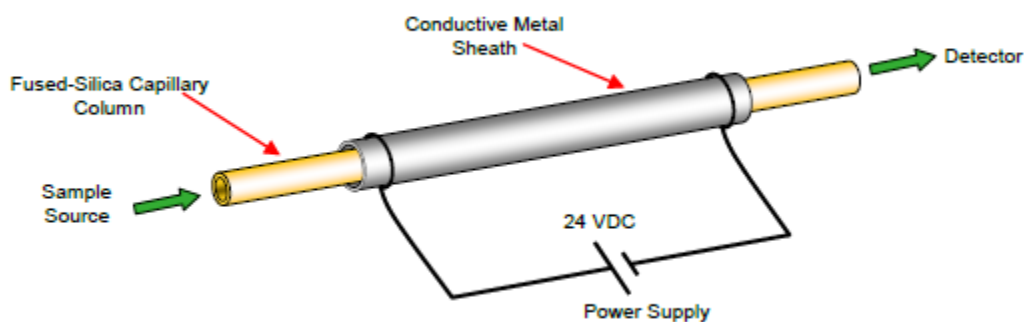


Figure 1-7: Resistive heating principle

The advantages of using this method are the lower power consumption and faster heating and cooling times, which are ideal for portable GC applications.

Two methods are commonly used for heating a MEMS GC column using the resistive heating technique: isothermal and temperature programmed. In the isothermal mode the column temperature remains constant while separation takes place. In the temperature programming mode, resistive heating is used to control the column's temperature. Low power and low mass are very important in the GC development.

Temperature uniformity is critical for temperature programming mainly because formation of hot and cold spots could cause band broadening. Agah [33] has investigated the effect of temperature programming and compared it with the isothermal model.

#### **1.2.4 Detector**

Detectors are an important part of the GC system. The ideal detector is a very fast, nondestructive, sensitive, and low power sensor that is independent of the flow rate and has a linear response to solutes' concentration. Many detectors are used for GC application, but the most popular are 1) Flame Ion Detector (FID) 2) Thermal Conductivity Detector (TCD) and 3) Electron Capture Detectors. Others are plasma photoionization, microresonator i.e. quartz tuning fork, SAW surface acoustic wave sensor [31, 32], and electrochemical sensors. These are apart from the standard FTIR and MS instruments mentioned in review paper on detection methods for VOC's from plants where they also discuss the photoionization detectors for isoprene, which have sub-second response time).

##### **1.2.4.1 Flame Ion Detector (FID)**

FID is the most widely used detector for conventional GC systems due to its sensitivity and reliability. FID uses a mixture of a combustible gas and air to form a flame above the burner and measure the current generated across the electrodes and nozzle due to ionized combustion products. The nozzle is typically polarized at several hundreds of volts. FIDs are sensitive to hydrocarbon, VOCs and halogen; however, the detector is not sensitive to incombustible gasses such H<sub>2</sub>O, CO<sub>2</sub>, SO<sub>2</sub>, and NO<sub>x</sub>. Zimmerman et al. [34] proposed a MEMS FID and flame spectrometers with 100 ppb level of detection for

pentane, which uses a combustible gas to generate flame. Kuipers et al. designed a planar MEMS FID with an integrated electrode, and with a detection limit of 450 pg carbon per second for methane [35]. A MEMS FID detector with a diffusion flame was developed for use in a portable system [36] with sensitivity of 0.02 C/mol for methane. However, the a FID detector for portable applications is rarely available, mainly due to the safety precautions involved with combustible gases and high fuel consumption.

#### 1.2.4.2 Thermal Conductivity Detector (TCD)

Thermal conductivity detectors are based on the change in thermal conductivity of the compounds passing over the detector. The detector is heated electrically with a fixed power input, so that its temperature depends on the thermal conductivity of the surrounding gases. TCDs are commonly used in helium, since the thermal conductivity of the helium is ten times higher than that of organic compounds. Therefore, in the presence of these compounds, the TCD temperature rises in response to the change in thermal conductivity of the organic compounds. The main advantages of using a TCD in a GC system are its low cost, nondestructive operation, fast response, and simplicity. On the other hand, the main limitation of these detectors is their low sensitivity.

#### 1.2.4.3 Electron Capture Detector

The electron capture detector is another widely used detector for halogen-containing compounds that are hard to detect, such as pesticides and polychlorinated biphenyls. There are other commercially available detectors such as chemiresistors; those have been used as a micro GC detectors for identification and quantification of VOC gases.

### **1.2.5 Overview of Miniature Gas Chromatography**

The table below summarizes the current state of the art of the micro GC system. Garg et al. [17] have demonstrated implementation of a microfabricated gas chromatography system specialized for detecting hazardous air pollutants (HAPs) at part-per-billion (ppb) concentration level. A MEMS separation column with an on-chip thermal conductivity sensor, and a micro preconcentrator were integrated for separating and detecting benzene, toluene, tetrachloroethylene, chlorobenzene, ethylbenzene, and p-xylene. They have reported a limit of detection (LOD) of ~1 ng with sampling time of 10 min at a flow rate of 1 mL/min, and they showed 3 orders of magnitude lower sample volume as compared to the conventional GC system.

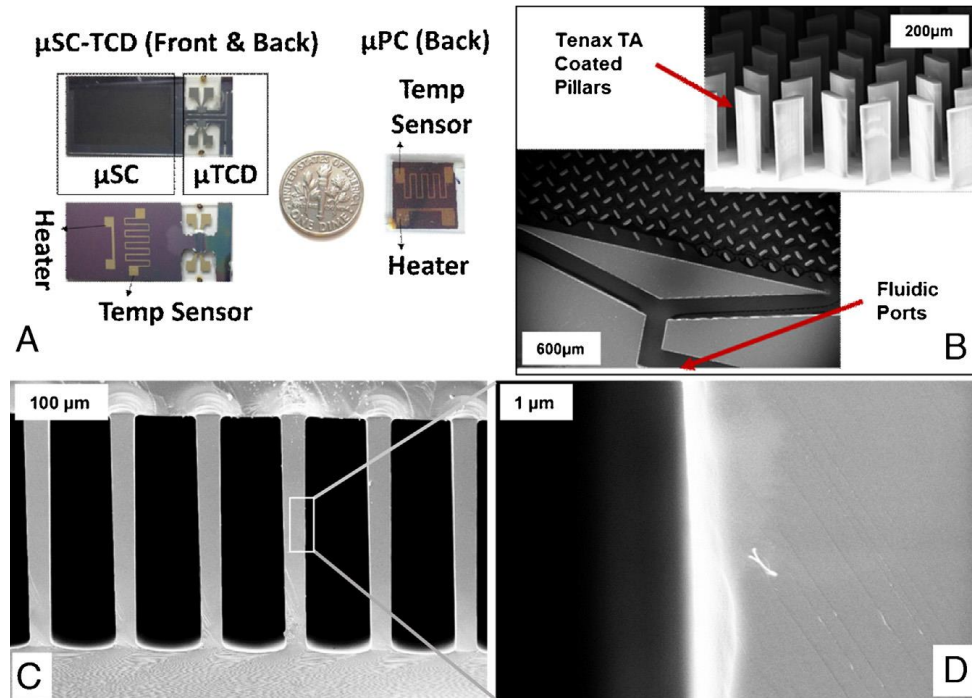


Figure 1-8 (A) Micro-devices, (B) SEM images showing micro-posts in  $\mu$ PC, (C and D) polydimethylsiloxane coating on the interior wall of the column channel.[17]

Cheng Chen and et al. [37] have developed a hybrid sensor system for monitoring VOCs in the air by integrating a GC column with a quartz tuning fork detector. The system was used to separate benzene, toluene, ethylbenzene, and xylenes (BTEX) in the presence of complex interfaces with a detection limit of  $\sim 1$  ppb)

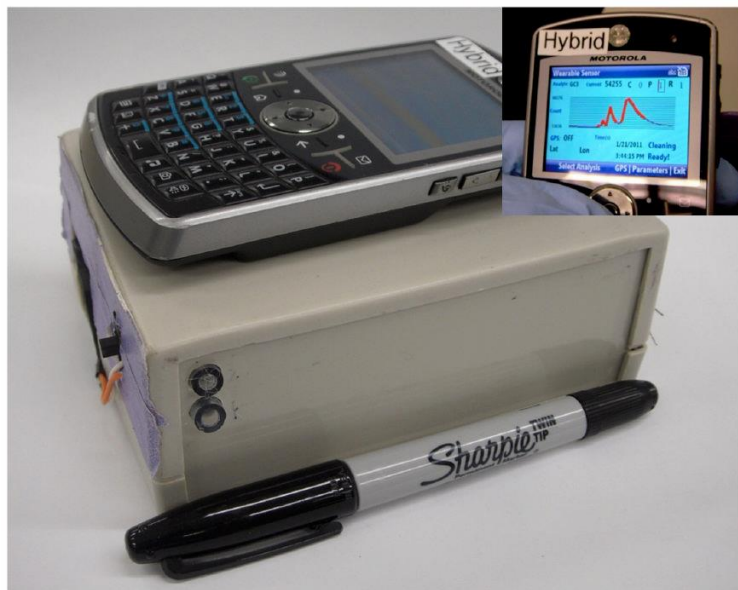


Figure 1-9: Photo of hybrid device together with a cell phone.[37]

Zampolli and et al. [38] have micromachined a GC system with highly sensitive MOX detectors for detection of aromatic VOCs with detection limit of sub ppb. A 0.5 m long spiral channel was etched into a silicon wafer and encapsulated with a Pyrex wafer. A very sensitive MOX array sensor, which is highly sensitive to aromatic volatiles, was developed to detect VOC, NO<sub>2</sub> or O<sub>3</sub> while using air as the carrier gas.

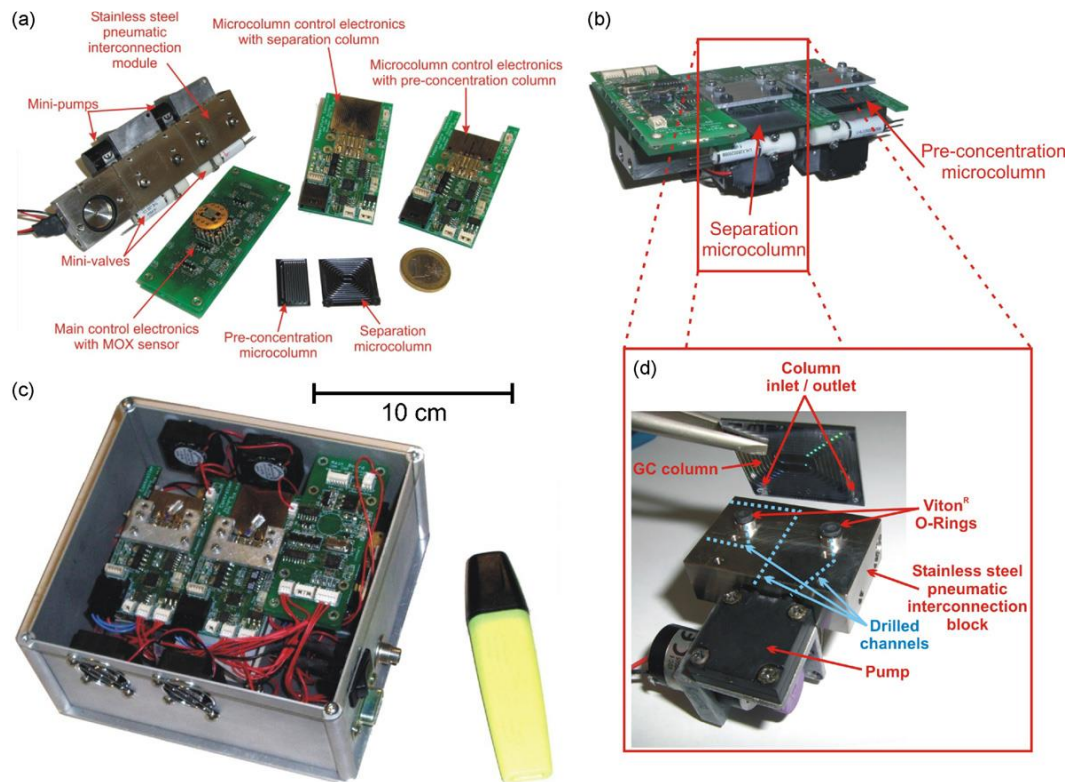


Figure 1-10: Photograph of the prototypical miniGC system: single components (a), assembled miniGC (b), complete packaged prototype (c) and close-up on the pneumatic interconnections (d) [38]

Lu et al. [16] developed the first hybrid microfabricated gas chromatograph system with all analytical components integrated into a complete system; it is shown in the figure below. The system is comprised of a preconcentrator, a separation column, and multi chemoreceptors. The separation column was etched in silicon and sealed using anodic bonding. The hybrid system could separate eleven vapor compounds in a few minutes with sub ppb level of detections.

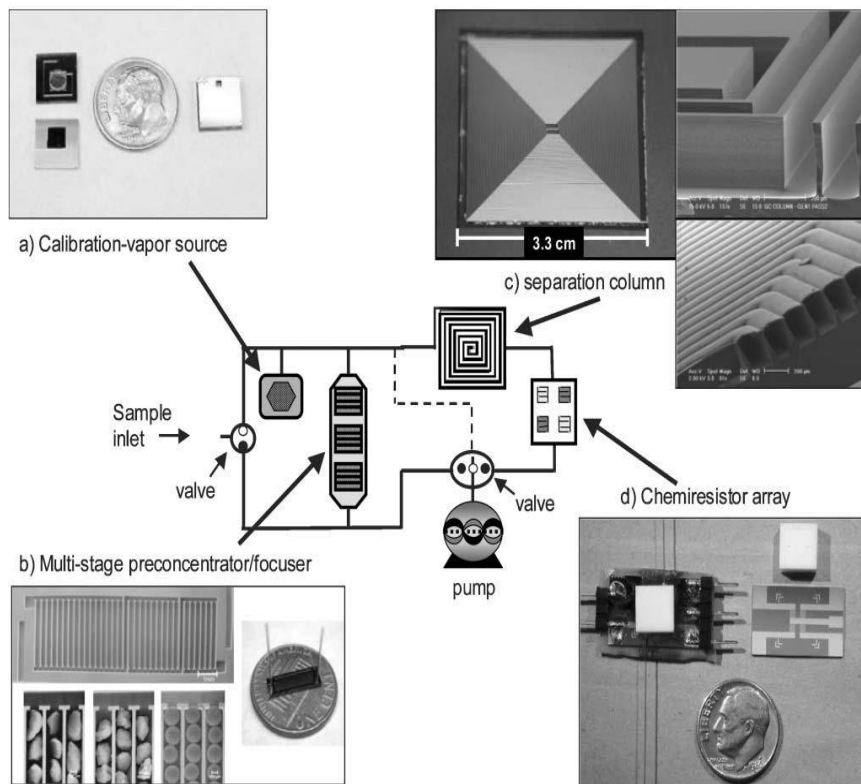


Figure 1-11: Block diagram of the MEMS  $\mu$ GC prototype analytical system: (a) calibration-vapor source before (left) and after (right) assembly; diffusion channel and headspace aperture can be seen in the top section and macro- Porous Silicon(PS) reservoir can be seen in the bottom section; (b) 3-stage adsorbent  $\mu$ PCF prior to loading and sealing (top left), with close-up SEM images of each section loaded with adsorbents (lower left) and assembled structure with capillary interconnects on a U. S. penny; (c) 3 m separation-column chip (left) with close up views of the channel cross-sections prior to (top right) and after (lower right) sealing; (d) detector assembly with 4-chemiresistor array chip (right), Macor lid (white square structure), and sealed detector with connecting capillaries mounted on a custom mounting fixture (left). The dashed line is a flow-splitter [16]

Table 1-2	Detection	Separation	
MicroGC			
Ambient-Air	Chemi-resistor array 0.48-2.2 ng	1-m, spiral channel (150 $\mu\text{m} \times 240 \mu\text{m}$ ) PDMS coated micro-column, temperature controlled	INTREPID system, University of Michigan, Ann Arbor[39]
Ambient-Air	Tuning fork( $\sim 100\text{ppb}$ )	Multiple configurations. 2-m & 19-m carbowax coated capillary columns Separation time: 3 min	GC system, Arizona State University[37]
Ambient-Air	Metal Oxide Semiconductor 5 ppbv	0.5-m, spiral channel (800 $\mu\text{m}$ deep) carbograph packed micro-column, temperature controlled Separation time: 10 min	GC system, CNR-IMM Institute for Microelectronics and Microsystems[38]
Helium	Micro TCD  $\sim 1 \text{ ng}$	2-m, rectangular channel (70 $\mu\text{m} \times 240 \mu\text{m}$ ) PDMS coated micro-column, temperature controlled Separation time: 1 min	Zebra GC system, Virginia Tech [17]
Helium	Micro TCD	2 m column with axial temperature control	GTRI System
	SAW(1-10 ppb)	0.8 m column with (40 $\mu\text{m} \times 250 \mu\text{m}$ )	ChemLab

### **1.3 Proposed Solution: Development of a novel bonding method using eutectic- fusion bonding for micro-fabrication of all silicon GC column**

In this chapter, we present a new method for improving the bonding quality of silicon-silicon by combining eutectic and fusion bonding. The conventional bonding techniques such as anodic bonding are not suitable for fabrication of a micro gas chromatograph column mainly due to the difference in thermal conductivity and thermal expansion of the bonded pieces. The new method consists of the fabrication of a 500  $\mu\text{m}$  thick GC column and its bonding with a 200  $\mu\text{m}$  silicon cap. The bonding technique was first validated for micro-fabrication of an all silicon 3-meter gas chromatography column that could withstand the temperature cycling required for axial temperature programming. The process parameters, especially the bonding quality, are thoroughly examined and the bonding layer was further investigated using SEM, EDX, and mechanical shear test.

### **1.4 Proposed Solution: integrating a novel Axial heating**

Column temperature is an important parameter that could easily control and affect the separation performance of the column. Here we investigate the effects of temperature gradients as a function of time and position,  $T(t,x)$ , along the length of the column. The heater design first was evaluated using COMSOL multiphysics. Heat transfer and resistive heating modeling were performed to investigate the heating and cooling rate, power consumption, and temperature distribution of the new Axial heating method for the all silicon

GC column. The actual thermal cycling was also measured for the GC column with an embedded heating element. Different heater designs were investigated and the design with the maximum temperature distribution was selected for microfabrication.

### **1.5 Proposed Solution: integrating an Ultra-low power TCD sensor**

An ultra-low power TCD was developed and tested at different flow rates. The effect of different flow rates and the limitations of the TCD were further investigated by integrating the TCD in line with the GC column. The main driving principle behind a TCD is joule heating of a conductive filament and measuring the resistance changes according to the thermal conductivity of the gases passing over it. To obtain further insights on the heat transfer phenomena, first a model of the microbridge was simulated in COMSOL 4.4. Next, the stability of the micro-fabricated MEMS sensor was investigated by inserting a single MEMS TCD in helium gas flow. The TCD data reveal that the effect of the flow rate is small, due to formation of a small thermal boundary layer around the microbridge. Therefore it only interacts with the low speed laminar sublayer in the flow channel, and as a result, the effect of bulk flow speed is minimal for standard flow rates for GC applications.

### **1.6 Proposed Solution: Study the VOC Gases Released by *Armillaria***

Initially, a GC-MS system was used to identify the VOCs gases associated with *Armillaria* fungi, by collecting and analyzing the VOC overhead space of an agar sample and comparing

it with an inoculated agar with *Armillaria*. After identifying the VOC associated with *Armillaria*, a mixture of twenty one VOC compounds was prepared and injected into the MEMS GC system to compare it with a bench top GC system. The MEMS GC system successfully separated and detected all the twenty one compounds in less than 3 minutes.

## Chapter 2

### COLUMN PERFORMANCE THEORY

Chromatographic measurements are typically described by plate height ( $H$ ) and plate number ( $N$ ), and the plate heights of two columns with the same length are determined by column width, gas flow, gas viscosity, and stationary phase thickness, each of which is considered. Column performance is characterized by retention time and column efficiency (Band Broadening). Therefore understanding the effects of different parameters on column performance is critical and must be investigated before designing a column.

#### 2.1 Retention Time

Retention time is the time it takes for a sample to reach the detector and is labeled by  $t_R$ , and  $t_M$  is the unretained mobile phase time.

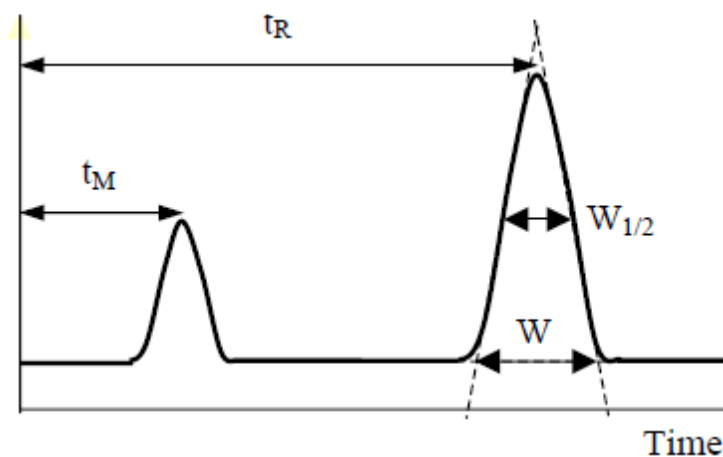


Figure 2-1: Chromatogram of a two component mixture

The chromatogram above shows the chromatogram of a two component mixture. For a given length of the column, the average linear rate of solute migration is defined by

$$\bar{U} = \frac{L}{t_R} \quad \text{Equation 2-1}$$

and the average linear ( $u$ ) velocity of the mobile phase is

$$\bar{u} = \frac{L}{t_M} \quad \text{Equation 2-2}$$

to relate the average velocity of the solute to the average linear velocity,

$$\bar{v} = \bar{u} \times \text{time solute spends in the mobile phase}$$

$$\bar{v} = \bar{u} \times \frac{C_M \cdot V_M}{C_M \cdot V_M + C_S \cdot V_S} \quad \text{Equation 2-3}$$

where  $C_M$  is the concentration of the solute in the mobile phase,  $C_S$  is the concentration of the solute in the solid phase. The equation above could be simplified by substituting  $K$

$$\bar{v} = \bar{u} \times \frac{1}{1 + K \cdot \frac{V_S}{V_M}} \quad \text{Equation 2-4}$$

The migration rate of solute is then defined by

$$k = K \times \frac{V_S}{V_M} \quad \text{Equation 2-5}$$

where  $k$  is the retention factor that is widely used for the GC column. Substituting the retention factor back into the equation

$$\bar{v} = \bar{u} \times \frac{1}{1+k} \quad \text{Equation 2-6}$$

And the equation above could be rearranged for  $t_R$  and  $t_M$ .

$$\frac{L}{t_R} = \bar{u} \times \frac{1}{1+k} \quad \text{Equation 2-7}$$

And

$$t_R = \frac{L(1+k)}{\bar{u}} \quad \text{Equation 2-8}$$

## 2.2 Column Efficiency

Chromatographic Efficiency is typically described by plate height (H) and plate number (N), and the plate heights of two columns with the same length are determined by column width, gas flow, gas viscosity, and stationary phase thickness, each of which is considered. Column performance is characterized by retention time and column efficiency (Band Broadening). Therefore understanding the effects of different parameters on them is critical and must be investigated before designing a column. The efficiency of a column is

widely reported as the height equivalent to theoretical plate (HETP) and number of theoretical plates ( $N$ ). These two parameters are inversely related by

$$N = \frac{L}{H} \quad \text{Equation 2-9}$$

where  $L$  is the length of the column. In the MEMS column, low chromatographic efficiency is associated with the reduced length of the column. The concept of the plate height and number first were introduced for a gas-liquid partition chromatograph by James and et al. [40]; their assumption is that a column is made of numerous districts but continuous layers called theoretical plates and was successfully demonstrated for Gaussian shape of chromatographic packs. Therefore, the relation between plate height and number could be presented by

$$H = \frac{\sigma^2}{L} = \frac{LW^2}{16 t_R^2} \quad \text{Equation 2-10}$$

And the plate number

$$N = 16 \left( \frac{t_R}{W} \right)^2 = 5.54 \left( \frac{t_R}{W_{\frac{1}{2}}} \right)^2 \quad \text{Equation 2-11}$$

where  $W_{\frac{1}{2}}$  is the height of the peak at half height.

### 2.3 Gas Flow in MEMS Channel

To study the average flow rate in the column, first the Navier-Stokes equations for an incompressible Newtonian fluid with no slip condition are calculated for the following three geometries.

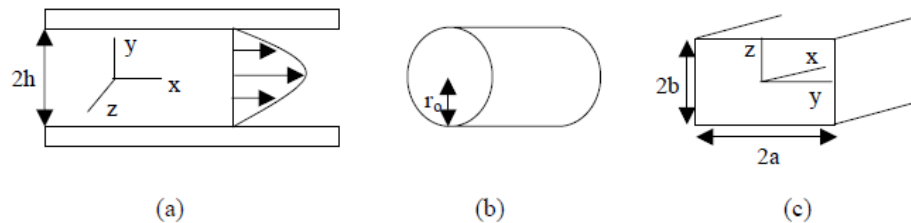


Figure 2-2: (a) Parallel plate system, (b) circular column and (c) rectangular column

Solutions for the Navier-Stokes equations for the three geometries are summarized in Table 2-1. The physics of flow and mass transfer in channels also have been numerically investigated with open source tool, OpenFOAM [41, 42]

Table 2-1: Average linear flow velocity for fixed parallel plates, circular tubes, and rectangle channels

Fixed Parallel Plates	Circular tube	Rectangular Channel
$\bar{u} = \frac{h^2 (P_0 - P)}{3 \mu L}$	$\bar{u} = \frac{r_0^2 (P_0 - P)}{8 \mu L}$	$\bar{u} = \frac{w^2 P_0 (P^2 - 1)}{24 \mu L} f_1$

where  $P_0$  is the outlet pressure,  $P$  is the ratio of the inlet to outlet pressure.  $L$  is the column length,  $\mu$  is the carrier gas viscosity, and  $f_1$  is the Martin-James gas compression coefficient. However, the geometry of the etched silicon columns is more rectangular than circular; therefore, the average velocity of a rectangle channel was used for theoretical calculation. As shown in the rectangular channel average velocity equation, the pressure and width of the channel are the key factors that affect the speed of separation and also separation performance of the GC column.

## 2.4 Maximum Column Efficiency

The Golay and Spangler kinetic model [43] was used to calculate the column efficiency. The column performance is characterized by calculating the column efficiency (Band Broadening) and can be described by Van Deemter equation

$$H = A + \left(\frac{B}{u}\right) + Cu + Du^2 \quad \text{Equation 2-12}$$

where  $A$  is eddy diffusion constant,  $B$  is longitudinal molecular diffusion,  $C$  is mass transfer in the stationary phase, and  $D$  is extra column effects. The eddy diffusion is zero for the MEMS column, mainly due to open tubular column and uniform path through the column. The  $B$  term depends on the type of carrier gas and also the gas velocity. The  $C$  term is the mass transfer in the mobile phase  $C_m$  and stationary phase  $C_s$ . The geometry of the column and the thickness of the stationary phase are important factors that contribute to the column's performance.  $D$  is external column effects.

Table 2-2: Van Deemter equation parameters

Reference	B term	$C_g$ term	$C_s$ term	D term
Golay (round)[44]	$2 D_g$	$\frac{a + 6k + 11k^2 r}{24(k + 1)^2 D_g}$	$\frac{2}{3} \frac{k}{(1 + k)^2} \frac{d_f^2}{D_g}$	$\frac{\Delta t^2}{L(k + 1)^2}$
Golay (rectangle)	$2 D_g$	$\frac{a + 9k + 25.5k^2 w^2}{105(k + 1)^2 D_g}$	$\frac{2}{3} \frac{k}{(1 + k)^2} \frac{(w + h)^2 d_f^2}{D_g h^2}$	$\frac{\Delta t^2}{L(k + 1)^2}$

where  $D_g$  and  $D_s$  are the binary diffusion coefficient in the mobile and stationary phase,  $k$  is the retention factor,  $d_f$  is the thickness of the stationary phase, and  $\Delta t$  is the dead volumes in connection lines.

The work reported here for a round micro-GC column and the Van Deemter equation parameters is modeled for different lengths of column as the function of the uniform velocity. The average carrier gas velocity for rectangular column was used to calculate the plate height versus velocity.

### 2.4.1 Column width theoretical calculations

The column was first optimized as a function of the width. The width of the channel affects the performance of the column in two ways: the velocity of the carrier gas and column efficiency. Column width is a dominant factor in a narrow column, when ( $w \ll 4h$ ). As shown in Golay's equation, the width of the channel is an important parameter that affects the mass transfer term of the equation; hence, influencing  $H_{min}$  and  $u_{opt}$ . As the width of the channel decreases, plate number increases, hence improves the column efficiency.

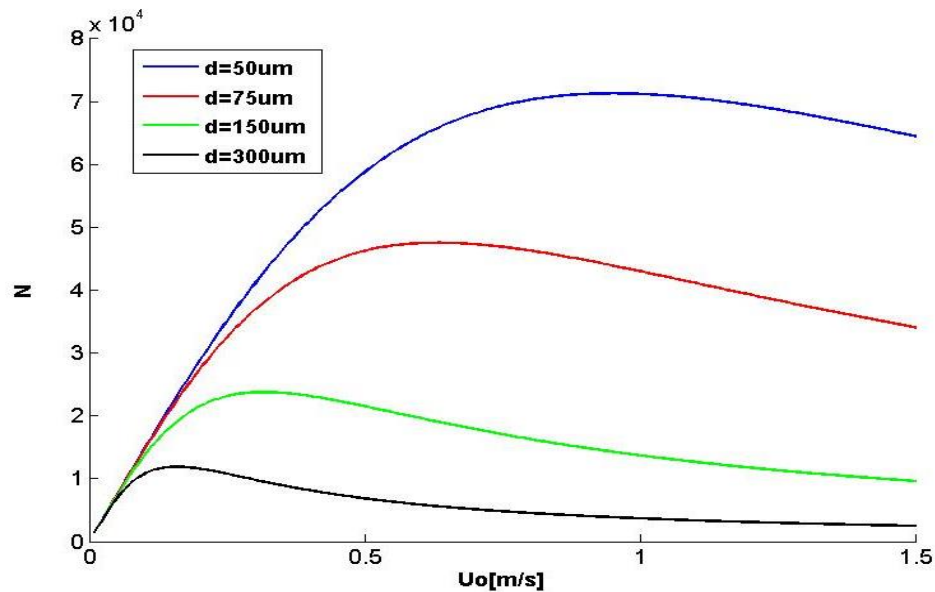


Figure 2-3: Effect of column width for a 3 meter column

As shown in Figure 2-3, reducing the column width increases the number of theoretical plates drastically. Initially, the height of the column was fixed at 300  $\mu\text{m}$  as the effect of height on the column plate height is small. Next, the optimum flow velocity and the corresponding plate height for a 50  $\mu\text{m}$  channel were investigated and plotted in Figure 2-4. The velocity corresponded to the minimum plate height was calculated.

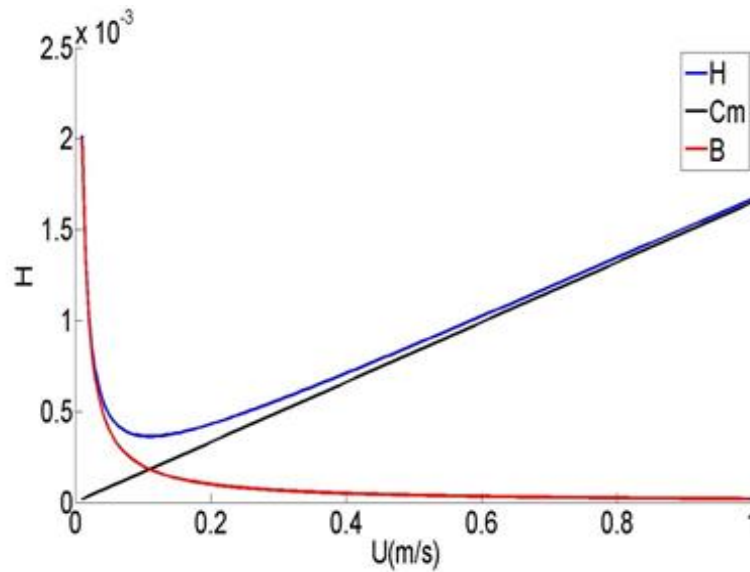


Figure 2-4: Plot of the optimum velocity and plate height for the 50  $\mu\text{m}$  channel column.

### 2.4.2 Column Length

The length of the column is an important factor that has a linear correlation to the plate number; therefore, by increasing the length of the column, the plate number increases significantly. Figure 2-5 shows the correlation between the plate height and the carrier

gas velocity. As shown in the figure, for a fixed column diameter, the plate number increases, but optimum velocity remains relatively the same.

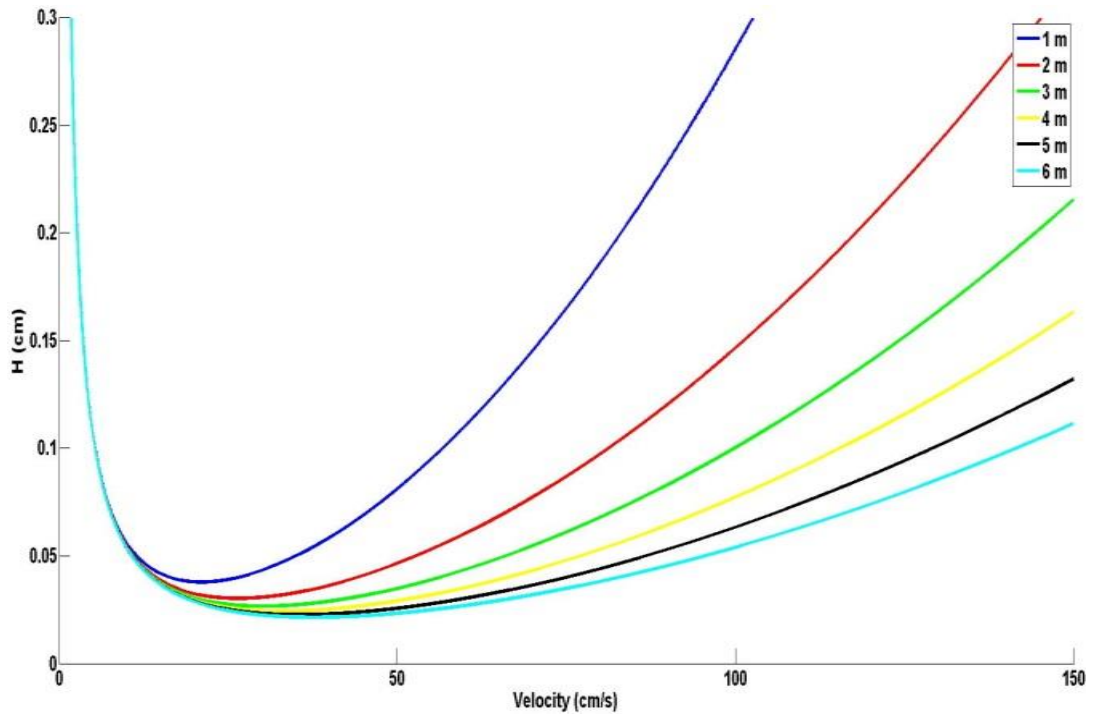


Figure 2-5: Plot of height equivalent to the theoretical plate versus average carrier gas (Helium) velocity for a different length of the column.

The table below summarizes the plate number values for the 50  $\mu\text{m}$  channel with different lengths.

Table 2-3: Golay's Equation parameters for the MEMS GC system

Length in meter	1	2	3	4	5	6
B	0.174	0.174	0.174	0.174	0.174	0.174
C	2.2 E-3					
D	8.21E-06	8.21E-06	8.21E-06	8.21E-06	8.21E-06	8.21E-06
H min (cm)	0.0379	0.0303	0.0266	0.0244	0.0227	0.0215
N	2639.22	6539.22	11261.30	16427.10	21997.40	27920.00
U optimum (cm/s)	20.91	26.91	30.41	32.81	35.96	37.81

## 2.5 Final Design Considerations:

The overall design features a center entry capillary interconnect with no modification of the gas column and a side outlet capillary to a detector. The plate height (H) and plate number (N) of columns with different lengths are determined by the column width, gas flow, gas viscosity, and stationary phase thickness, each of which was considered in section 2.4. In this section, we investigate the effect of the channel dimensions and geometry on the average flow velocity for the column lengths of 2 and 3 meters and channel widths of 50 and 75  $\mu\text{m}$  in order to maximize the plate number. Note that two geometries (rectangle and circular) are chosen to accommodate unintended variances in temperature gradient on the chip and also to improve the uniformity of the stationary coating.

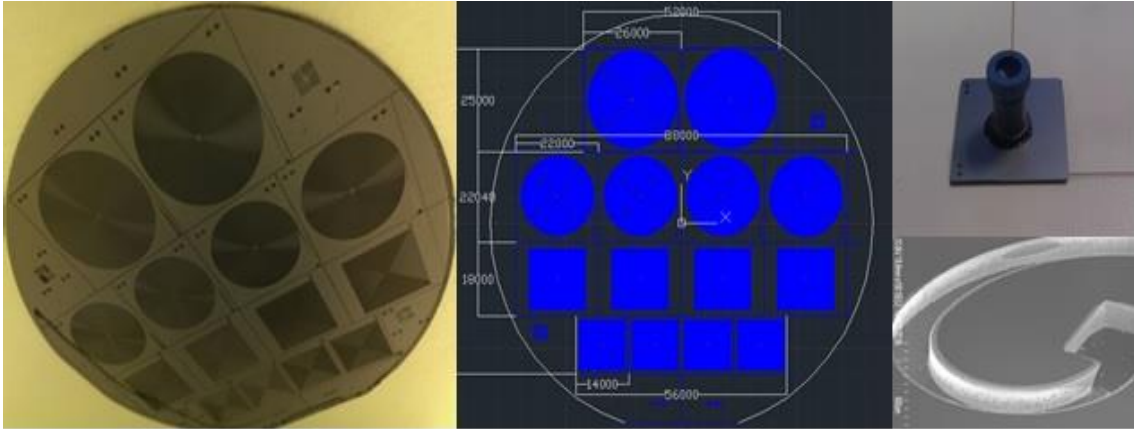


Figure 2-6: (a) Schematic of 2 and 3 meters GC column and the final column (b) mask layout of the column (c) final column (d) etch profile of the column

Here we design and perform both analytical and experimental validation of a high performance GC column using OV-1 as the stationary phase for separation of twenty VOC gases commonly released by the *Armillaria* fungal infection of plants. The miniaturized GC column was first optimized as a function of dimension by a numerical analysis, design and experimental validation follow

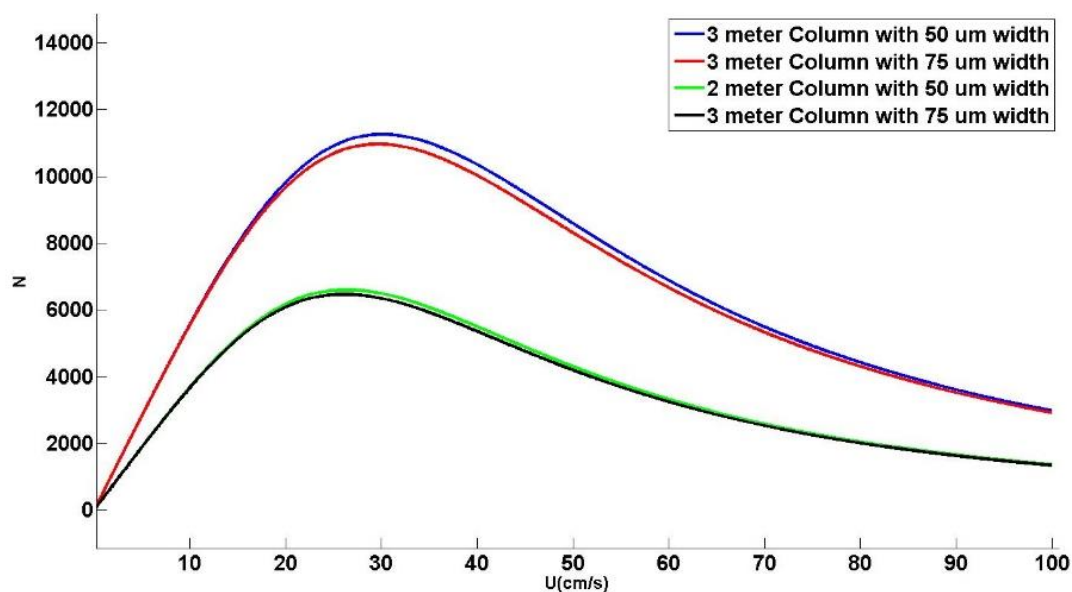


Figure 2-7: Effect of column width and length for 2 and 3 meters column with 50 and 75 diameter width (Height is 300 $\mu$ m, k=5, P=8.5 psi)

Note that columns of two different lengths (2m and 3 m) and two different widths (50  $\mu$ m and 75 $\mu$ m) were chosen to accommodate a higher plate number[45].

Table 2-4: Column properties for the different column lengths

Column Length	Geometry	Surface Area	Chip size	Volume
3 m	Helix	1.5 cm <sup>2</sup>	2.6 cm X 2.5 cm	0.053 cm <sup>3</sup>
2 m	Rectangle	1.0 cm <sup>2</sup>	2.2 cm X 1.8 cm	0.035 cm <sup>3</sup>
3 m	Helix	2.25 cm <sup>2</sup>	2.2 cm X 2.2 cm	0.078 cm <sup>3</sup>
2 m	Rectangle	1.5 cm <sup>2</sup>	1.4 cm X 1.4 cm	0.053 cm <sup>3</sup>

## Chapter 3

### PROCESS DEVELOPMENT OF ALL SILICON GC COLUMN

This work highlights a new bonding technique for micro-fabrication of an all silicon 3-meter gas chromatography column that could withstand the temperature cycling required for axial temperature programming. Proper separation of a complex gas mixture using a miniaturized GC column is critical to improve the overall performance of the lab on a chip systems for environmental monitoring, medical diagnoses, and gas impurity measurement. To improve upon current methodology, the column was first fabricated using micro fabrication processes; experimentally validated using a high performance 3-meter GC column coated with OV-1 stationary phase. This process demonstrates that the quality of the bonding between a GC column and a 200 um thick silicon lid was improved when using a new gold eutectic bonding technique. This was further evaluated at higher pressure. Furthermore, a new quality control technique was developed in order to test the overall bonding quality of the column by fixing the bottom column and applying a mechanical shear force to the top lid. This method could ultimately be used for quality control of each individual bonded column. The gold interface of the gold diffusion bonded area is further characterized using SEM and EDX imaging. In the end, the utility of the column was demonstrated by separating a mixture of six hydrocarbon compounds with different Kovats retention indices and molecular weights in less than five minutes.

### 3.1 Introduction

GC columns are the heart of the system where separation takes place; therefore, properly sealing the micromachined GC column is a critical step in improving system integration and overall performance. Several techniques have been developed for bonding and sealing MEMS micro-GC columns, such as anodic bonding [23], gold eutectic bonding [46], and fusion bonding [47].

Anodic bonding is a well-established technique for properly sealing micro-channels columns and currently accounts for packaging the majority of the silicon microfabricated GC columns [16, 22, 23] [28]. Among the many methods available for bonding a high density micro-machined surface, anodic bonding is possibly the one with the lowest capital cost, while offering a strong bond. However, its main disadvantage for the micro-GC column is the necessity of bonding silicon to a material with sufficiently different thermal conductivity such as Pyrex® glass. High frequency temperature cycling of a GC column comprised of two materials with different thermal expansion coefficients and thermal conductivities enhances fatigue cracking, reduces fatigue life, and influences non-uniformity in the temperature profile. As a result, anodic bonding of a Pyrex® glass lid to a micro-machined silicon column reduces the overall column efficiency while it requires additional power to reach a steady-state temperature.

Fusion bonding, while an easy and low cost bonding technique, presents many challenges due to the rough surfaces of the micro machined GC column. The rough metrology of the micromachined surfaces enhances formation of small voids and gaps between the two bonding pieces. Previously, our attempts to perform direct silicon-silicon

bonding without an intermediate layer have failed. We observed only the partial bonding of silicon, which was mainly due to the high roughness and contamination on the surface of the column. Finally, the gold eutectic bonding as a standalone method does not create a durable bond to withstand the high pressure condition needed for GC column operation [26]. Even though all these techniques are available for packaging a GC column, none of these techniques is ideal for bonding a high density micro-machined surface.

This chapter introduces a novel bonding technique for micro-fabrication of all silicon 3-meter gas chromatography columns. The bonding technique enables sealing of a GC column that withstand the temperature cycling and decrease degradation over time. This method eliminates the need for anodic bonding and provides a better temperature uniformity when operates at a higher temperature.

To improve the bonding quality, we performed a two-step process: First, the two pieces were bonded temporarily using gold eutectic bonding at the eutectic temperature of the gold, followed by the annealing step by placing the pre-bonded column in a furnace at 1200 °C for one hour. The bonding strength was then quantified by connecting the GC column to a compressed nitrogen system with a controlled bleed to an ambient valve. The quality of the bond interface was further characterized using SEM/EDX imaging. Finally, a new bonding quality control test was developed by measuring the displacement of the bonded column while applying a mechanical shear force to the column.

### 3.2 Micro Fabrication Process of all Silicon GC column

The microfabrication of the column started with a 4 inch diameter P doped silicon wafer (0.5-0.42 Ohm-cm 500-550  $\mu\text{m}$  SSP prime Grade). Megaposit SPR 220 photoresist was spin-coated on the wafer at 2000 rpm for 50 seconds. The photoresist thickness was measured, using a Nanospect reflectometer, to be around 10  $\mu\text{m}$ . Following a baking step of 3 minutes at 120°C, the wafer was lithographically exposed in order to print the inlets and aligner marks on the backside of the wafer.

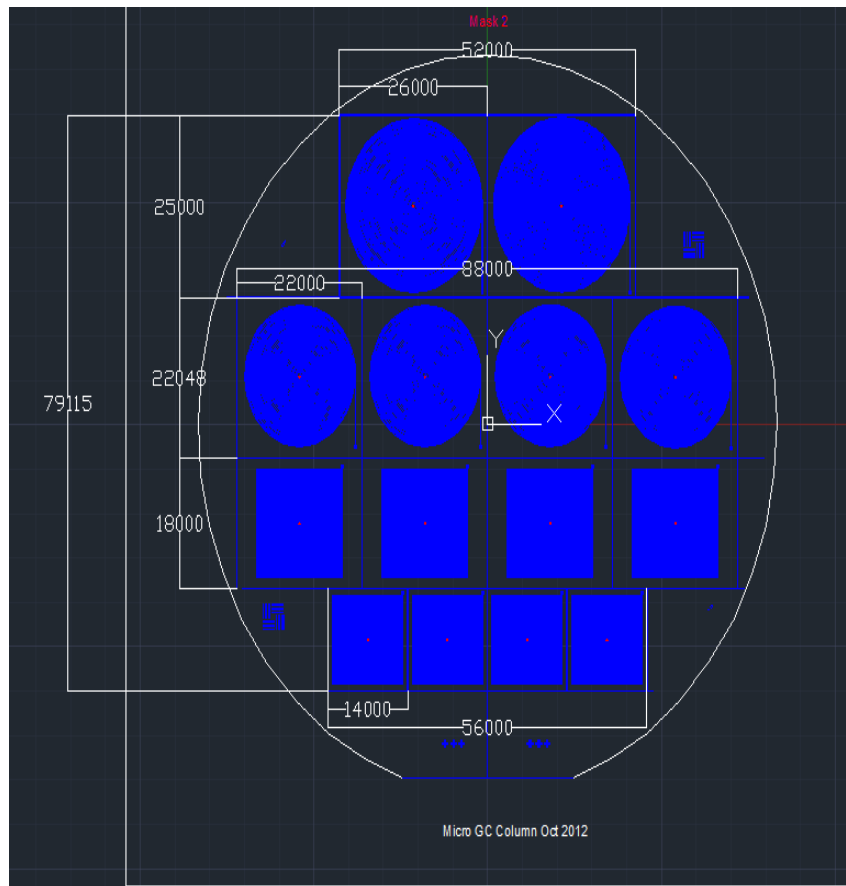


Figure 3-1: MEMS Column MASK Design layout

Next, STS HRM Deep Ion Reaction Etching (DIRE) was used to etch 300  $\mu\text{m}$  height holes anisotropically in the silicon. During the DIRE process,  $\text{SF}_6$  and  $\text{C}_4\text{F}_8$  were used for etching and passivation layer deposition respectively. Different power levels and passivation times were tried, and the best etch rate with the smoothest wall profile was selected. The etch rate was measured to be  $\sim 0.9 \mu\text{m}/\text{cycle}$ .

Table 3-1: Etching Rate STS HRM

<b>Test</b>	<b>number of Cycle</b>	<b>Etch</b>	<b>Ramp rate</b>	<b>Passivation</b>	<b>Ramp rate</b>	<b>Mask</b>
1	300	2200	5	1500	0.5	SiO <sub>2</sub> Mask
2	300	2200	4	1500	0.4	SiO <sub>2</sub> Mask
3	300	2200	3	1500	0.3	PR Mask (4 $\mu\text{m}$ )
4	200	2200	2	1500	0.2	PR Mask (4 $\mu\text{m}$ )
5	300	2200	3.5	1500	0.3501	PR Mask (4 $\mu\text{m}$ )
6	300	2200	3.3	1500	0.33	PR Mask (4 $\mu\text{m}$ )
7	400	2200	3.5	1500	0.35	PR Mask (3.2 $\mu\text{m}$ )
8	400	2200	3.5	1500	0.35	PR Mask (8 $\mu\text{m}$ )
9	250	2200	3.5	1500	0.35	PR Mask (8 $\mu\text{m}$ )

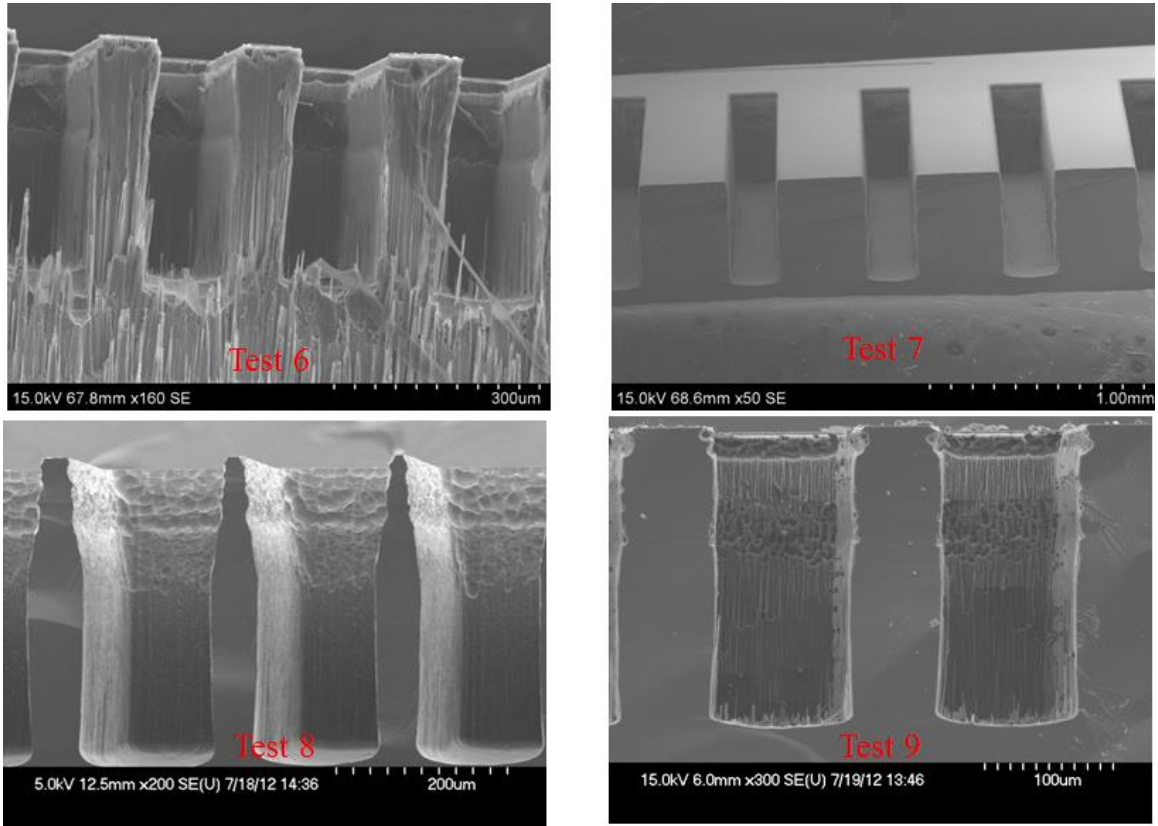


Figure 3-2: STS HRM etch quality for different power and etch rates

The resist layer was removed using acetone, and the wafer was cleaned with piranha solution for 20 min. The same resist coating procedure was repeated on the back side of the wafer. Next, a 400 nm thermal oxide mask layer, was thermally grown using a Tystar nitride furnace. The column pattern was transferred on top of the wafer by the backside alignment technique. Mask aligner aligns the inlet of the columns with the 200 µm diameter inlet port holes etched in the previous steps. The oxide mask layer was removed using a BOE 6:1 wet etch process, opening the channels for the dry etch step. DRIE was used to etch through the wafer and open the inlet capillary fittings to form the 300 µm in height channels on top of the wafer. The resist layer was then removed using acetone. A thin layer

of silicon oxide was grown thermally and subsequently removed by buffered oxide etch (BOE) to reduce the surface roughness of the silicon surface inside the channel. Reducing the channel roughness ensured uniform stationary phase coating. The wafer was diced and rinsed with DI water.

A double sided polished 4 inch dia. P doped silicon wafer (0.5-0.42 Ohm-cm 200-225  $\mu\text{m}$  SSP prime Grade) was cleaned and coated with 20 Angstrom titanium adhesion layer following 100 nm gold using Denton Explorer electron beam evaporator. The wafer was diced to match the exact dimensions of the previously fabricated chips. Both the column die and the lid were cleaned in piranha solution for 20 minutes at 120°C and subsequently dipped in to the BOE solution for 2 min to remove the native oxide from the silicon die. The dies were rinsed with DI water for 5 minutes and nitrogen blow dried. The two dies were brought into contact within a minute of drying, then they were placed in a Karl Suss SB6 wafer bonding tool. The tool's temperature and pressure were set to 420°C and 10 MPa respectively.

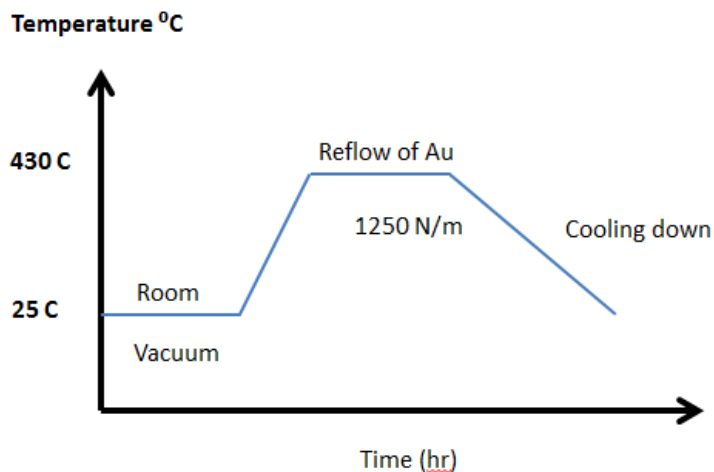


Figure 3-3: Temperature and pressure programming of SB6 wafer bonder

The bonded dies were annealed at 1200 °C (Tystar furnace: 2500 sccm N<sub>2</sub>, 2 hours) for two hours to ensure that gold atoms diffused into the silicon and formed a gold-silicon alloy. Formation of the gold-silicon alloy improves the bonding strength and reduces the stress. Next, the columns were coated with (Ohio Valley) OV-1 stationary phase. Figure 3-4 shows the process flow for fabrication of the entire silicon micro-GC column and reported in [45, 48]. Processing run sheet was developed and is described in Appendix A.

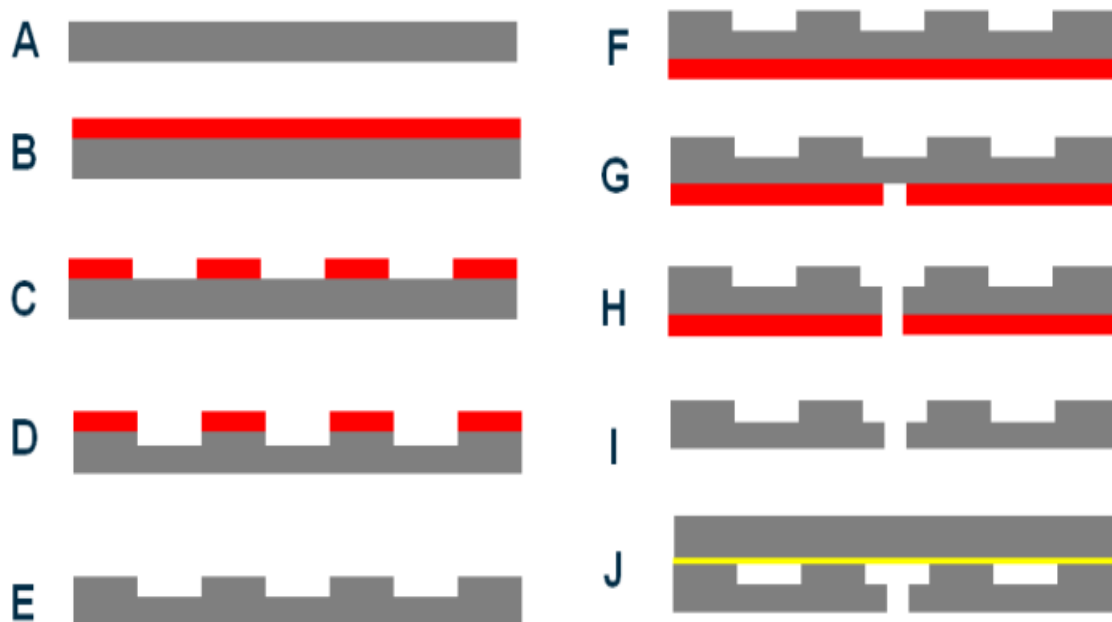


Figure 3-4: Process flow for fabrication of micro-GC column: A) 500  $\mu\text{m}$  (100) silicon wafer; B) Resist spin coating; C) Channel lithography; D) STS HRM Deep RIE; E) Resist stripping; F) Back side resist spin-coating; G) Alignment and lithography; H) Deep IRE of input hole; I) Resist stripping; and J) 200 nm gold deposition on a wafer and wafer bonding.

After fabricating the GC column, a LEXT Laser microscope was used to characterize the column profile. As shown in Figure 3-5, the average column height is about 320  $\mu\text{m}$  and the channel width is 65  $\mu\text{m}$ .

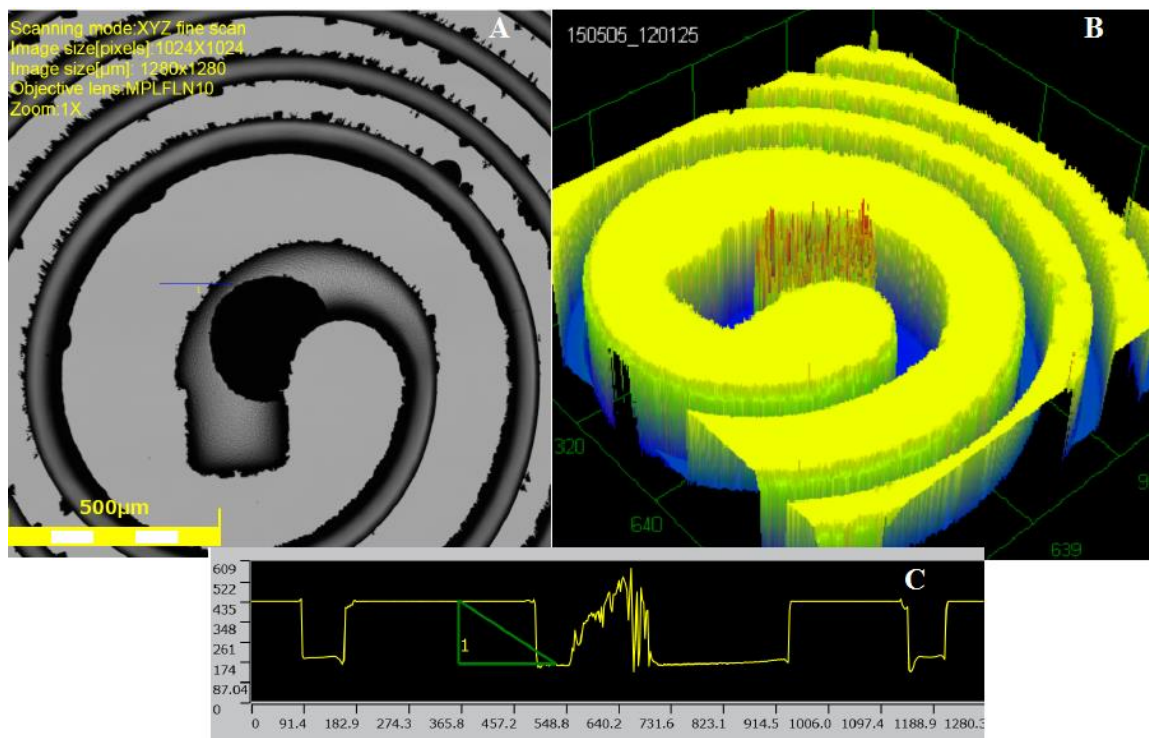


Figure 3-5: LEXT imaging A) Top View, B) 3-D view C) profile measurement

### 3.2.1 Nano Port Bonding Setup

The inlet of the GC column was connected to a 250  $\mu\text{m}$  diameter fused silica (FS) capillary via NanoPort fitting. The NanoPort fitting was aligned with the inlet hole on the chip and cured in a convection oven at 320  $^{\circ}\text{C}$  for an hour. The outlet was connected to the same diameter fused silica by inserting the capillary into the pocket etched in silicon and epoxy sealing the capillary using Miller-Stephenson epoxy 907 adhesive. Figure 3-6 shows the schematic of a 3-meters GC MEMS column and the etch profile.

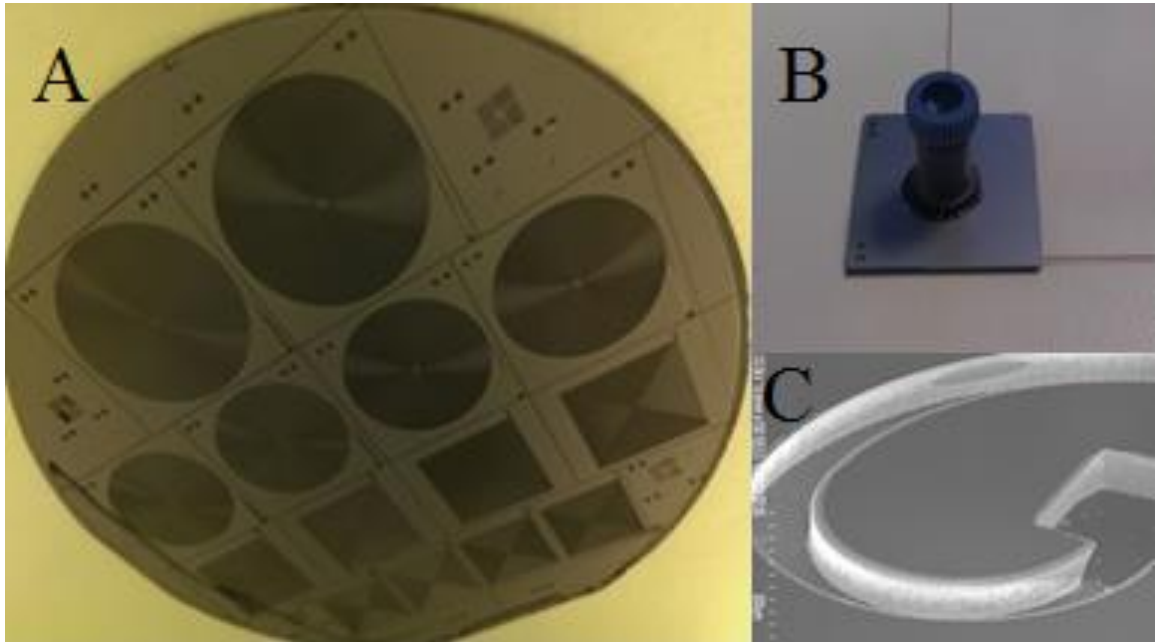


Figure 3-6: (a) Schematic of 2 and 3 meters GC column, (B) 3 meters MEMS GC column, and (C) etch profile of the column.

Figure 3-7 shows the experimental setup for connecting the NanoPort to the MEMS column. The MEMS column is clamped in the holder, which was built by milling aluminum.

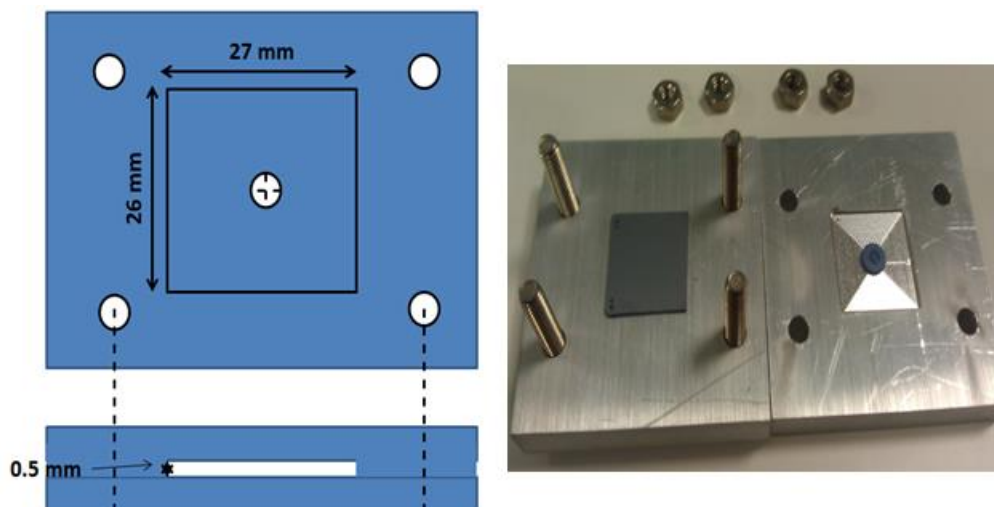


Figure 3-7: NanoPort Adaptor attachment setup

### 3.2.2 Column Stationary Phase Coating

Stationary phase coating is the most important step in developing a GC column. The performance of the GC column is highly impaired by the non-uniformity and bad quality of the coating. The most common methods for coating the stationary phases are static and dynamic. Static coating is the standard coating technique for coating commercial GC columns mainly due to its good coating uniformity. In static coating, a column is filled with a dilute solution of stationary phase in a suitable solvent. One end of the column is sealed to control the evaporation of the solvent, and a vacuum is applied to the other end of the column to form a uniform stationary phase coating on the inner wall of the column. The thickness of the stationary phase was calculated based on the viscosity of the coating solution to be around 3  $\mu\text{m}$ . In Dynamic coating, the Column is filled with a dilute solution of the stationary phase, and positive pressure is applied to remove the excessive solvent.

The thickness of the stationary phase using this method is a function of air velocity and the concentration of the stationary phase. For this study, one of the most common non-polar stationary phases, OV-1 (Ohio Valley) was selected for coating the column using both static and dynamic methods.

Dynamic coating of the GC column was also attempted at different concentrations, 0.1, 2, and 5 % (weight to volume) in toluene. First the column was filled with the stationary phase solution, and the excessive solution was removed by pressurizing the column at 40 psi for 2 minutes. Next, the pressure was reduced to 0.2 psi, and the column was left to dry at 120 °C overnight. In this work we present the data for 5% (W/V) OV-1 coating. The stationary phase coating using dynamic methods was calculated to be 1  $\mu\text{m}$ .

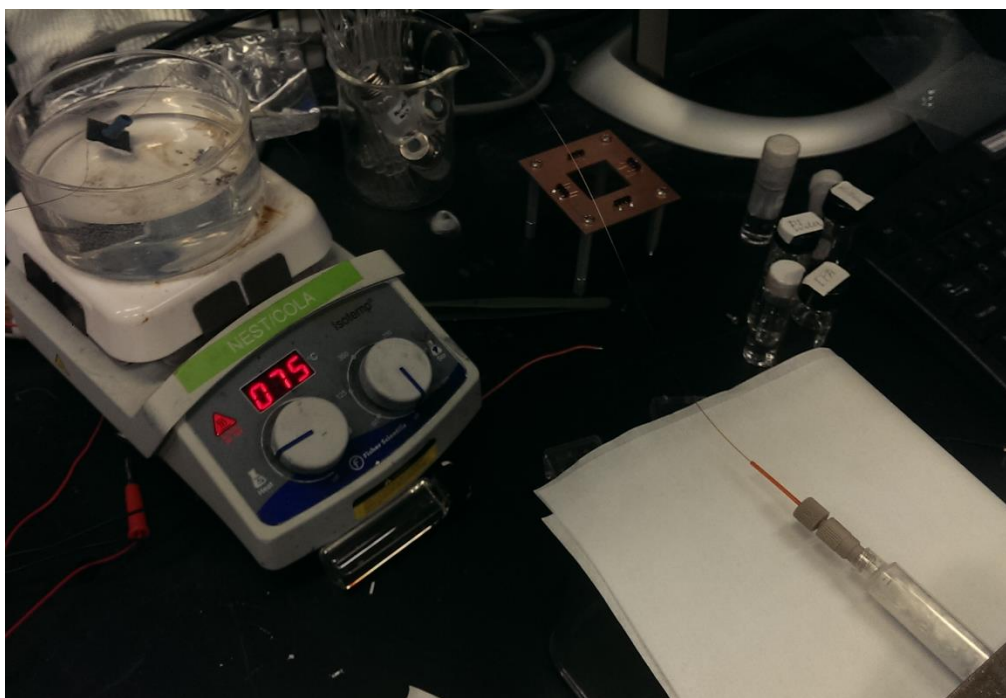


Figure 3-8: Stationary coating setup

### 3.3 Bond Quality Characterization

The bonding strength was quantified by connecting the GC column to a compressed nitrogen system with a controlled bleed to ambient valve. The pressure in the column was controlled by the flow rate of the bleeding gas into the column, and a pressure transducer was integrated to measure the pressure difference. The gold eutectic fusion bonded column demonstrated sealing up to 90 psi compared to the gold eutectic bonded column which failed at 40 psi. Furthermore, the bonding strength was tested by insertion of a flat tweezer between the bonded pieces. The gap between the two pieces of gold eutectic fusion bonded was small enough to prevent insertion of the tweezer. Finally, the quality of the bond interface was characterized using SEM imaging

#### 3.3.1 SEM Imaging

The SEM images presented in Figure 3-9 show formation of a continuous silicon interface.

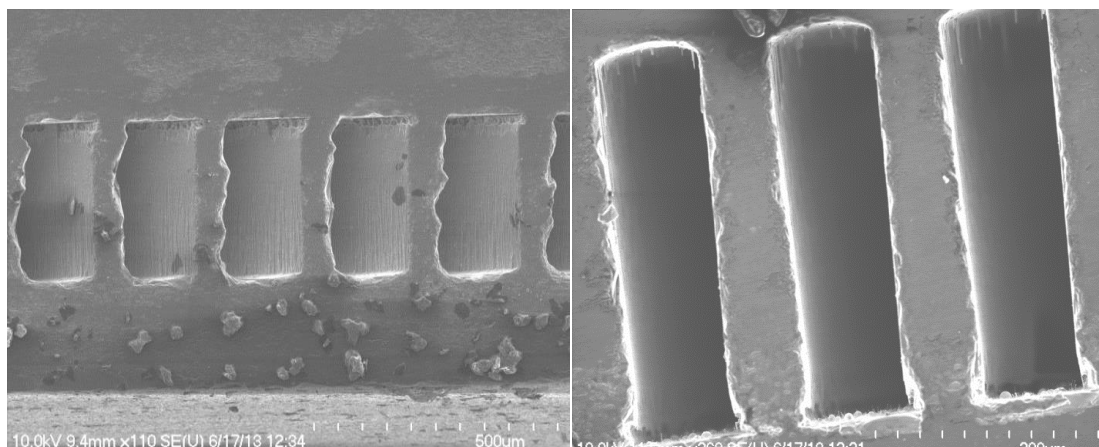


Figure 3-9: SEM images of cross-section of the gold fusion bonded column.

The bonding interface of the micro-column was further analyzed using SEM/EDX Zeiss to study the bond formation and micro-voids characterization. Area 1, boxed in Figure 4, shows the gold eutectic bonding area and area 2 is silicon. These voids are suspected to be the gold-silicon composite alloy. The heat treatment profile affects the diffusion rate and densification, as well as the residual stress development in the bonding area. The diffusion coefficient of gold in silicon is reported to be  $1.1 \times 10^{-7} \text{ cm}^2 \cdot \text{s}^{-1}$  [49], and the diffusivity and solubility of gold into silicon increase at higher temperatures. Therefore, at higher temperatures a thicker layer of gold silicon alloy forms, and a stronger eutectic bond is expected. Temperature and processing time are the key factors that affect the quality of the eutectic bond. A high amount of energy is needed for atoms to overcome the diffusion boundary and form a strong gold-silicon bond. Therefore, at higher temperatures, gold atoms have sufficient energy to diffuse into silicon and form an alloy.

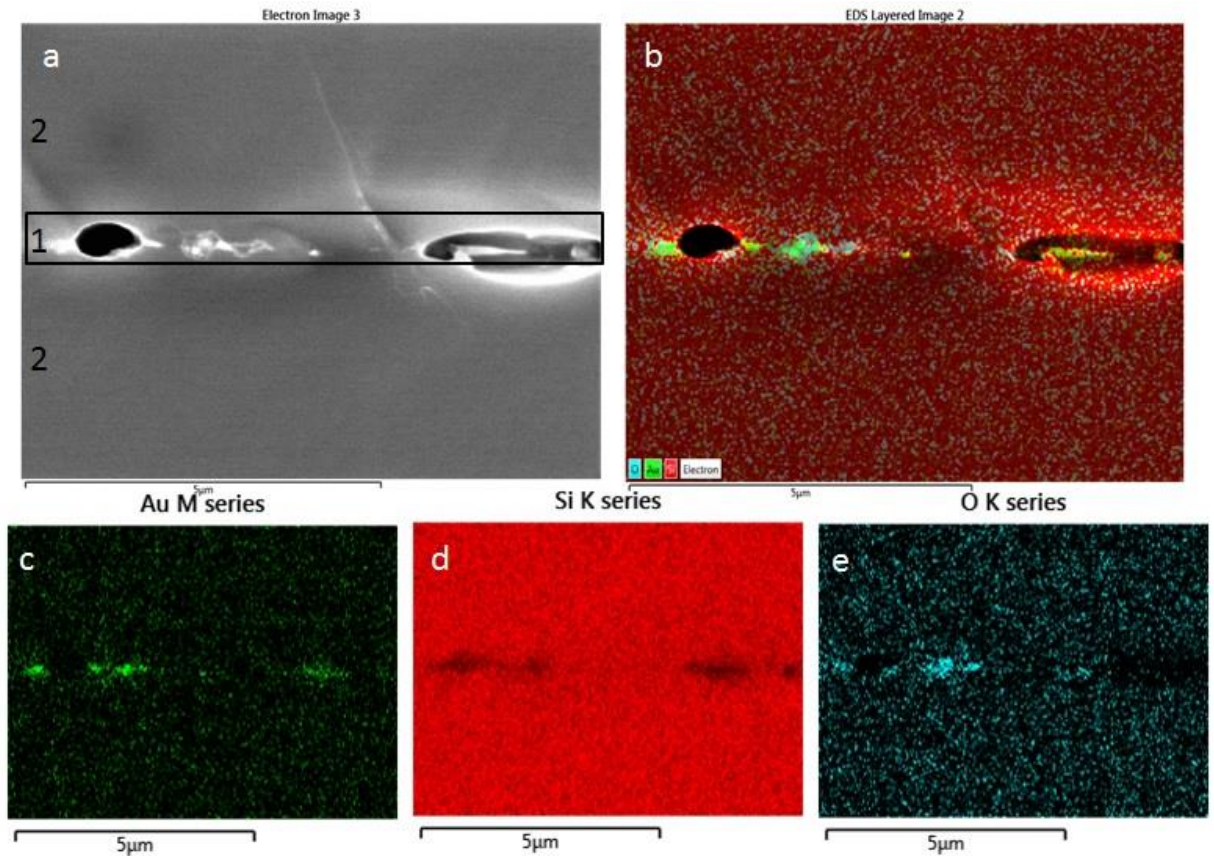


Figure 3-10: a) SEM images of the bonded interface of gold eutectic bonded; b) Energy dispersive X-ray showing the Au richness around the bonded area; and c) Location of gold atoms at the interface, d) Location of silicon atoms, e) location of oxygen

### 3.3.2 Mechanical Shear Test

Furthermore, a new mechanical shear test was developed to evaluate the bonding strength of the GC column. A 22 mm by 22 mm column die was diced into sixteen 3.5 mm by 3.5 mm pieces, and the bonded area was calculated. A Dage 4000 was used to perform a die

shear test using a 100 kg cartridge. Figure 3-11 shows the experimental setup of the die shear test and the direction of the shear. The shear height and speed were set at 100  $\mu\text{m}$  and 100  $\mu\text{m/s}$  respectively. Experimental parameters are summarized in Table 3-2.

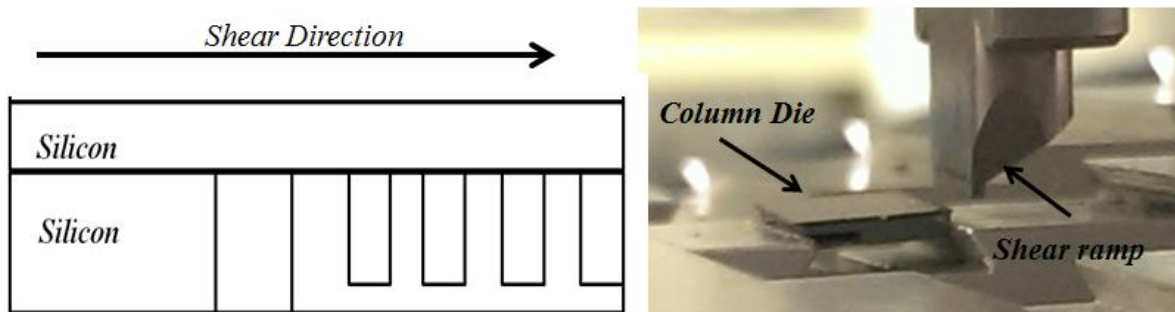


Figure 3-11: Die Shear Test setup

Table 3-2: Shear Test Parameters

Cartridge DS 100KG	Range 100 kg
Sample Size	3.5 mm X 3.5 mm
Shear height	100 $\mu\text{m}$
Shear Speed	75 $\mu\text{m/s}$

The maximum mechanical shear load for each sample was measured and plotted in Figure 3-12 and reported in Table 3-3. The average shear strength of seven samples is 4.67 MPa, which is adequate to the standard GC operating pressure range. The average shear strength of the gold eutectic bonded GC column was much lower than the column bonded by

previously reported fusion bonding and fusion-eutectic bonding. This was due to the high density surface machined area and also the limited surface area available for bonding.

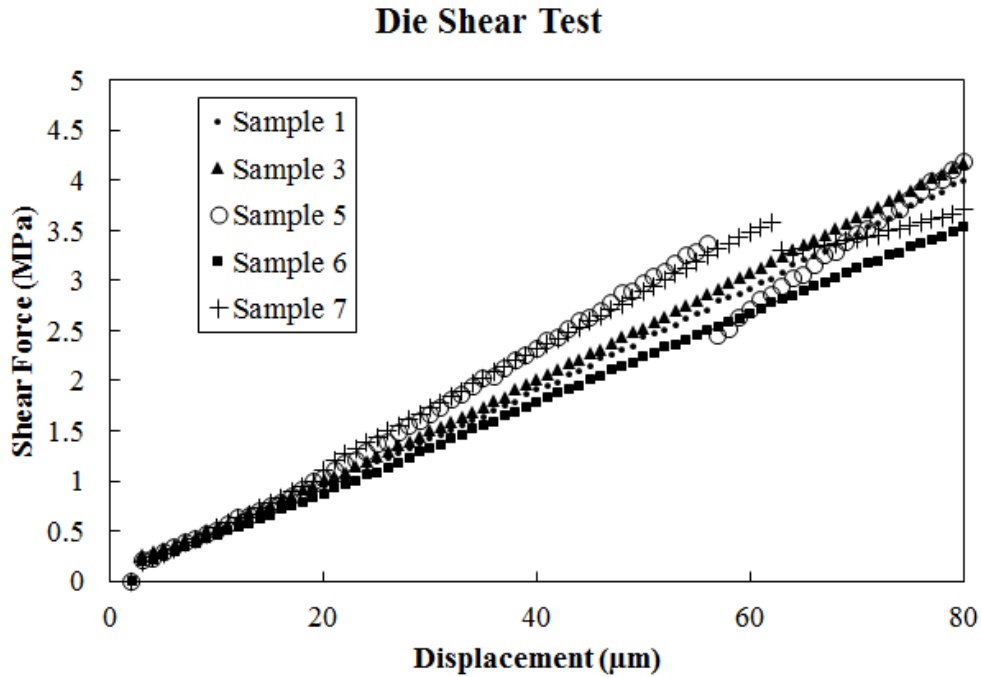


Figure 3-12: Shear test results of seven samples

Table 3-3 summarizes the shear test results for the seven samples. The average, standard deviation, max and min were calculated to provide a better understanding of the test parameters.

Table 3-3: Shear Test Results

Shear Test results	
Average	4.67 MPa
Standard deviation	0.69 MPa
Max	5.71 MPa
Min	3.59 MPa
Number of Samples	7

### 3.3.3 Chromatograph

After validating the bonding strength of the column, the bonding quality was further examined by the gas chromatography technique. Testing was performed by attaching the inlet of the GC column to an HP 6890 GC-FID system and changing the pressure over a wide operating range. For this experiment, the column temperature was kept at 30 °C isothermally, the inlet temperature set at 250 °C with a 1:150 split ratio. Helium was used as the carrier gas, and 1 µL of butane solution was injected for each pressure set. Figure 3-13 shows the chromatographs of butane at four different pressure levels. As shown in the figure, the peak shape and the total area under the curve remained constant for each inlet pressure; hence, no voids and crevices were observed[48].

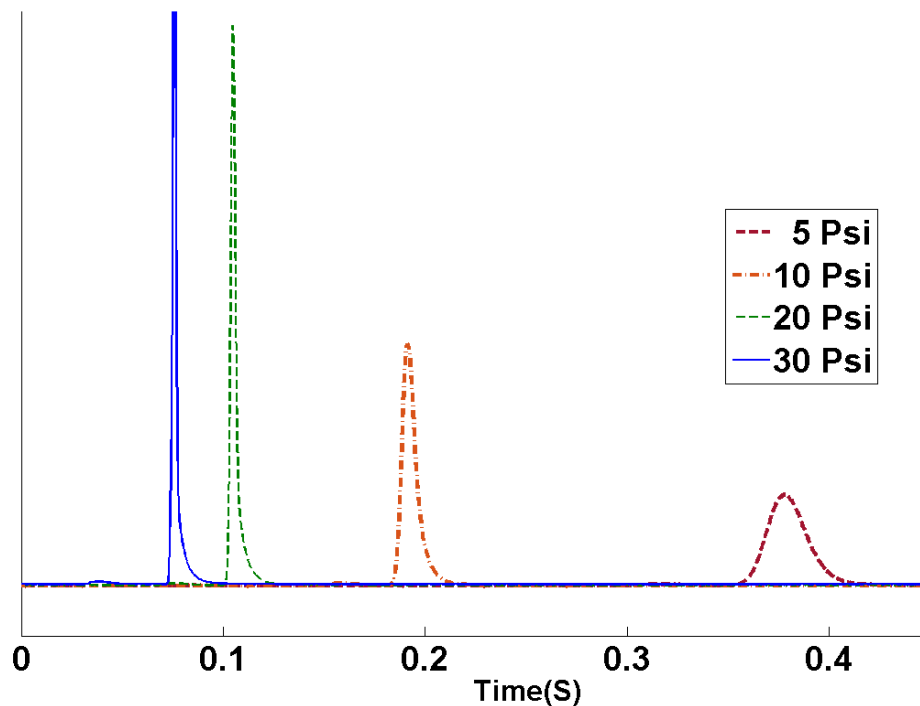


Figure 3-13: Chromatographs showing retention time of 1 µl of butane with split ratio of 150:1

### 3.3.4 Column Efficiency

Furthermore, the performance of the GC column was evaluated to explore the separation capabilities of the column for a mixture of compounds listed in Table 3-4. The column was connected to an HP 6890 Fast-FID, and the chromatograms of the 6 compounds were obtained by injecting 0.2 µl of the sample (split ratio of 400:1, Pressure 16 psi, and temperature 80 °C).

Table 3-4 Column test mixture components

	Compound	Kovats
1	C9	900
2	C10	1000
3	1-octanol	1058
4	linalool	1087
5	C11	1100
6	C12	1200

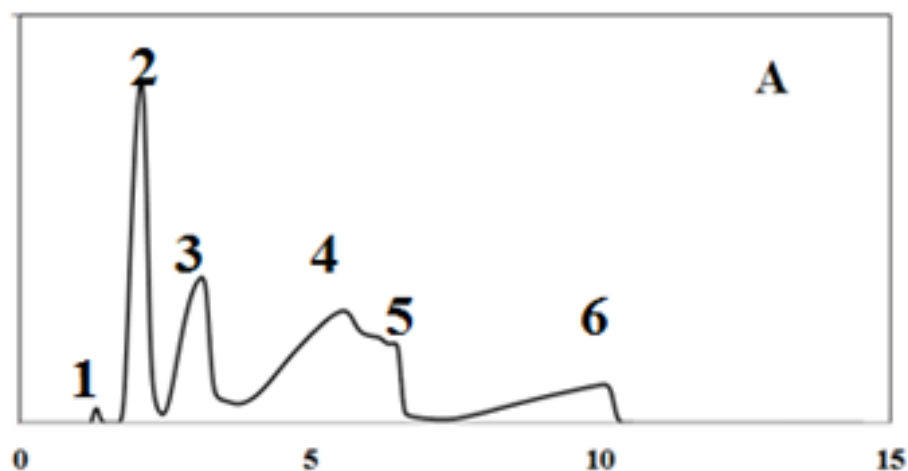


Figure 3-14 : Chromatograph achieved using the 3-meter HP-1 column at pressure 10 psi and inlet temperature of 240 °C

The performance of a standard 3-meter capillary column is not comparable to a MEMS GC column, due to its geometry and the uniformity of the stationary phase coating. However, to demonstrate the effectiveness of the 3-meter GC column, a 3 meter HP-1 column was used to separate the same six compounds previously separated by the MEMS GC and depicted in the Figure 3-14.

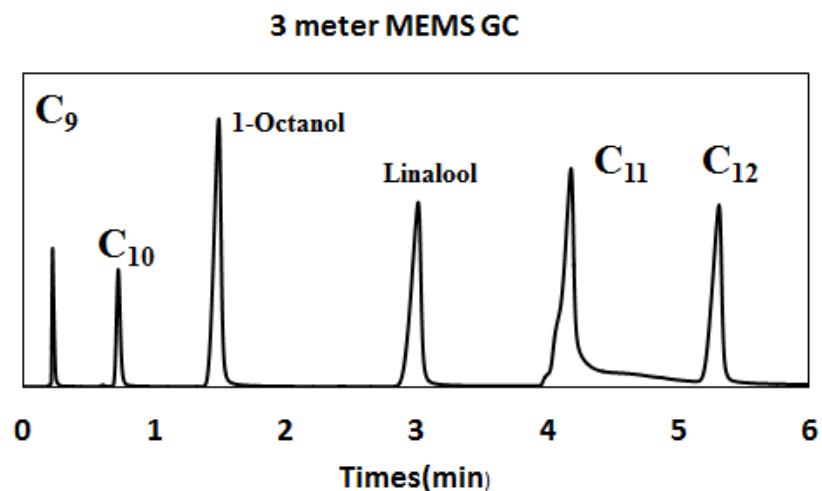


Figure 3-15: Chromatograph achieved using a 3 meter MEMS GC at pressure 16 psi and inlet temperature of 240 °C and isothermal at 80 °C for the first 2 min and ramp 10°C/min to 120°C

The resulting column efficiencies were calculated to be 3400 plates/m, which suggests small non-uniformity in the thickness of the stationary phase. Compared to the static coating, the dynamic coating method reduces the column efficiency; however, selected for simplicity.

### 3.4 Summary and Conclusion

This work demonstrates a new gold eutectic-fusion bonding for micro-fabrication of an all-silicon 3-meter gas chromatography column with a small footprint. The high temperature annealing technique was critical in improving the silicon bond quality, and the shear force measurement confirmed that an effective permanent bond was formed. The

bonding quality measurement using a mechanical force-displacement test can be used for quality control of the bonded columns. Characterization of the interface using SEM and EDX imaging indicated that the gold had diffused into the silicon surface, with little if any remaining at the interface. Evaluation of the columns by measuring the retention time for butane at different inlet pressure levels showed a clearly resolved peak with decreasing retention time at higher pressure. The utility of the silicon 3-meter column was demonstrated by separating a mixture of twenty one compounds with different Kovats retention index and molecular weights.

## **Chapter 4 : AXIAL HEATING DESIG**

One of the main limitations of the current MEMS GC systems is their high power consumption and separation time. In this chapter we introduce a novel, two dimensional axial heating technique for faster and more precise temperature programming, resulting in an improved separation performance. First, three different axial resistive heater designs were simulated theoretically on a  $3.0 \text{ m} \times 300 \text{ }\mu\text{m} \times 50 \text{ }\mu\text{m}$  column for the highest temperature gradient on a  $22 \text{ by } 22 \text{ }\mu\text{m}$  column. Next, the best design was micro-fabricated and evaluated experimentally. The simulation results showed that simultaneous temperature gradients in time and distance along the column are possible by geometric optimization of the heater when using forced convection. The gradients along the column continuously refocused eluting bands, offsetting part of the chromatographic band spreading. The utility of this method was further investigated for a test mixture of three hydrocarbons (hexane, octane, and decane).

## 4.1 Introduction

There have been many efforts to miniaturize the gas chromatography column system since its introduction by Terry [14] and subsequent efforts by Reston and Kolesar [15] in 1990. Sandia National Lab was the first to integrate a GC column, preconcentrator, and chemical sensor arrays into a hybrid system for fast detection of specific analytes commonly present in chemical warfare. Chia- Juang Lu [16] developed the first-generation hybrid MEMS gas chromatograph system, which uses air as the carrier gas and an anodic bonding technique for sealing the silicon etched column to a Pyrex glass. In this system the temperature is regulated using a Kapton embedded resistive wire, and the heat generated by the wire is conducted to the bottom of the column. The limitation of this method is the temperature nonuniformity, and the process of heating the column is slow. Significant progress has been made by different research groups [17-19, 27, 38] to miniaturize the GC system to a portable low power, low cost GC system capable of separating and detecting all the VOCs in a short time; however, band broadening and slow temperature programming are shortcomings of these instruments.

Temperature is the most prominent variable that has significant impact on separation performance, sorbent selectivity and peak spreading of MEMS GC system. Temperature changes the average kinetic energy rate of diffusion and interaction of compounds with the stationary phase. Two methods used commonly for controlling the temperature on a chip are isothermal and temperature-programmed GC. Isothermal GC provides a higher resolution than temperature-programmed, at the cost of a longer

processing time and a relatively narrow boiling temperature range. For both methods, the column maintains a constant temperature at any given time. In 1951, Zhukhoviskii [50] introduced axial temperature gradient where the temperature is not only varying with time but also in location along the length of the column. Axial temperature-programmed in certain conditions demonstrated an effective method for improving the band broadening and band coelution; however, this method wasn't adopted for the standard 30 meter column due to the complexity of controlling the temperature at different locations along the column. Phillips [51, 52] demonstrated the use of an axial temperature gradient by utilizing direct resistive heating on a short standard column capillary; even though they improved the band broadening, they faced many challenges coating the GC column with different thicknesses and generating a temperature gradient. Recently, Zhao [21] demonstrated implementation of this technique on a short micro pack column capillary for separation of a complex mixture of C<sub>1</sub>-C<sub>7</sub>.

The advancements in micro-fabrication processing and the rise of MEMS GC systems make it possible to implement an axial temperature gradient which is impractical for standard capillary GC. Axial heating is a good method to integrate into a MEMS GC system mainly due to the small thermal mass, low power consumption, portability and short analysis time of the columns. Despite the tremendous improvement in separation efficiency, the new GC MEMS column still has not resolved issues such as experimental time, peak coelution, and power consumption, especially for separating a complex mixture. Developing a low powered, faster heating time would be advantageous in shortening the separation time and improving the resolution.

Resistive heaters are the standard methods utilized for temperature programming of MEMS columns. There are two modes: isothermal GC [16] and temperature-programmed [16]. Resistive heater integration on silicon has been demonstrated by many research groups for temperature programming and isothermal analysis; however, the amount of time and power required to ramp and sustain the column at a desired temperature is too large for a portable system.

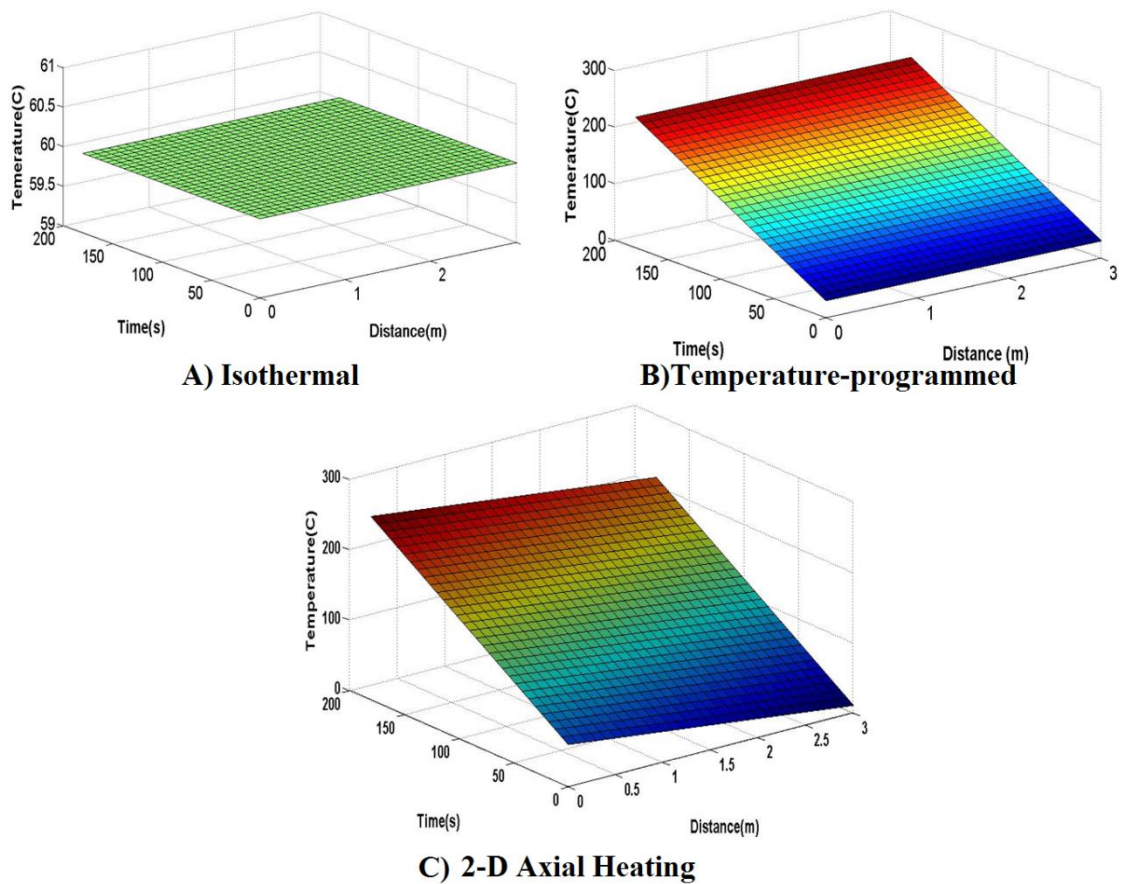


Figure 4-1: MEMS GC thermal programming A) Isothermal B) Temperature-programmed C) 2-D Axial heating

Therefore, fabrication of an all silicon column with a small thermal mass and a heater capable of operating in the temperature ranges of 30-130 °C in less than a minute are vital for fast, low-power, temperature programmed, and portable GC systems.

## **4.2 Experimental Section**

### **4.2.1 Thermal Analysis and Computational Modeling**

Precise temperature control of a GC column is the most important variable affecting separation performance and peak spreading. In conventional GC systems, for precise temperature control and fast ramping, columns are temperature controlled using a convective oven. However, the time and power required to ramp and sustain the oven's temperature for each temperature set-point are critical. As a result, each sample may take several hours to process. In order to reduce the wait time and minimize the power consumption, we designed a novel heating technique by controlling the temperature gradient throughout the length of the column and the unit rapid response time. The heating elements operate in two modes; 1) isothermal mode 2) simultaneous temperature gradients along the column mode. It was explicitly shown that the temperature gradient along the capillary column improves the band spreading and compression, which ultimately reduces band broadening.

On the back side of the column, an axial negative temperature gradient is generated by applying a fixed voltage across the heating element. The temperature is hotter in the center (inlet of the column) than the perimeter (outlet) of the micro-GC using a linear

temperature profile. As the sample passes through different temperature zones, the diffusion rate changes so that the front of the separation peak moves slower relative to the trailing edge of the peak, thereby improving the resolution of the compounds passing through the column. As a result, for a given number of theoretic plates, a shorter column length can be used. Typically, shortening the length of a GC column reduces the analysis time at the expense of resolution; however, thermal refocusing of the eluting band will improve the resolution of the shorter columns. The gradient along the column continuously refocuses the eluting bands, offsetting part of the chromatographic band spreading, and consequently sharpens the peaks as they move down the column. The more volatile compounds move faster at a higher temperature and will focus at a lower temperature; hence, they exit the column quicker than the non-volatile compounds. The band broadening of compounds as they move down the length of the column could be explained by the following equation [52],

$$\sigma = \sqrt{H R(x)} \quad \text{Equation 4-1}$$

where  $\sigma$  is the band standard deviation,  $R(X)$  is the distance as a function of radius, and  $H$  is the column efficiency. The assumption is that the efficiency of a column is independent of time and position along the column for a MEMS GC column mainly due to the short length of the column and a small pressure drop. The variance of a band increases in direct proportion to the distance moved down the column and can be explained with the following equation,

$$\left(\frac{d\sigma^2}{dt}\right) = \frac{H\bar{u}}{(k+1)} \quad \text{Equation 4-2}$$

where  $k$  is the capacity factor and  $u$  is the linear velocity.

$$L = \int_a^b r^2 + \left(\frac{dr}{d\theta}\right)^2 d\theta \quad \text{Equation 4-3}$$

On the top of the column, four resistance heating elements are integrated for side by side comparison of the isothermal analysis with the radial heating analysis.

The main challenge facing the implementation of the axial heating design is the ability to control the temperature profile along the length of the column. To achieve this, three heating element designs were investigated to form a hot spot and were made of a material with high thermal conductivity, so the applied voltage to the heater dissipates in a relatively short time. Even though the most widely used material for micro-fabrication of resistance heaters on silicon is gold, platinum was chosen due to the material's resistivity. Figure 1 shows the heater design, and Table 4-1 summarizes the dimensions of the designed heater.

Table 4-1: The dimensions and resistance of the designed heater

Length(mm)	Heater		Resistance( $\Omega$ )	
	Thickness(nm)	Platinum layer	Gold layer	
4.71	125	7.84	1.52	
11.00	125	18.29	3.54	
17.28	125	28.75	5.55	

In order to investigate the simultaneous temperature gradients induced by the heater on silicon, the heater was designed and simulated using COMSOL Multiphysics®. The 3D simulation was performed by coupling the electric current and heat transfer, and applying the numerical methods described in our previous thermal simulations [53, 54]. For

simplicity, the following assumptions were made: 1) the effect of the insulating SiO<sub>2</sub> layer was insignificant to the overall heat transfer simulation; 2) convection heat transfer from the edges of the silicon to the surroundings were assumed to be small; 3) heat loss due to the traverse of helium gas through the column was compensated by increasing the natural convection coefficient on the back side of the column, and 4) radiation heat losses due to low temperature were small compared to the combined heat loss, and were neglected

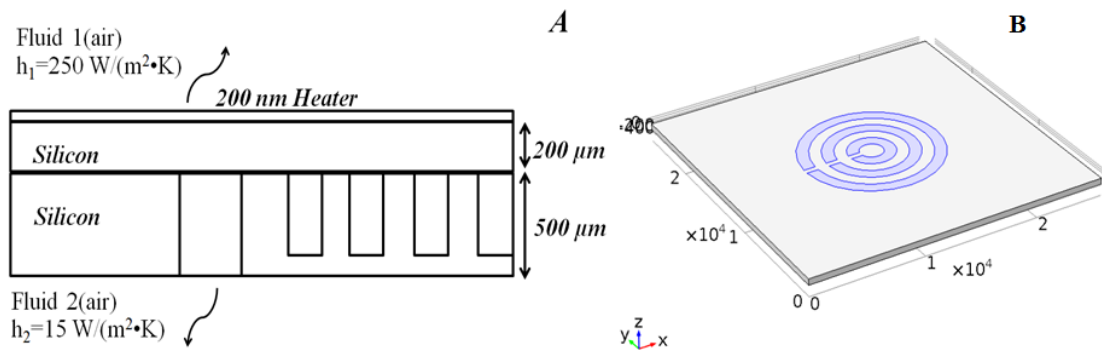


Figure 4-2: A) Side view of GC Colum with heat losses B) layout the heater

The resistance heating layer was the active surface and simulated with *the shell conductive AC/DC layer* which is governed by,

$$\nabla_t \cdot (-d\sigma \nabla_t V) = 0 \quad \text{Equation 4-4}$$

where  $d$  is the thickness of platinum thin film (200 nm),  $\sigma$  is the electrical conductivity (S/m),  $V$  is the electric potential (V), and  $\nabla_t$  denoted the gradient operation in the

tangential directions. The electrical conductivity of the heater was adjusted by a temperature dependent equation,

$$\sigma = \frac{1}{\rho_0[1+\alpha(T-T_0)]} \quad \text{Equation 4-5}$$

where  $\rho_0$  is the resistivity at temperature  $T_0$  ( $\rho_0 = 2.41 \times 10^{-7} \Omega \cdot m$ ),  $\alpha$  is the thermal coefficient of resistance of Platinum ( $\alpha = 2.43 \times 10^{-3} \text{ K}^{-1}$ ). [55]

The heat generated by the Joule heating was coupled with the heat transfer module. The *highly conductive layer* feature of the heat transfer interface was used for joule heating of the thin layer. The power per unit area ( $\text{W/m}^2$ ) generated inside the thin conductive layer is governed by,

$$q_{prod} = dQ_{DC} \quad \text{Equation 4-6}$$

where  $Q_{DC}$  is the power density. At the steady-state, the heat generated by the joule heating is conducted to the silicon column, and some dissipates by forced and natural convection from the top and bottom of the silicon piece to the surrounding air.

## 4.2.2 Current Device Fabrication and Characterization

### 4.2.2.1 Chip Fabrication

The process for fabricating an all-silicon GC column was described in our previous work [48]. To investigate the axial temperature gradient, three heater designs were investigated. To fabricate the integrated heaters and a temperature sensor on the previously micro-

fabricated column, Shipley MICROPOSIT® S1318 photoresist was spin-coated on the column at 1000 RPM for 40 seconds. The column was then soft-baked at 160 °C for 60 seconds and was then exposed using MA-6 mask aligner. The column was then emerged in RA6 developer for 15 seconds and was post-baked at 90 °C for 3 minutes. Denton Explorer was used to deposit 10 nm of Ti as an adhesion layer; subsequently 120 nm of platinum was deposited. The column was then immersed in acetone for several minutes and then was rinsed with DI water.

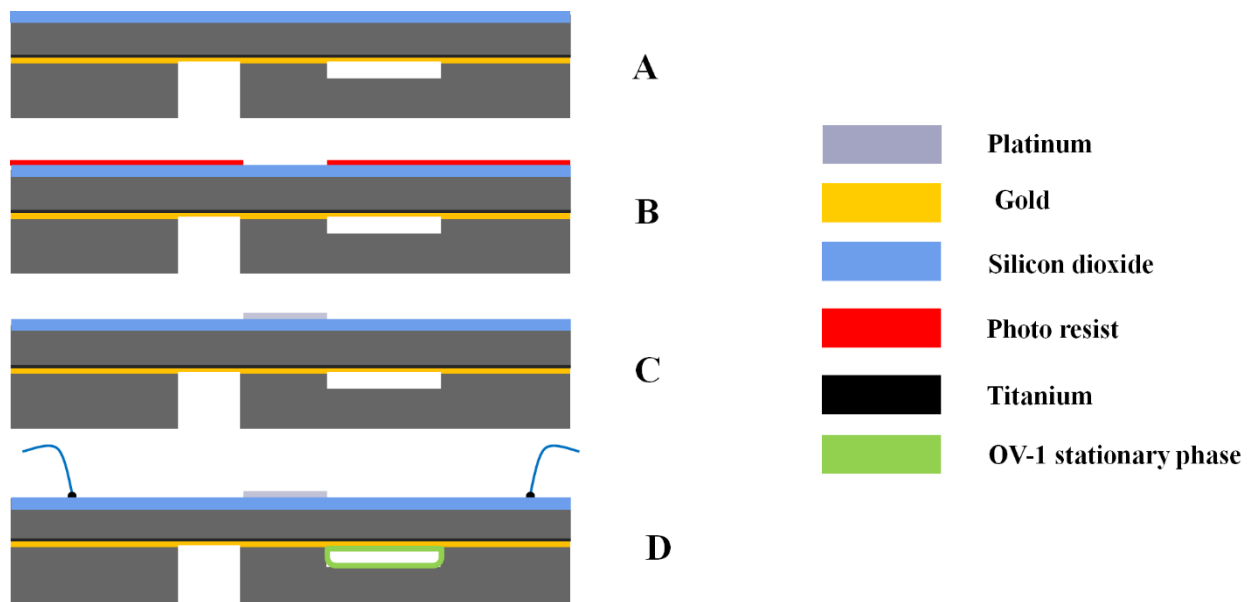


Figure 4-3: A) 200 nm oxide grown thermally B) the top-side is coated with photoresists C) 115 nm of Ti/Pt deposited using E-beam evaporator D) wire bonded the heaters to the package

#### 4.2.2.2 Stage Assembly

A flexible stage was designed to reduce the conductive loss and improve the convective loss by exposing one side to a natural convention and the other side to a forced convection, controlled by an axial fan. Two probes were used to apply a constant power to the heater, while another two probes concurrently measured the temperature of the sensor at different locations on the chip. A 6 digit Agilent meter was employed for measuring the resistance change of the platinum sensors. Figure 3 shows the experimental setup.

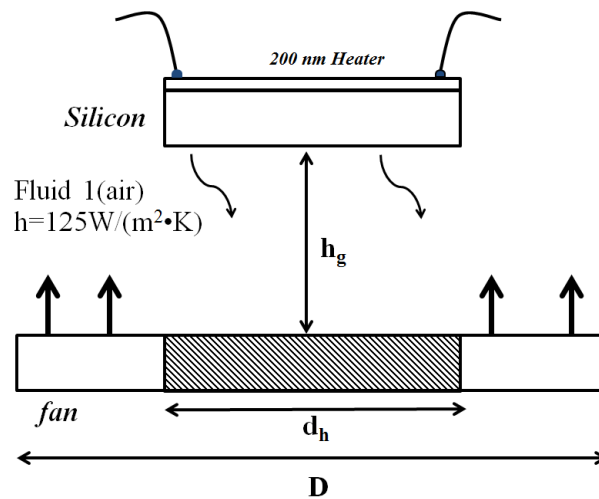


Figure 4-4: Experimental setup

### 4.3 Results and Discussion

#### 4.3.1 Computational Modeling

The simulation method was carried out through a transient response, using the room temperature as the initial condition. Figure 4 presents the structure of the column and the

calculated temperature field when 6 W power was applied and the force convection heat transfer coefficient was at 150 W/m<sup>2</sup>K.

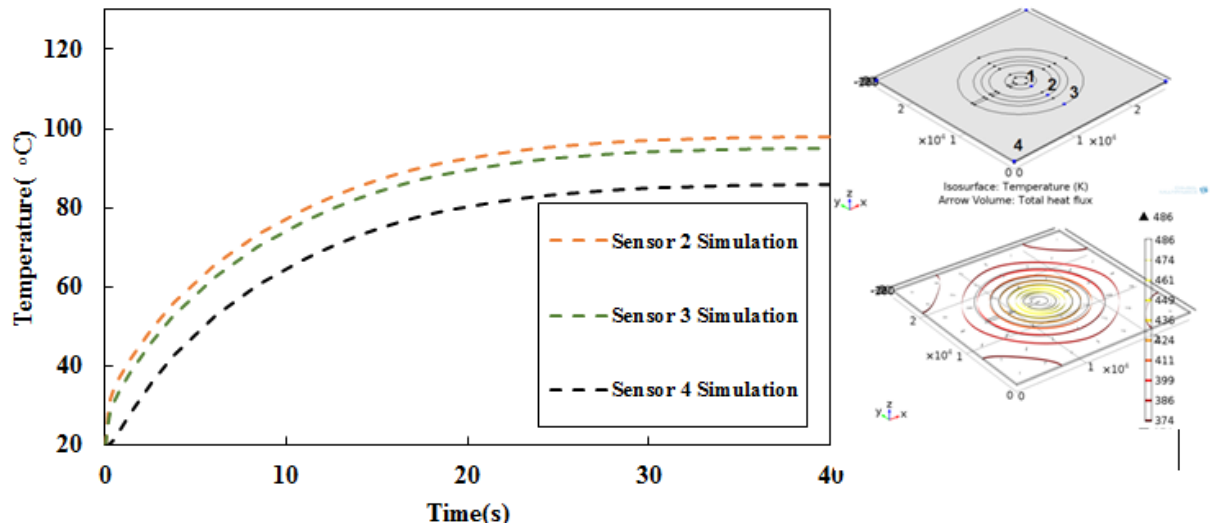


Figure 4-5: Temperature distribution with 6 W of electrical power dissipated in the heating element on the GC silicon column and surrounding air at ambient temperature of 20°C and b) sensors location c) temperature profile

After validation of the model, three heater and temperature sensor designs were investigated. Figure 4-6 shows the three different heater size and temperature sensor designs, and Table 4-2 provides the dimensions and expected resistance value of the heaters for each design. The simulation method depicted in Figure 4-7 shows design b as the best heater design, which provides the largest temperature gradient on the chip.

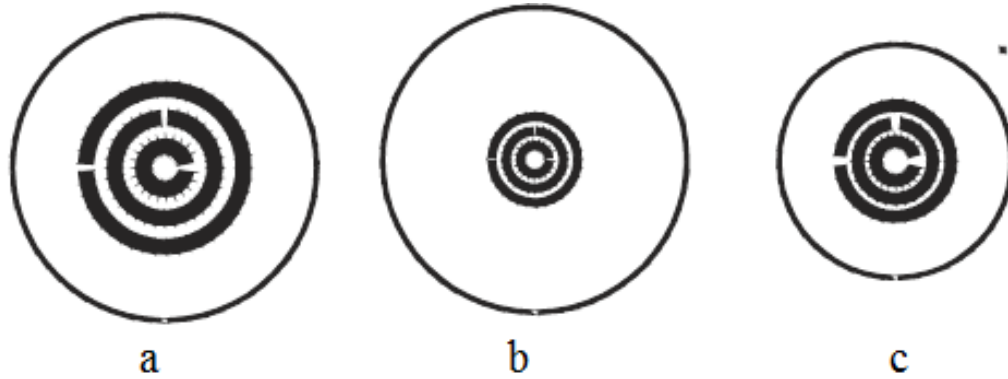


Figure 4-6: Mask designs of the radial heater and the temperature sensor: (a)

Design a (b) Design b (c) Design c

Table 4-2: The dimensions of the three heater designs and the theoretically calculated the platinum resistance.

Design	Radius 1	Radius 2	Length (mm)	Track resistance( $\Omega$ )
Design a	0.001	0.00175	6.28	6.97
	0.00225	0.003	14.14	15.68
	0.0035	0.00425	21.99	24.40
Design b	0.00075	0.00125	4.71	7.84
	0.00175	0.00225	10.99	18.30
	0.00275	0.00325	17.28	28.75
Design c	0.001	0.002	6.28	5.22
	0.003	0.004	18.85	15.68
	0.005	0.006	31.42	26.14

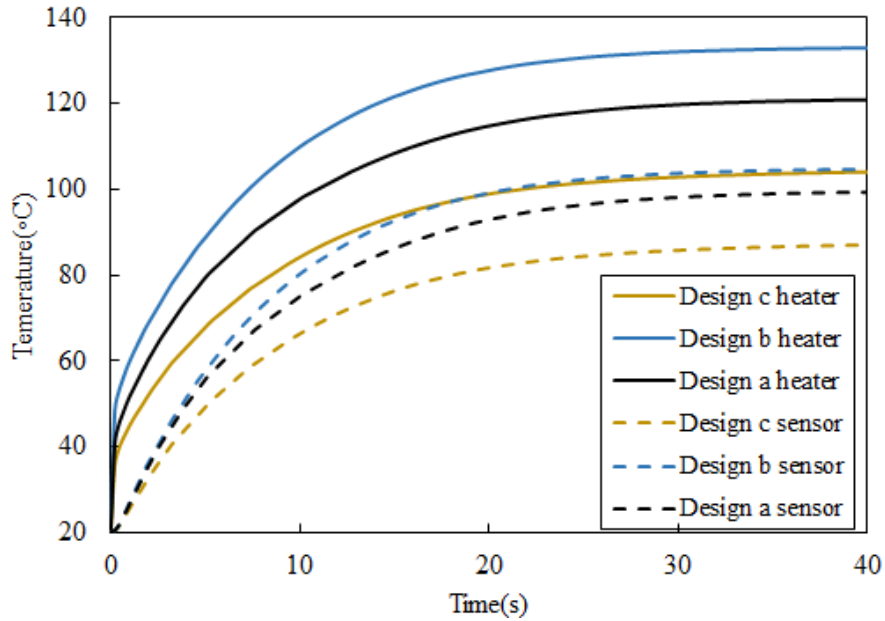


Figure 4-7: Simulated transient response of temperature over time after applying 6W of electrical dissipation to the heater, for the three designs.

### 4.3.2 Heater characterization

To validate the simulation data, the electrical properties of the thin film of platinum were characterized. The experiment was carried out by placing the column on a temperature controlled probing station, the change in resistance of the sensor was measured using a digital multimeter and a thermocouple (with accuracy of 0.1 °C) was used to measure the temperature.

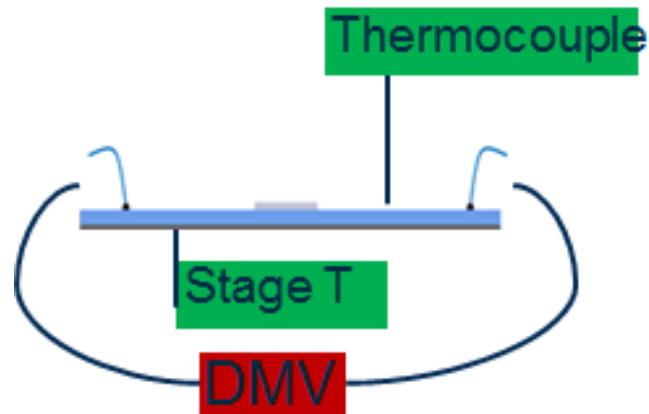


Figure 4-8: Experimental setup for TCR measurement

The measurement was performed in a temperature range between 30 to 80° C. The TCR and the base line resistance of the thin film of platinum were calculated by plotting the measured resistance of the sensor against the temperature of the thermocouple and fitting it into the following equation.

$$R = R_0\alpha(T - T_0) + R_0 \quad \text{Equation 4-7}$$

where  $R_0$  is the base resistance at the base temperature,  $\alpha$  was calculated by dividing the slope of the linear fit by the  $R_0$ , which is the linear line interception with the y axis, to be  $\alpha = 2.54 \times 10^{-3}$  and  $R = 18.16 \Omega$ . The TCR values of the thin film platinum were 65% smaller than bulk platinum due to impurities in the platinum and also the surface roughness quality of the platinum film. [55]

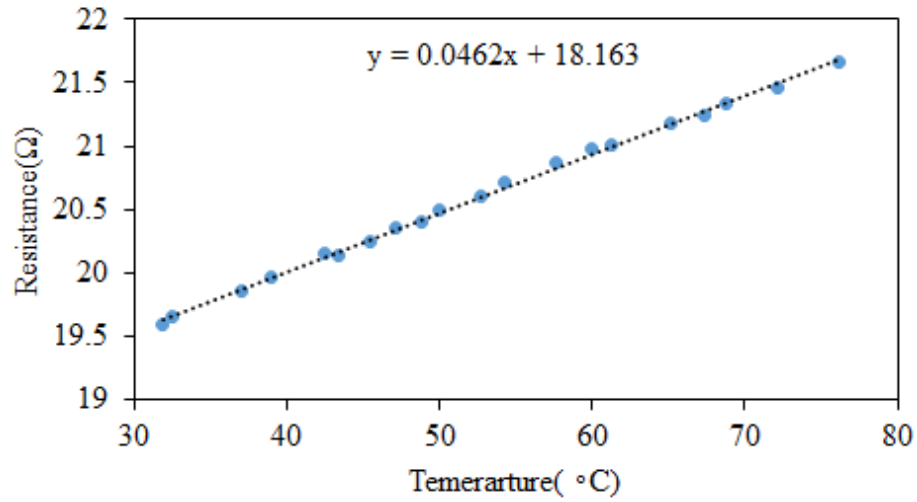


Figure 4-9: Temperature calibration data for the heater, where each data point was obtained by subjecting the column to a uniformly heated glass plate surface.

### 4.3.3 Coefficient of Convection Characterization

The convective heat transfer coefficient is another critical factor affecting the temperature gradient generated on the column. A higher convective coefficient provides a better temperature gradient at the cost of increasing the power consumption. To obtain the coefficient of convective heat transfer, the model of the heating method was simulated for different heat transfer coefficients of convection and compared to the experimental data collected while the fan (50X15 mm 12V DC model number AFB0512HHB) was operating at 12 V.

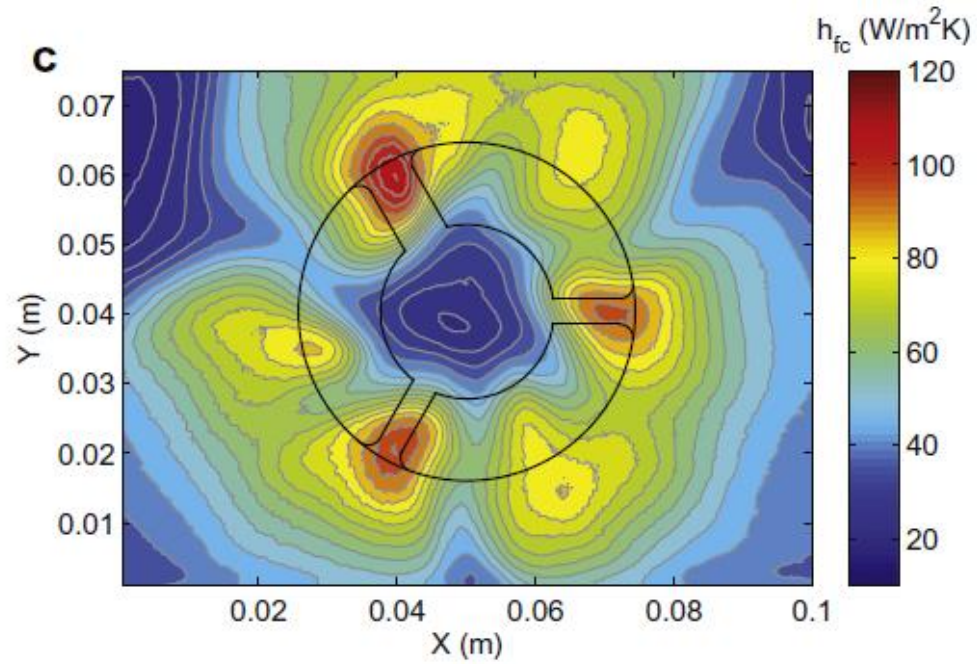


Figure 4-10: Forced convection heat transfer coefficient for 4000 rpm and a fan to plate distance of 15 mm[56]

The convective heat transfer of the fan was measured to be  $125 \text{ W/m}^2$  based on the distance from the column, which agrees with previously reported data [56].

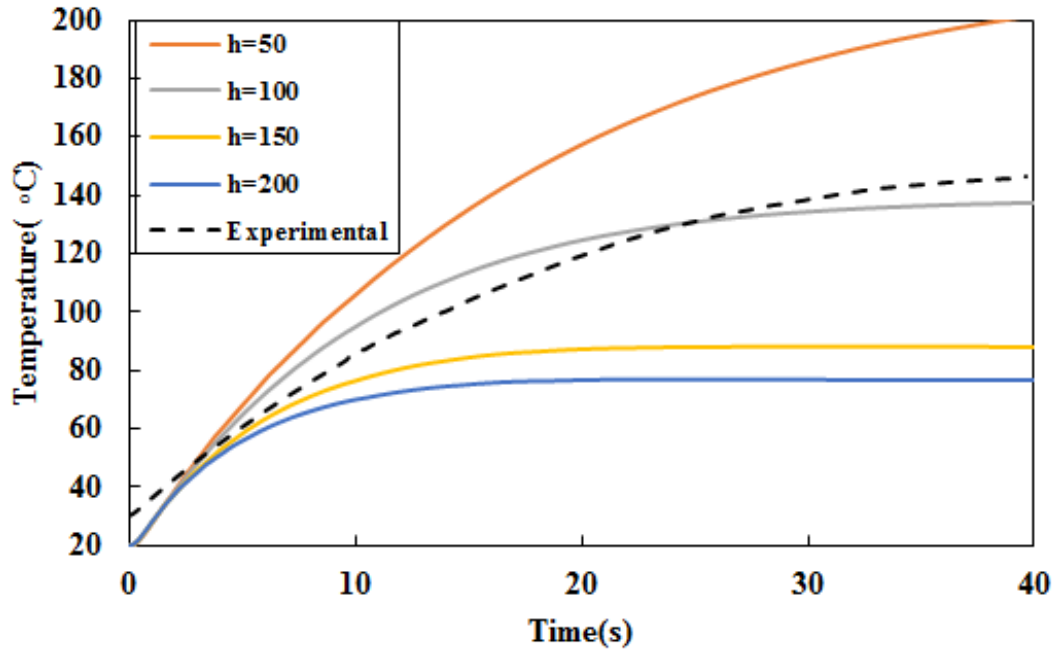


Figure 4-11: Plot of simulated average temperature transient response of the resistor film with 2W electrical power applied to the heater compared to experimentally measured temperature on the micro-GC column with convection heat transfer coefficient in air as a parameter.

#### 4.3.4 Experimental Setup

To test the effectiveness of the heater, heat transfer performance on the chip was quantified by measuring the resistance change of the platinum sensors at different locations and using temperature profile infrared thermography. The schematic of the experimental apparatus and the location of the fan relative to the column is presented in Figure 4-12 where the 700  $\mu\text{m}$  thick column is heated by resistive heating and cooled by an axial flow fan. A fixed current of 0.6 A is applied to the center of the platinum heater, resulting in heating of the column by joule resistive heating. A 12 V DC fan was employed by placing it at 20 mm

distance from the chip to generate sufficient convective heat transfer in order to cool the column. The thermal image of the GC column was captured by using a fluke TI 27 infrared digital camera with an InSb detector. Furthermore, the temperature of the column at different locations was measured using temperature sensors embedded on the column. A calibration of the temperature sensors were conducted to ensure an accurate temperature measurement

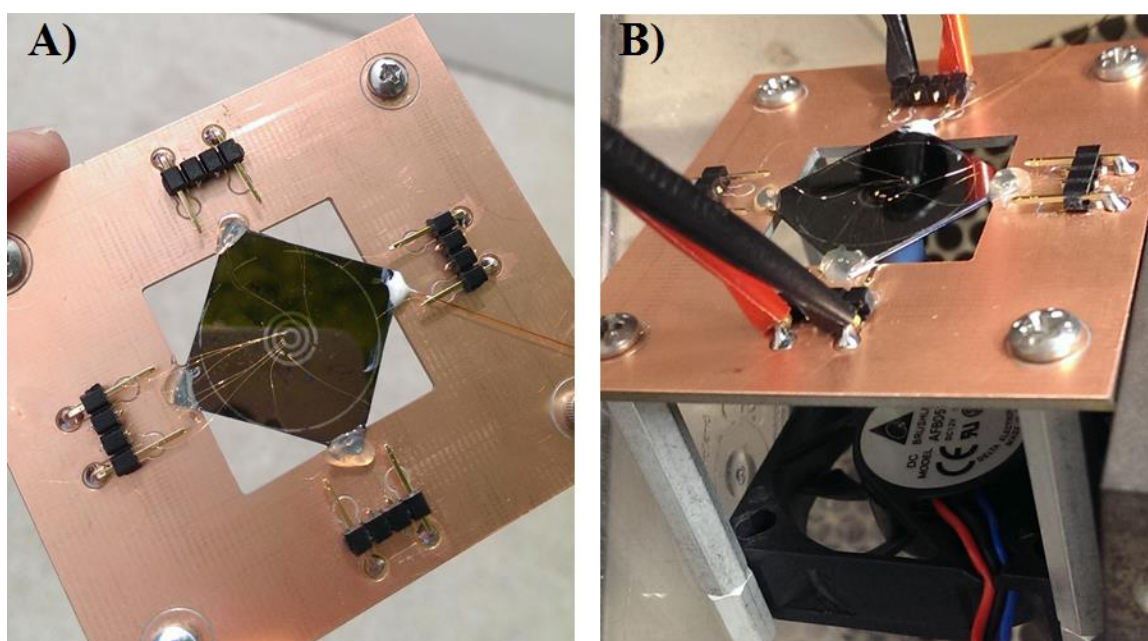


Figure 4-12: 2-D Experimental Setup A) Top View B) Side view with the location of the fan from the chip

Figure 9 shows the transient response of the heater in response to an applied current of 0.6 A, measuring the temperature at three different locations on the column. The total power applied to the chip was calculated to be 10 W, which is sufficient to generate a temperature gradient of 40 °C in less than 40 seconds.

A simulation of the heater temperature as a function of time for the heater was performed, and the results are compared with the experimental data collected for the 26 by 26 mm column. The simulation data was modified based on the TCR and thermal resistivity of the platinum. The simulation response shows a good agreement between the measured temperatures and the simulation data.

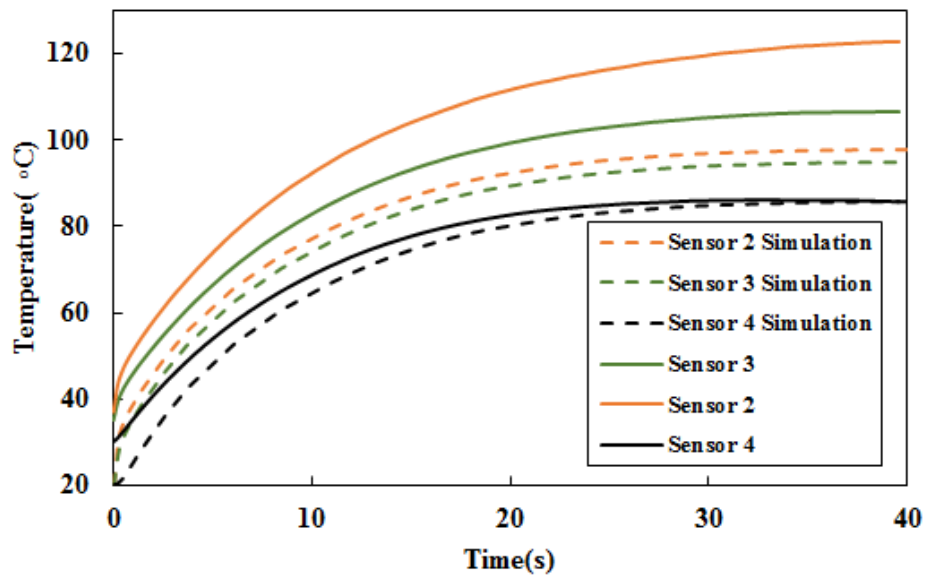


Figure 4-13: Transient response of heater design b to a 0.5 A constant current.

There is a small discrepancy between the experimental and simulation data as a result of the impairing the air flow of the axial flow fan, which results in variation in local heat transfer coefficient distributions across the column. The fan to plate distance was fixed at 20 mm [56], and the fan was blowing air at the surface of the column. This applied power results in joule heating of the silicon, and temperature was measured at 3 different locations on the chip.

Figure 4-14 shows the transient response of the GC column with an embedded heater at two different power levels ( $I^2R_0$ ), where  $I$  is the high current value and  $R_0$  is the base resistance. As expected, the transient heating time constant increases with power and provides a larger temperature gradient from the center to the edge of the column. We expect significant improvement in column performance when the gradient produces a temperature different of more than 40 degrees.

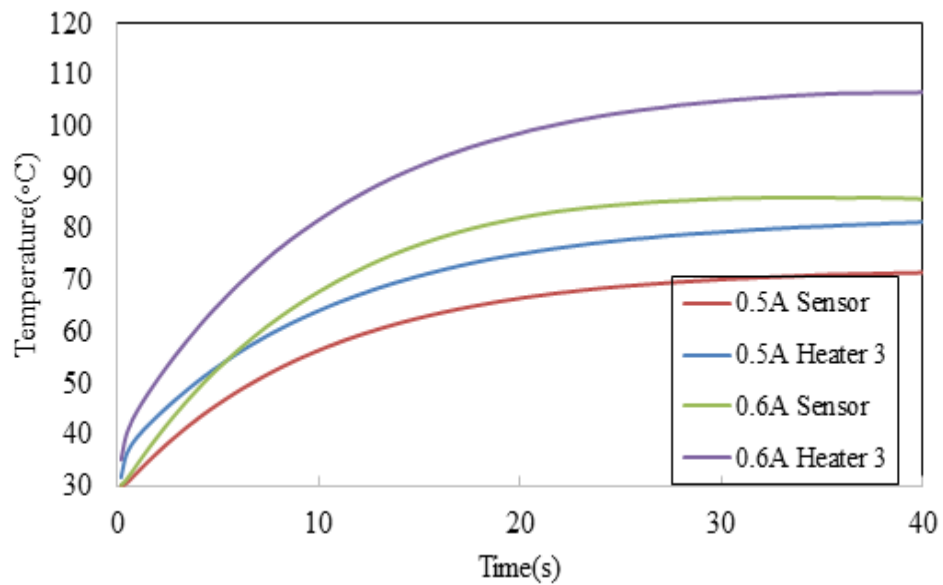


Figure 4-14: Transient response of the heater at two different power levels

Temperature distribution of the silicon column was further measured using an infrared camera, and the relationship between heat fluxes was measured by force convection. Silicon was assumed diffuse and gray with an emissivity of 0.65 for temperature estimates.

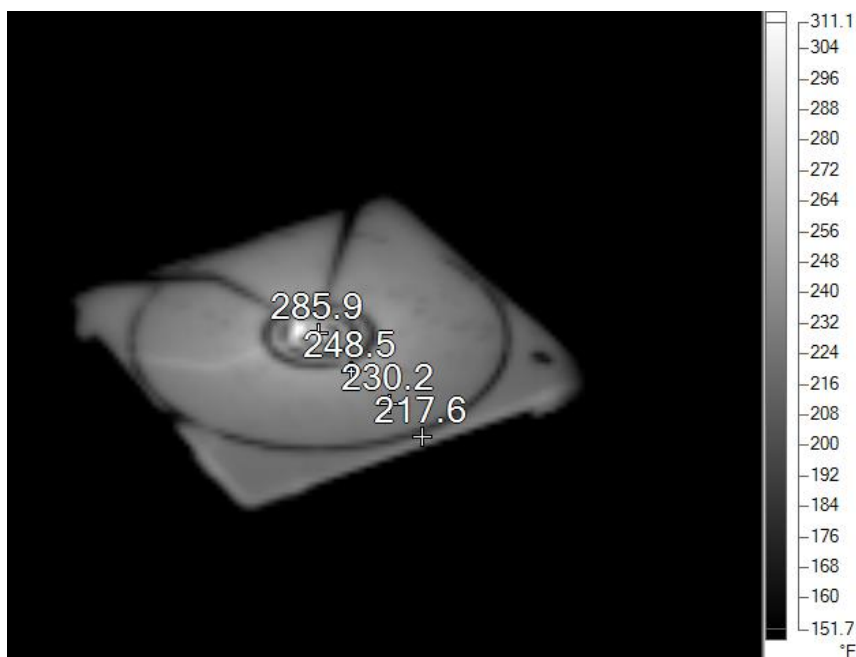


Figure 4-15: Temperature distribution in Kelvin, estimated from IR thermal imaging with an applied voltage of 13 volts applied to heater b with forced convection present

#### 4.4 Column Performance Evaluation for Focusing of Wide Injections

To evaluate the focusing of the peaks band, the 3-meter GC column was operated in isothermal, temperature gradient (TG), and temperature gradient programmed mode. A simple mixture of hydrocarbons (hexane, octane, and decane) was prepared to test the device over an appreciable range of volatilities.

The column was connected to an HP 6890 Fast-FID, and the chromatograms of the 3 compounds were obtained by injecting 1  $\mu\text{l}$  of the mixture sample (split ratio of 400:1, Pressure 16 psi, and 60  $^{\circ}\text{C}$  center temperature.

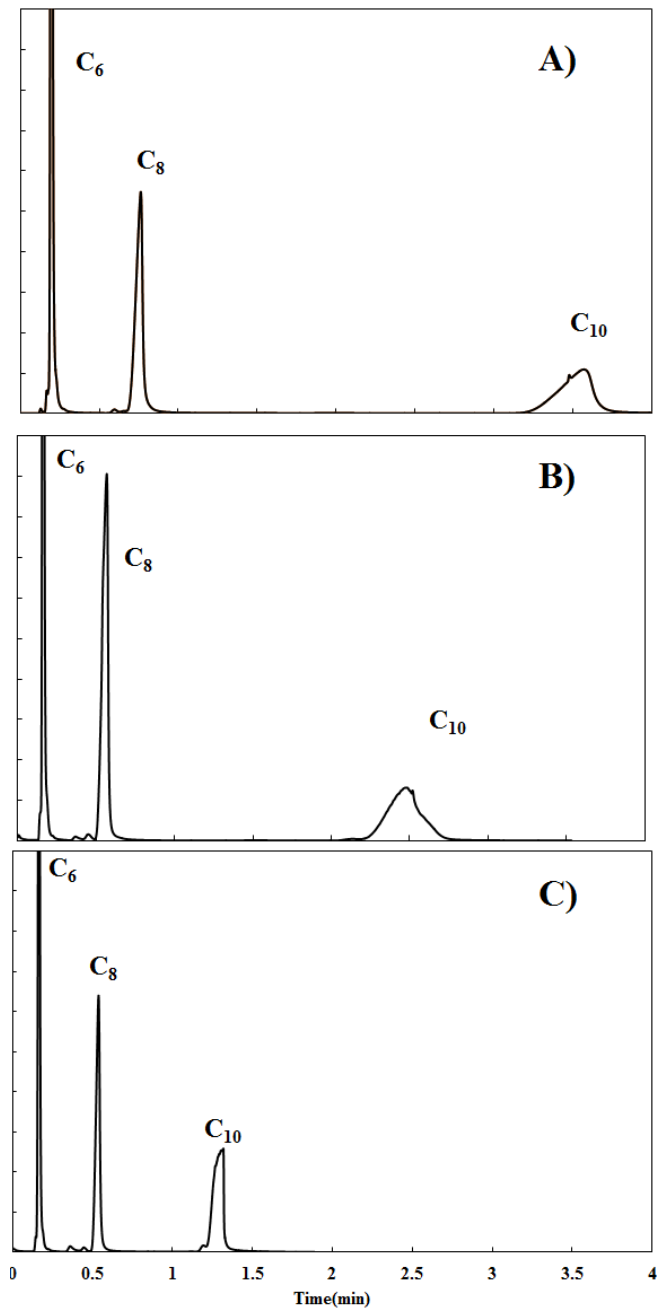


Figure 4-16: Chromatograph achieved using the 3 meter column at pressure 16 psi and inlet temperature of 240 °C with OV-1 stationary phase using A) 60°C isothermal temperature B) temperature gradient with center temperature of 60 °C C) Temperature gradient programmed at 250 °C/min from 60°C to 110 °C.

Table 4-3: Peak focusing calculated for Temperature gradient GC (TGGC) and Temperature programmed gradient GC(TPGGC)

peak	TGGC	TPGGC 150 °C/min	TPGGC 250 °C/min
C <sub>6</sub>	11.19%	21.59%	19.15%
C <sub>8</sub>	20.60%	43.03%	67.94%
C <sub>10</sub>	12.41%	60.13%	69.03%

Figure 4-16A displays the chromatogram obtained for the isothermal run. The peak widths and shapes of hexane (C<sub>6</sub>) and octane (C<sub>8</sub>) are acceptable for the length of the chromatographic column, however the peak shape and peak asymmetry of decane (C<sub>10</sub>) are in clear need of improvement. These runs were performed in triplicate, and the results are consistent within acceptable ranges of statistical variations typically observed in conventional chromatography (5% coefficient of variation or less for retention times, peak area, and peak asymmetry).

Figure 4-16B shows a chromatogram obtained for a run in which the device was operated isothermally at 60°C in the thermal gradient mode. The application of the axial thermal gradient reduces the residence time of the analytes through the system, and results in a reduction in the retention times for all 3 compounds. But more importantly, the peak widths of the analytes are reduced as well, due to the reduction of the peak broadening that typically occurs as the compounds are travelling through the column. Table 4-3 shows that the peak focusing is significant (between 10-20% for the compounds in the test sample) and compound specific. It is also observed that for the decane peak the severe tailing that was occurring at isothermal conditions (Figure 4-16A) has been corrected, and the peak asymmetry has improved substantially. These series of runs were also run in triplicate, and

chromatograms were consistent within acceptable statistical ranges. The chromatogram shown in Figure 4-16B thus demonstrates the utility of the negative thermal gradient in the improvement of chromatographic resolution.

Figure 4-16C shows a chromatogram obtained for a run in which the device was operated in multidimensional temperature programming mode, meaning that there is a temperature program in time (ranging between 60°C and 110°C at 4.2°C/second) that is superimposed on the temperature program in distance (the negative thermal gradient that was applied in Figure 4-16B). The combined effect of these two temperature program regimes is a further reduction in retention times that is accompanied with additional peak focusing. Once again, these improvements are compound specific, but significant enhancement is observed for all compounds in the mixture. For a late eluting compound like decane, the impact of both temperature programs is particularly salient. The fast temperature program in time is responsible for the sharp reduction in retention time, and the temperature programming in distance is responsible for the reduction in the peak width, which enhances the peak height because the peak area is unchanged. This combined effect is quite advantageous for separations on columns whose length is markedly shorter than those used in conventional chromatography, because it provides a tool to enhance the chromatographic resolution. Overall, the decane peak's retention time has been reduced by over a factor of 2, and its peak height has been enhanced by over a factor of 2 between the conditions used in Figure 4-16A and Figure 4-16C. Similar optimization of bi-dimensional temperature programs were tested for compound mixtures containing a wider variety of chemical functional groups (such as alcohols, ketones, and fatty acid methyl esters), and similar observations were obtained [57, 58].

The combined effect of these two temperature program regimes is further investigated for different ramping rates and shown in Figure 4-17. As was expected, the separation performed at higher ramp rate results in a further improvement in retention times that is accompanied with additional peak focusing.

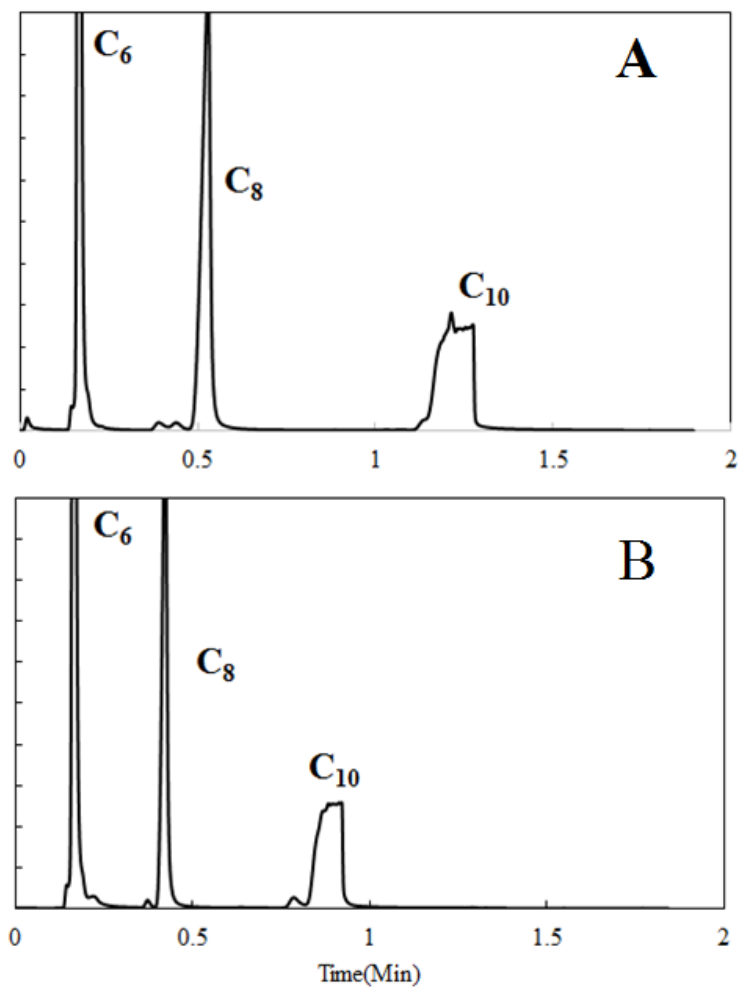


Figure 4-17: Separation of a hydrocarbon mixture A) Temperature gradient programmed ramped at 150°C/min B) Temperature gradient programmed ramped at 250°C/min

## 4.5 Conclusions/Outlook

In this work, we investigated the effects of temperature gradients as a function of time and position,  $T(t,x)$ , along the length of a micro-GC column. Three different heater designs were evaluated through numerical modeling using COMSOL Multiphysics. A detailed geometry of the GC column with thin film resistive heaters was used as a basis for the simulation, to investigate the heating and cooling rate, power consumption, and temperature distribution of the new axial heating method for the all silicon micro-GC column. The best geometry with the maximum temperature gradient was selected for microfabrication and evaluated experimentally. The temperature distribution was evaluated using several embedded temperature sensors and IR imaging. The effectiveness of the heater was investigated by separating a mixture of compounds using a 3-meter microGC column. The results with a 30°C gradient from the center to the edge of the column demonstrate enhanced separations for a test mixture of 3 hydrocarbons that span a range of boiling points of over 100°C. The dual temperature programming (in time and space) produced improvements in peak focusing that result in significant increases in peak height. This novel temperature programming method demonstrates that the performance of micro-GC columns can be improved using thermal programming techniques to increase analytical performance.

## **Chapter 5**

### **THERMAL CONDUCTIVITY DETECTOR (TCD)**

In this chapter, we describe the design and integration of a low power, ultra-sensitive thermal conductivity sensor for fast and more accurate measurement of the VOC gases separated with the previously micro-fabricated MEMS GC column. The TCD sensor was optimized for different flow rates, and the dead volume was reduced to avoid sample dilution. After separating the compounds using the GC column, it is vital to have a fast detector that is capable of detecting all the separated compounds.

#### **5.1 Introduction**

The thermal conductivity sensor is used for monitoring the low ppm levels of the composition of gases in the environment. Compared to the conventional GC chromatograph, MEMS GC chromatograph bands eluting are narrower; therefore, they require a significantly faster detector to capture the signal. Compared to a GC-FID and a mass spectroscopy (MS) system, TCD sensors are easy to micro-fabricate, use low power, and carry low cost; however, the tradeoffs are that they perform with poor detection limits, need a carrier gas, and have constraints on factors such as temperature and humidity.

The main driving principle of a thermal conductivity sensor is Joule heating of a conductive filament, then measuring its resistance changes and correlating these measurements with the thermal conductivity of the gases passing over it. The simplest TCD sensor is a heated platinum wire, which acts as a heater and a detector simultaneously and measures the

thermal conductivity of the surrounding gases when it is heated. The more advanced TCD sensors are micro-plates and pellistors. The disadvantages of these sensors are their large surface area and their big thermal mass, hence the response time and the power consumption suffer significantly. The recent developments in MEMS technology enable the micro-fabrication of a highly sensitive, low power, and low cost TCD sensor.

A number of research papers have been published on miniaturization of thermal conductivity sensors and their application in a MEMS GC column; however, these reported miniaturized sensors have a large dead volume, and their signal to noise ratios are significantly large [59-66]. Khanna et al. [63] have designed an electro-thermal polysilicon micro-heater for use in gas sensing; they showed that by applying 4 V a mean temperature of 706° C is possible, and the heat is transferred from the sensor to the surrounding air. However, the total power requirement to operate the microplate is around 50 mW, and the response time is in the order of 10 ms. Cruz et al, [62] demonstrated a microfabrication of micro-TCD with a four-filament Wheatstone bridge circuit to compensate for the variance in the flow rate. The resistors are suspended by a silicon nitrate membrane, and their detection limit and power consumptions are 1 ppm and 1 W respectively.

Here we present a low power, ultra-sensitive sensor that is faster and more sensitive than the previously reported TCDs. This was achieved by reducing the dead volume and reducing the sensor's dimensions. Figure 5-1 shows a summary of the process used to fabricate TCDs in the Georgia Tech cleanroom.

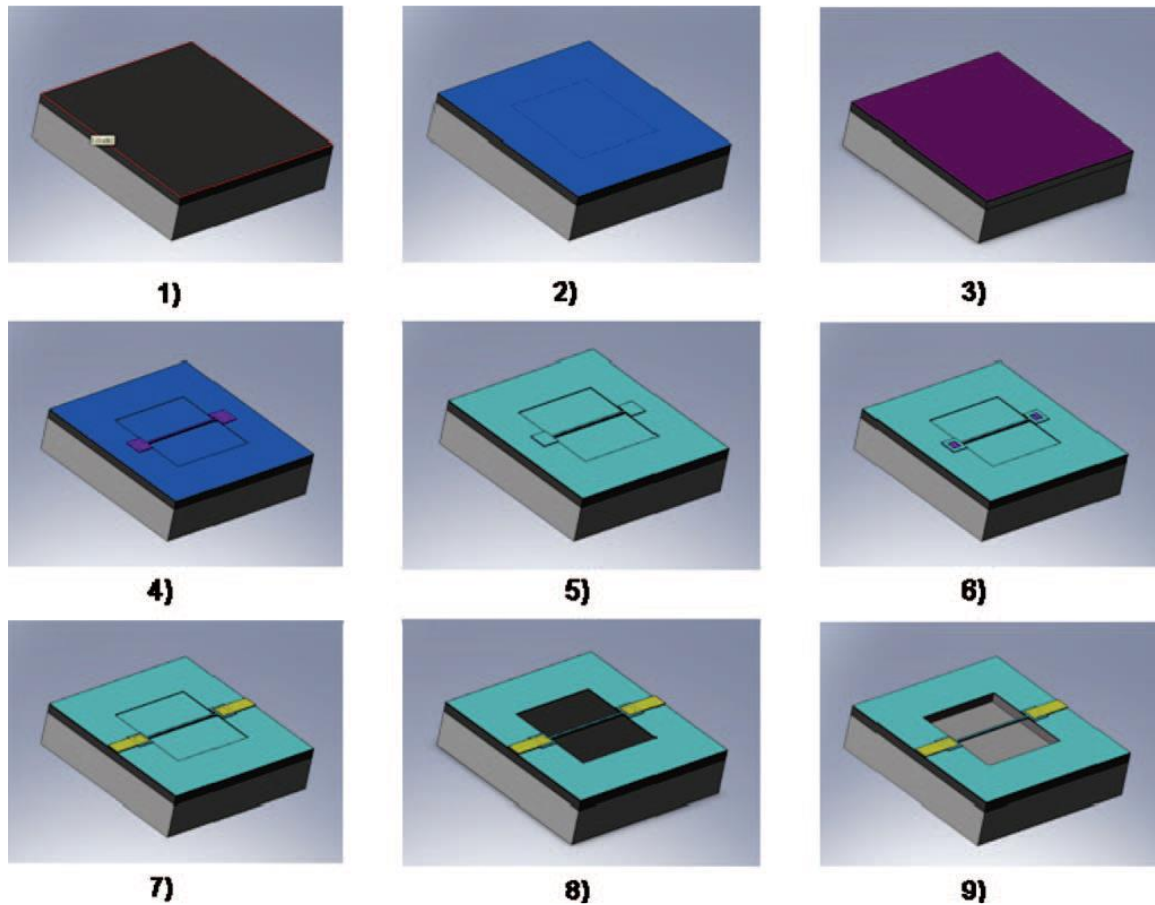


Figure 5-1: Summary of ultra-low power TCD fabrication process [53]

Previous work with a  $1\mu\text{m} \times 100\mu\text{m}$  TCD sensor in a no flow condition have shown promising results in terms of sensitivity and power consumption [53, 67]. Therefore in this work we focus on improving the packaging feature of the TCD sensor, refining the TCD sensor response, evaluating the sensor's responses in different helium flow rates, and integrating the sensor with the previously micro-fabricated MEMS-GC.

As described in Figure 5-2, the TCD micro-bridge is a doped polysilicon, and its resistance correlates to the average temperature of the bridge. A low-stress 200 nm silicon

nitride membrane is thermally grown as a support structure, and the bridge rests on it. The SEM image Figure 5-2 shows the thickness and the structure of the TCD.

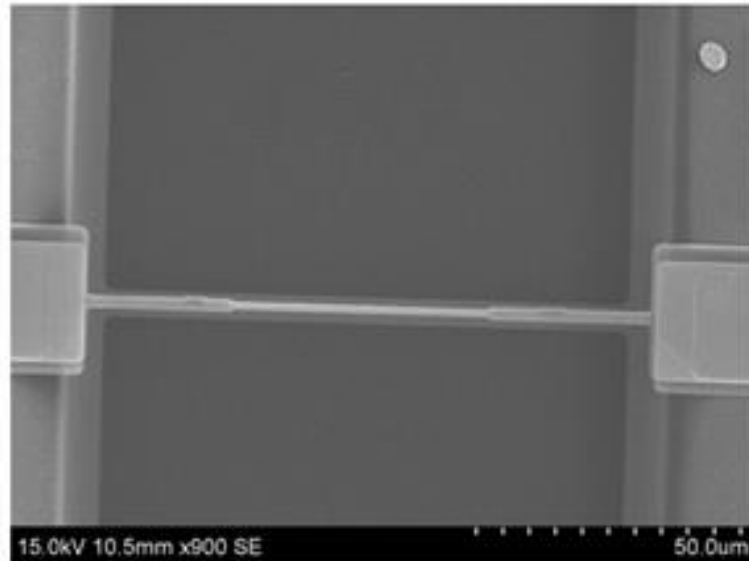


Figure 5-2: Scanning electron microscope image of the fabricated micro sensor; a 100:1 bridge with 50:1  $\mu\text{m}$  narrow center region

The alteration in the thickness, at the center of the bridge, increases the resistance of the bridge. Therefore, for the same applied current, more heat is generated and the bridge becomes hotter in the center, farther from solid anchors. Electrical characterization of the sensor was carried out to determine base resistance,  $\rho_0$ , and Temperature Coefficient of Resistance,  $\alpha$ , for modeling and experiments. The sensor was placed in a temperature controlled oven and was subjected to a series of uniform steady temperatures, up to 70°C. For the microbridge in this study, a TCR of  $\alpha = 0.0013 \text{ 1/}^\circ\text{C}$  and a base resistance of  $\rho_0 = 3084 \text{ } \Omega$  at 23 C were measured.

## 5.2 Experimental Implementation of Micro-TCD in GC system

In order to investigate the performance of the TCD with the changing flow rates and pressure levels, a TCD was packaged and connected to a standard GC system.

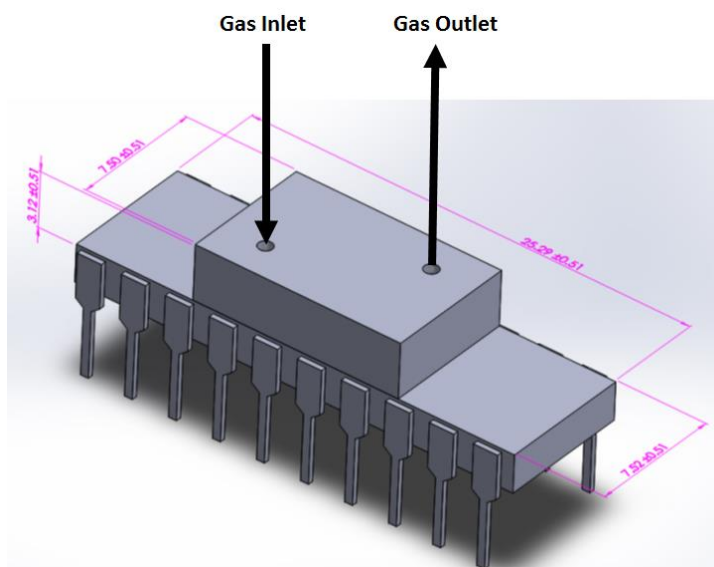


Figure 5-3: sensor packaging with flow ports and electrical connections

The gas inlet was connected to the inlet of the package and was sealed using an UV cured epoxy.

Constant current and constant voltage are the most common methods for operating a TCD. In the constant voltage operation mode, the micro bridge temperature rises as an analyte with lower thermal conductivity crosses the bridge. On the other hand, constant current operation mode generates a feedback loop by adjusting the current applied to the bridge. To use the TCD sensor in our setup, a Semi Wheatstone bridge circuit interface was designed to measure the voltage change that corresponds to the thermal conductivity of the gas passing over the bridge. The circuit is composed of

resistance of the sensor ( $R_s$ ), reference sensor ( $R_R$ ), corresponding resistance ( $R$ ), and an op-amp (OPA1324). In order to measure the change in resistance of the TCD, the value of  $R_R$  and  $R$  were fixed ( $R_R=2858 \Omega$  and  $R=300 \Omega$ ), and the output voltage of the op-amp was measured using the following equation,

$$V_0 = \frac{V_B(R_R - R_S)}{(R + R_R)} \quad \text{Equation 5-1}$$

An output pulse of 2.5 V with 50 Hz frequency and 20% duty cycle was used to prevent the bridge from overheating.

The experimental setup shown in Figure 5-4 was developed to measure the TCD response. The TCD response, which is in microseconds, is much faster than conventional TCDs commonly used in the commercial fast GC systems. To investigate the stability of the previously micro-fabricated MEMS sensors in helium gas flow, a single MEMS TCD sensor was connected to the outlet of the MEMS GC. The sensor was then tested in the following conditions: Helium flow rate was set to 1 mL/min, temperature was at isothermal condition at 80 °C, and power was set to 4.28 mW. The final device is shown in Figure 5-5B. Initially, the TCD sensor was calibrated at no flow condition. The dead volume of the TCD sensor was reduced to 150  $\mu$ l by filling the dead volume with cement while an Aluminum lid was used to cover the sensor.

The sensor was connected to a 3 meter long GC MEMS, while helium was continuously flowing over the sensor. A constant voltage of 3.83 V was applied to the circuit's input, corresponding to a sensor current of 1.2 mA, during which the output of the sensor was recorded using a data logging DMV.

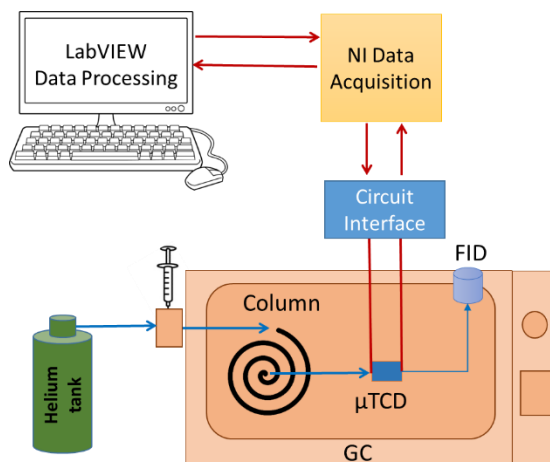


Figure 5-4: Schematic of the experimental setup for  $\mu$ TCD testing in GC system

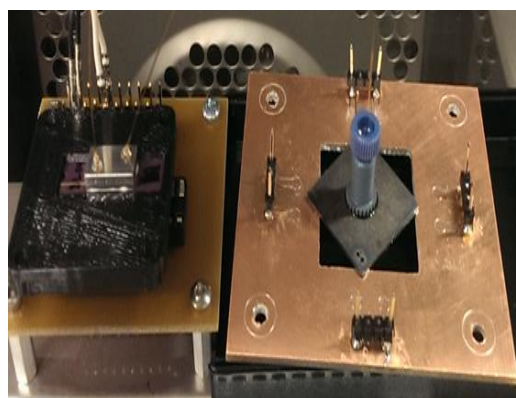
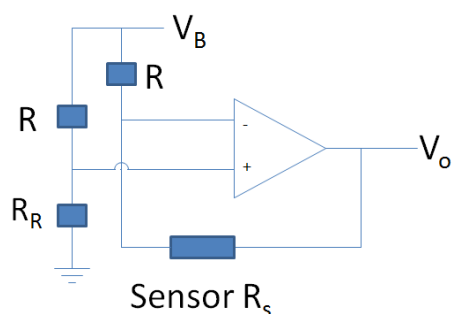


Figure 5-5 A) Circuit interface B) experimental setup

#### 5.2.1.1 Relation between TCD resistance change and flow rate

The inlet of the TCD was connected to a 2.4 meter HP-1 GC-column with inner diameter of 0.32 mm and non-polar stationary phase of 250 nm thickness. The outlet of the TCD was vented to the atmosphere to reduce the effect of backup pressure. The TCD was attached to a 20 pin package and sealed using a 3.1X4.5 aluminum cap. The total dead

volume of the TCD was calculated to be around 150  $\mu$ l. Testing was performed by connecting the inlet of the TCD to the GC system and changing the pressure over a wide operating range.

Table 5-1: Base resistance of the TCD at different pressure levels

	PSI	Delta R	Base Resistance
He	10	138.5	2456.4
	5	138	2456.4
	2.5	137.9	2456.5
Air	1	137.9	2456.6
	0	516.8	2459.1

As shown in Table 5-1, the resistance change of the detector remains almost constant while the GC inlet pressure levels and flow rates vary. This result coincides with our numerical simulation result, which anticipated insensitivity to flow rate at typical flow speeds used in a GC system. This result suggests that in this system, the thermal conductivities of two fluids, helium and air, are independent of flow rate.

#### 5.2.1.2 Relation between pressure and TCD response

One of the limitations of the diffusion based TCD sensors is their limit of detection due to flow and mass transfer phenomena in the channels. These phenomena cause the concentration of compounds to be lower at the edge of the channel than the center; therefore, higher flow rates are required to obtain a fraction of the concentration.

To evaluate the TCD response in different flow rates, the TCD sensor was connected to the column, and a fixed concentration of hexane was injected into the system at different

pressure levels. Figure 5-6 shows the response of the TCD for 0.2  $\mu\text{L}$  of hexane at 4 different pressure levels.

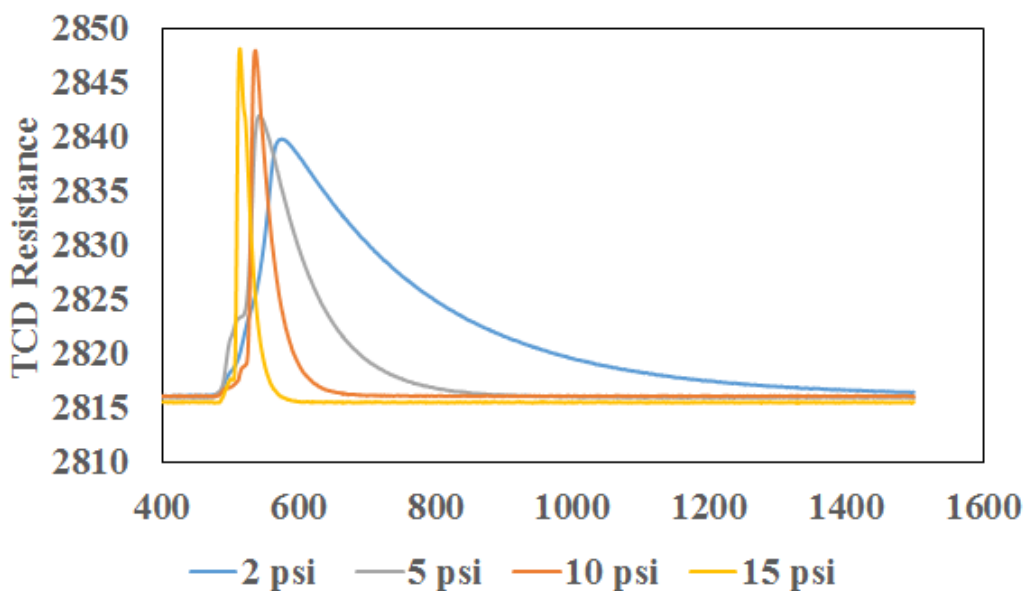


Figure 5-6: TCD response for different pressure levels.

### 5.2.1.3 TCD Level of Detection

To study the relation between the magnitude of the TCD signal and the concentration of a compound, known volumes of hexane samples were injected into the system, and the TCD response was recorded and presented in Figure 5-7. The area under the response

curve is the total concentration of the compound detected by the TCD sensor, and was calculated by integration of the response curve over time.

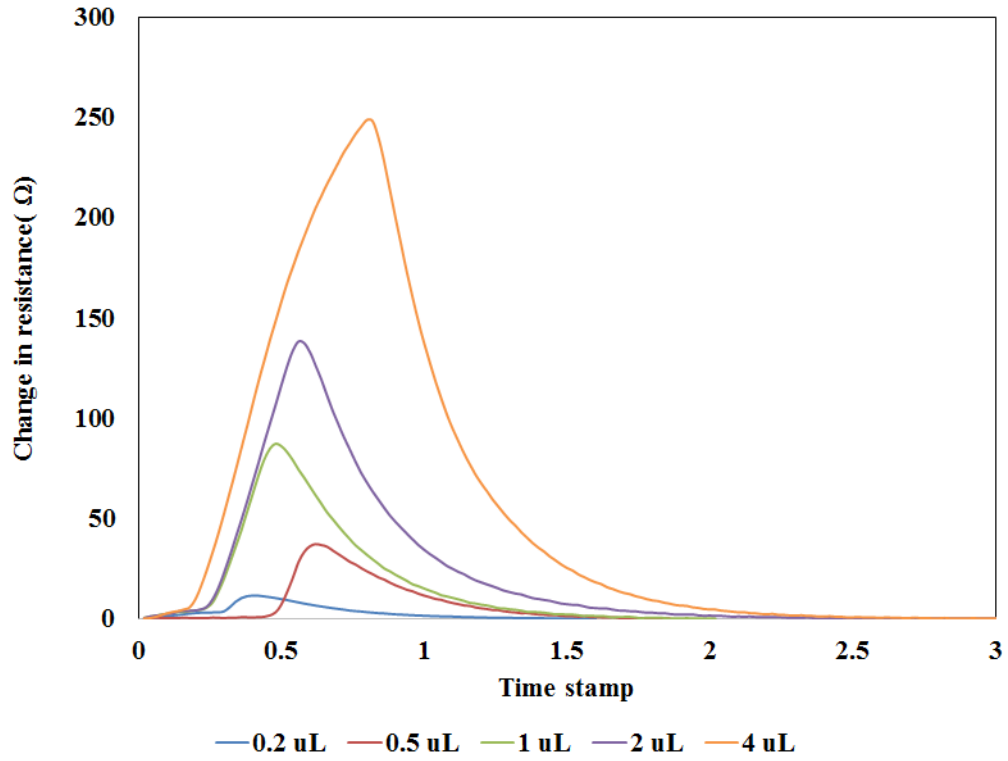


Figure 5-7: Response of the MEMS TCD for different sample concentrations

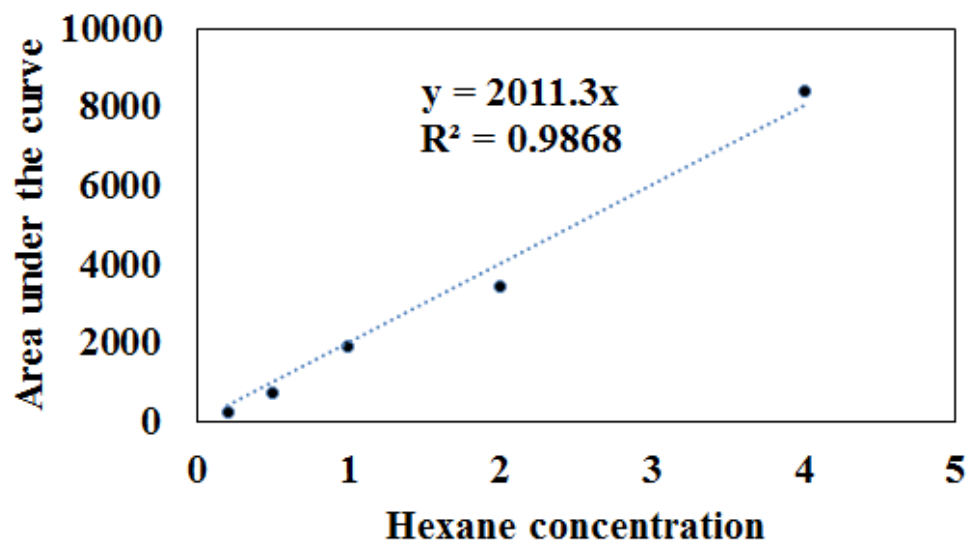


Figure 5-8: the concentration hexane vs. the area under the curve

where the x axis is the concentration level of Hexane( $\mu\text{L}$ ) and the y axis is the resistance ( $\Omega$ ) . Overall there is an approximate linear correlation between the amount of the compounds injected and the area under the curve; however, the small variance in the linear fit is due to inconsistency in manual injection.

### 5.2.2 TCD Response Compared to a Commercial FID Detector

Next, the performance and resolution of the TCD system were compared to those of a commercially available FID detector. The GC system and TCD Sensor were operated isothermally at  $80^\circ\text{C}$ , 1:500 split ratio, and the inlet pressure was set to 10 psi.  $0.2 \mu\text{l}$  of a mixture of six compounds with different kovats indices was injected to the GC system, and the results are shown in Figure 5-9. Intentionally, two out of the six compounds were chosen to have a comparable Kovat index to illustrate the resolution of the TCD.

Table 5-2: List of compounds in the mixture

	Compound	Kovats
1	C9	900
2	C10	1000
3	1-octanol	1058
4	linalool	1087
5	C11	1100
6	C12	1200

The figure below shows the separation of the six compounds listed in Table 5-2 using a standard FID detector and using the MEMS TCD.

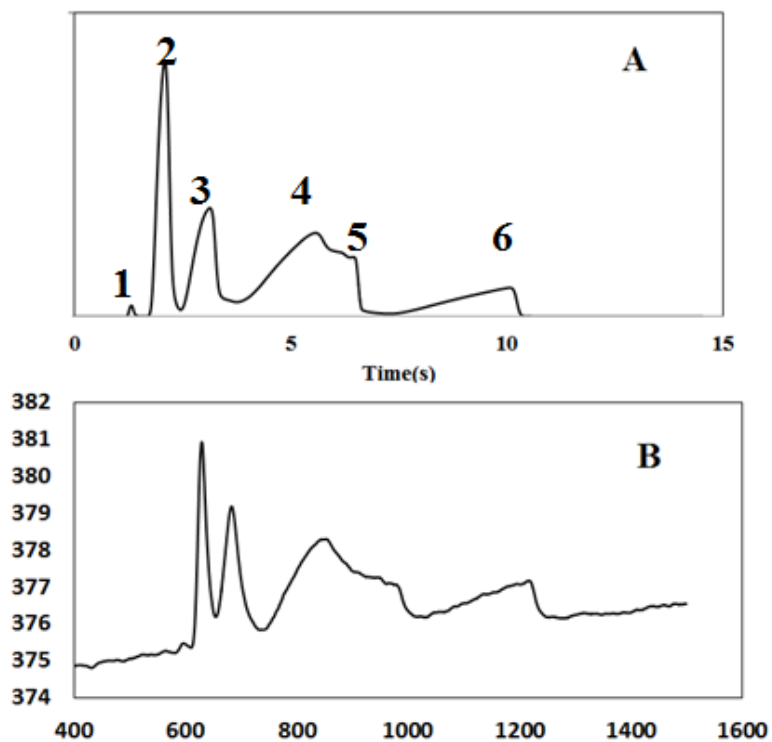


Figure 5-9: FID responses, B) TCD responses

### 5.3 Summary

A novel polysilicon microTCD was developed and tested with a previously fabricated micro GC column. The designed TCD has an ultra-fast response time and is highly sensitive. These features make the sensor suitable for portable GC applications. The TCD performance in different flow rates reveals that the sensor response is independent of the flow rate. At the end, the performance of the TCD system was compared to a commercially available FID detector. The microTCD detection performance was comparable with that of the more complex standard FID, despite being low power, lower cost and less complex.

## Chapter 6 DETECTION OF *ARMILLARIA*

### 6.1 Introduction

Armillaria root rot, caused by *Armillaria tabescens*, is a root disease that arises on a variety of forests and is the number one cause of the peach tree decline in the southeastern United States. There are a few species of *Armillaria*, and several species are pathogenic. As a forest pathogen, *Armillaria* can be extremely destructive. Every year, millions of dollars are lost to *Armillaria* root rot caused by *Armillaria tabescens*. Early detection of the pathogen's presence and the stage of the disease are vital in preventing mortality of the trees. A study by Beckman [68] reveals that a site with a known history of *Armillaria* root rot (ARP) increases the chance of peach tree mortality by 35%.



Figure 6-1: Infected tree with *Armillaria*

Despite the magnitude of this disease, there is limited information available about the non-visual methods of detection of *Armillaria*. Finding the metabolic compounds commonly released by the plant infected with pathogenic species of *Armillaria* and comparing the

results with the agar sample will help pathologists better understand the progress of the infection, to innovate better treatments.

We will use a GC-MS system to experimentally identify the VOC gases commonly released by *Armillaria* and to compare the data with the agar. First, the overhead space of the vial with the agar and the inoculated agar with *Armillaria* will be collected and identified using a standard GC-MS instrument. Next, a mixture of the identified VOC will be mixed and injected into the MEMS system using a standard GC system injector.

## **6.2 *Armillaria* Sample Preparation**

Inoculated *Armillaria tabescens* in the growth medium, along with the growth medium as background check were prepared and inoculated by USDA's Southeastern Fruit and Tree Nut Research facility in Byron, Ga. The well cultivated samples were shipped to GTRI for headspace VOC analysis using the purge and trap GC/MS system (Agilent and Teledyne Tekmar). The EPA 8260C method was used to analyze the headspace VOC of both the inoculated *Armillaria tabescens* and the growth medium.

## **6.3 Gas chromatography-mass Spectrometry (GC-MS) Sampling**

The GC/MS based method currently is the gold standard for VOC analysis. It contains a gas chromatography based separation and mass spectroscopy based compound identification. The method is very sensitive with a detection limit of sub particle per billion or ppb. However, this instrument is expensive, bulky, not portable, and requires a technician's assistant to operate. The following two concentration methods were used,

1) The purge and trap concentration before gas chromatography-mass spectrometry (GC-MS) is one of the most common techniques used worldwide to determine volatile organic compounds (VOCs) by following EPA method 8260C. This method outlines the analysis of volatile organic compounds in a variety of solid waste matrices, including various air sampling trapping media, ground and surface water, soils, and sediments among others.

## 2) Solid Phase Microextraction (SPME)

Our experimental set-up includes:

- Tekmar Atomx (Teledyne Tekmar, Mason, OH) automated VOC Sample Pre System (comprising an integrated 80-position Autosampler and purge and trap).
- Agilent 6850 Gas Chromatography with 5975 Series MSD Pre-cultured samples in 20 ml vial (Agar and Inoculated *Armillaria* on Agar from USDA) are placed directly in the purge and trap 80-position Autosampler.

The purge and trap conditions are presented in Table 6-1

Table 6-1: Purge and trap setup conditions

Purge and Trap system	Tekmar-Atomax
Trap	Tekmar #9 trap
Sample Size	5 mL
Mass Flow	10ml/min
Pressure	0.8 psig
Syringe	10 µl
Transfer Line	140 °C
Oven	140 °C
Mount	90 °C
Trap	Ambient
Sample Vial	40 °C
Condenser	Ambient
Soil Valve	100 °C
Water	90 °C

The GC system was fitted for DB-624 stationary phase (25 X 0.2 X 1.12 µm). This column is specially designed for the analysis of volatile and residual solvents. Helium was used as the carrier gas with 35.9 mL/min in a constant flow mode. The injection temperature and GC transfer line temperature were set to 220 °C, and auto sampler was used to perform the injection. The MS 5975 detector acquisition parameters were set as follows: transfer line at 220 °C, detector was at 230 °C. Detection was achieved in a full scan model from  $\frac{m}{z}$  30-350.

Solid Phase Microextraction (SPME) is a solvent-free sample pre-concentration method and uses a fiber coated with an absorbent polymer. The SPME can be used to inject the sample directly into the GC System. Two SPME Fiber 7 µm PDMS, 24 gauge were used to pre-concentrate the sample for 24 hours as shown in Figure 6-2

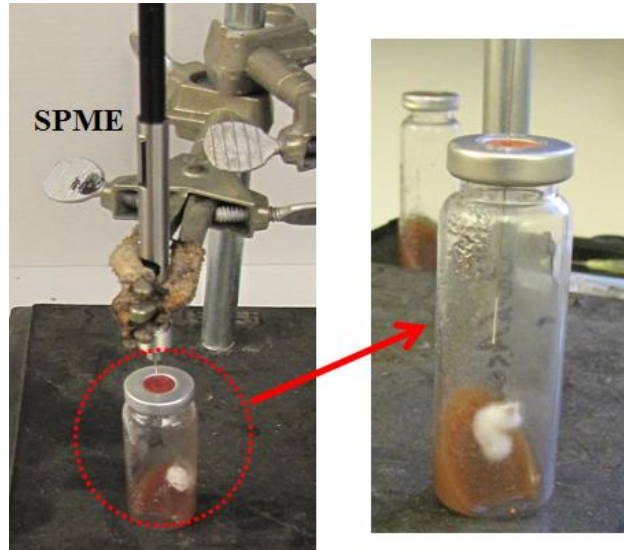


Figure 6-2: SPME adsorbent station

#### 6.4 Experimental setup:

The inoculated *Armillaria tabescens* in the growth medium (Figure 6-2) along with the background growth medium were placed in two vials. The over-head space gases of the two samples were collected and measured using the described GC-MS method.

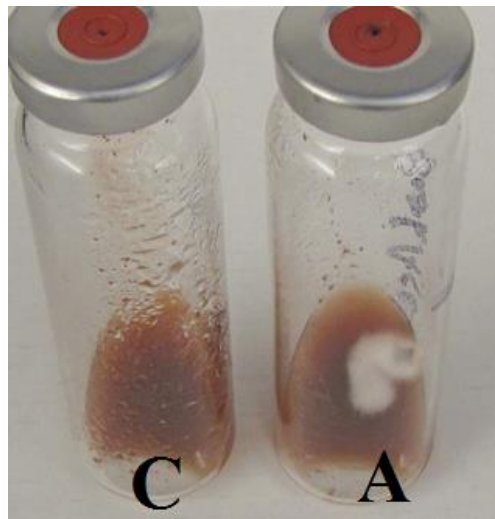


Figure 6-3: A) Inoculated *Armillaria* sample C) agar sample

The overhead space of the two samples were collected for 24 hours and measured once a day for four days and plotted in Figure 6-4 using the SPME setup.

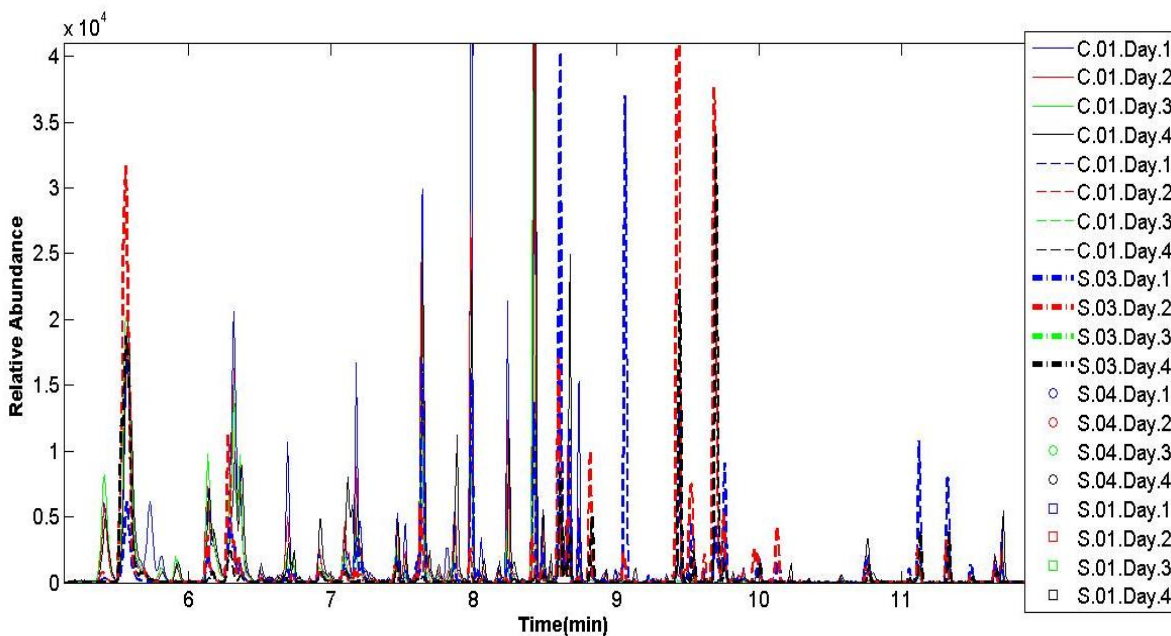


Figure 6-4: Raw data collected for 4 days of sample and control

The data collected using SPME was not conclusive due to improper use of SPME and further experiments are necessary to improve the method of collecting the VOCs.

Therefore, the purge and trap method was used next to identify the VOCs. Obtained Chromatograms of VOCs from both the headspace samples of inoculated *Armillaria* culture and the agar nutrient medium are listed in Figure 6-5.

## VOC of Inoculated *Armillaria* and Agar

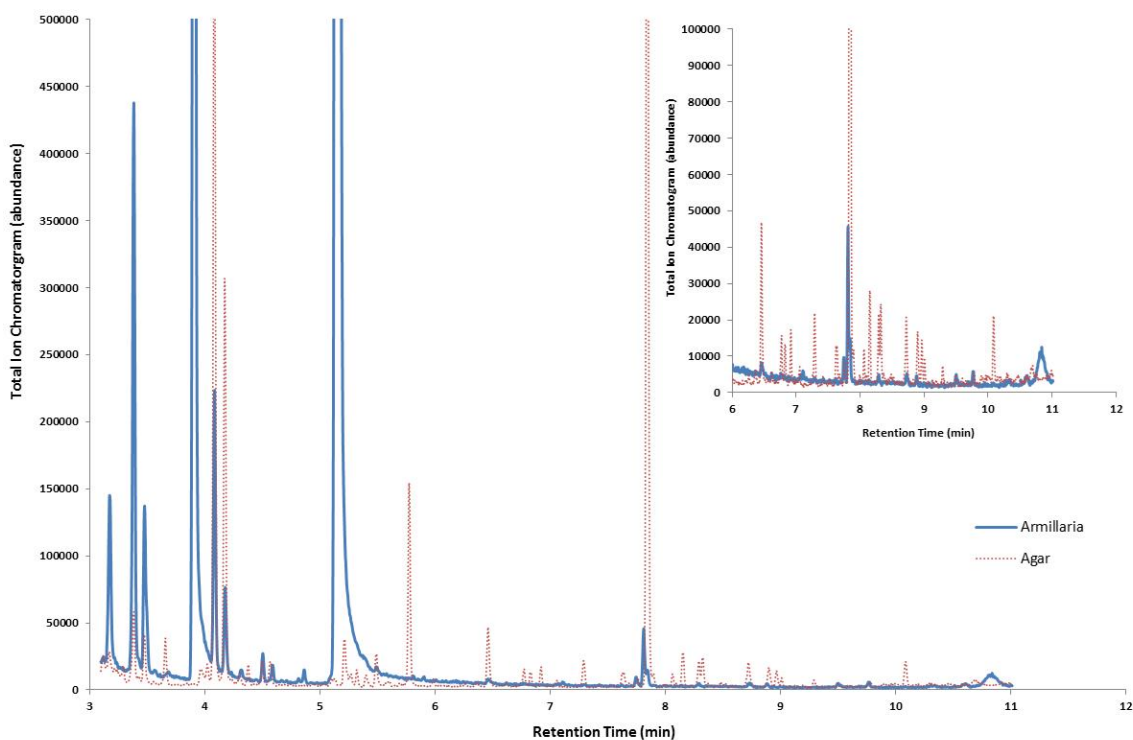


Figure 6-5: Chromatograms comparison for the inoculated *Armillaria* culture and the Agar nutrient media.

After collecting the data, a spectrometric identification library (NIST) was used to identify the compounds based on their retention time. However, the isomeric conjugates are not discernable by mass spectrometry. Therefore, to enhance the reliability of identification, we added several standards with different Kovats indices to the mixture.

Table 6-2: Mixture compounds

NO	Compound	Boiling point	Kovats Indices
1	Pentane	36	500
2	Acetone	57	503
3	Hexane	68	600
4	Benzene	80	662
5	1-Butanol	118	665
6	2-Pentanone	103	686
7	3-Pentanone	101	687
8	Heptane	98	700
9	1-Nitropropane	131	712
10	3-Methyl-butanol	131	732
11	Pyridine	115	746
12	Toluene	111	769
13	Octane	126	800
14	Nonane	151	900
15	Benzaldehyde	178	936
16	1-Octen-3-ol	174	979
17	3-Octanone	167	988
18	Decane	174	1000
19	Undecane	195	1100
20	Naphthalene	195	1100
21	Dodecane	216	1200

## 6.5 System Integration

Here we present a fully integrated GC system for separation and detection of the VOC gases released by *Armillaria* fungus. The schematic of the analytical system prototype is shown in Figure 6-6.

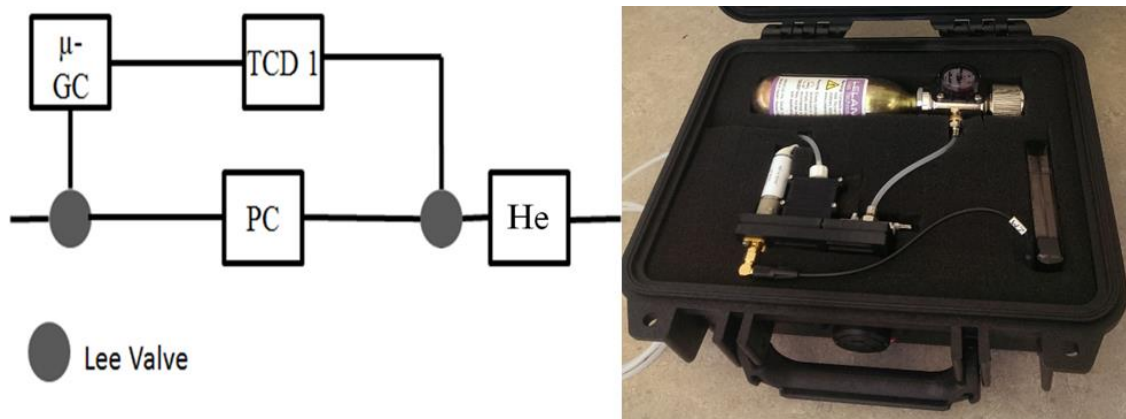


Figure 6-6: (A) Schematic diagram showing the key components of the proposed MEMS-GC system and the innovation. (B) Photograph of MEMS-GC system components.

The components of the system are as follow: micro GC column, thermal conductivity sensor, helium tank as the carrier gas, and two 3-way Lee valves.

After validating each individual component of the GC system, a mixture of twenty-one compounds presented in Table 6-2 was prepared and injected into the system. The performance of the GC column was examined to explore the separation capabilities of the GC system for the mixture components diluted in hexane. The chromatograph of the twenty one compounds was achieved by injecting 0.2  $\mu\text{l}$  of the mixture at 8.06 psi and inlet temperature of 240  $^{\circ}\text{C}$  and temperature at 80  $^{\circ}\text{C}$  and ramp rate 10  $^{\circ}\text{C}$  /min. Figure 6-7 shows the chromatograms achieved using the 3 meter MEMS column.

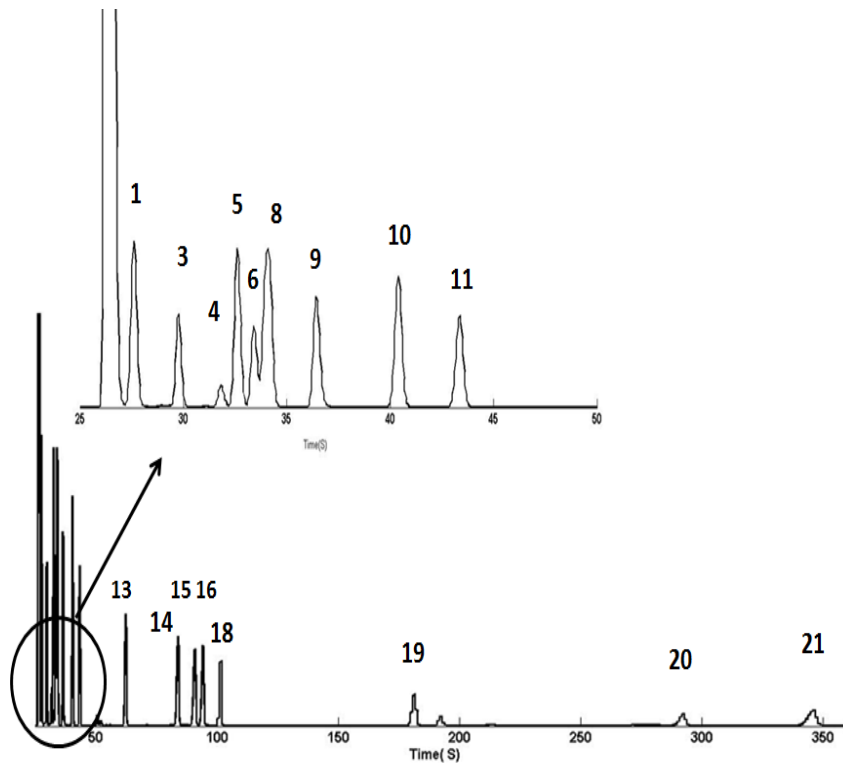


Figure 6-7: Chromatograph achieved using the 3-meter column at 8.06 psi and inlet temperature of 240 °C and temperature at 80 °C and ramp rate 10 C/min

As discussed earlier, it is highly challenging to measure all the VOC gases of *Armillaria* due to a metabolic pathway and similarity of the thermal conductivity of the compounds; therefore, identifying the VOCs correlated to the fungus is very important.

## 6.6 Summary:

This chapter described an innovative portable MEMS gas chromatography column for detection of the VOC gases released by *Armillaria*. Initially, a GC-MS system was used to

identify the VOCs gases associated with *Armillaria* fungi, followed by integration of an all silicon micro-GC column with a novel axial heating technique. The MEMS GC was interconnected with an ultra-low power thermal conductivity Nano sensor for rapid separation and detection of the VOC gases released by *Armillaria* fungus.

## Chapter 7

### CONCLUDING REMARKS

#### 7.1 Conclusions

An innovative portable MEMS gas chromatography system was introduced and discussed for detection of the VOC gases released by *Armillaria* fungus. First, a new micro-fabrication method was developed for fabrication of all silicon 3-meter gas columns with a novel bonding technique. This bonding technique was used to properly seal the column to withstand the temperature cycling required for temperature programming and to decrease degradation over time. This method eliminates the need for anodic bonding of the GC channels, and provides a better temperature uniformity when operated at a higher temperature. Second, we validated the bonding quality by shear force measurement, SEM, EDX and, a butane test at different pressure levels.

To improve the quality of the peaks and ultimately the performance of the overall system, a novel two dimensional axial heating technique was introduced. This heating technique demonstrated a faster and more precise temperature programming in time and distance along the length of the column. Three different axial resistive heater designs were simulated theoretically on a 3.0 m×300 μm×50 μm column to demonstrate the highest temperature gradient on a 22 by 22 μm silicon column. Then, the best design that had the highest temperature gradient was micro-fabricated and evaluated experimentally. The simulation results show that simultaneous temperature gradients in time and distance along the column are possible by geometric optimization of the heater when using forced convection. The gradients along the column continuously refocus the eluting bands, while

offsetting part of the chromatographic band spreading. The results obtained provide a 40° C gradient from the center to the edge of the column. The utility of this method was further investigated for separation of four hydrocarbons C<sub>6</sub>-C<sub>10</sub>.

The GC column was then interconnected with an ultra-low power TCD sensor. The TCD sensors are based on CMOS compatible batch fabrication processes that allow highly reliable sensors to be commercially produced in large numbers and at low cost. A new measurement technique was developed to give optimum sensitivity and minimum power consumption for the sensor. There was a demonstration of an ultra-low power TCD sensor that is independent of the flow rate and that was tested at different pressure levels. The complete system was evaluated for separation of a 6 complex compounds sample.

Finally a GC-MS system was used to identify the VOCs gases associated with *Armillaria* fungi, followed by integration of the all silicon micro-GC column with an ultra-low power thermal conductivity detector for rapid separation and detection of the VOC gases released by *Armillaria* fungus. At the end, the utility of the GC column was demonstrated by separating a mixture of complex compounds.

## 7.2 Recommended future work

In this research, an ultra-low power GC system with an advance embedded 2 dimensional heating element was developed and integrated with an ultra-low power TCD nanosensor for detection of VOC gases released by *Armillaria*. However, there is still some room for improvement. The recommendations for future work are these:

a) Column efficiency needs to be improved by manipulating the coating of the stationary phase. The thickness and uniformity of the stationary phase play an important role in the overall column resolution. Therefore, a proper study of the stationary phase coating of the column with different cross-sectional geometry would be beneficial. We suggest taking advantage of the newly developed advance materials such as MOF and nanotube materials that have a high surface to volume ration to improve the separation performance of the stationary phase.

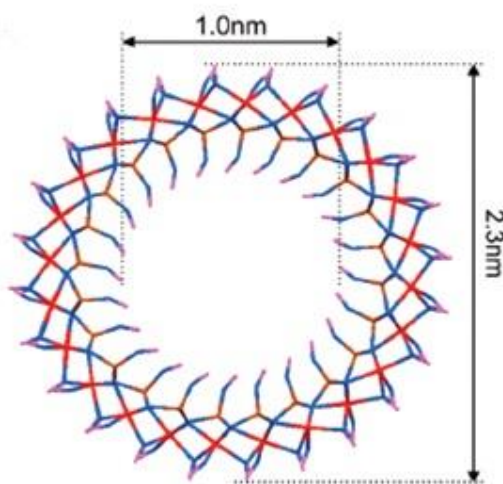


Figure 7-1: Nanotube structure

b) Fabricating a high yield silicon MEMS GC column is very critical to reduce cost. To improve the yield, several shorter columns could be interconnected to make a longer column that could be used for separation of a sample having more complex mixtures.

c) The impact of the axial heating technique is compound specific; therefore, a sequence of compounds with similar Kovat indices should be tested using this method to study the effectiveness of the heating method for more complex samples.

d) Improving the temperature control of the column to enable it to reach higher temperatures during the temperature ramping, and demonstrating separations of other mixtures relevant to environmental sensing and food safety

e) The current TCD sensitivity could be enhanced by employing several Chemoresistors. One of the main advantages of the TCD sensor is its nondestructive detection method; therefore, different sensors could be used in series to enhance the sensitivity.

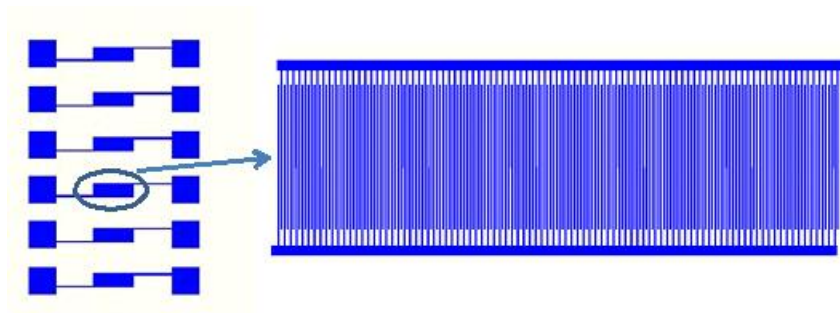


Figure 7-2: Chemiresistor sensors with 4 μm spacing

f) The current setup does not have a fixed pre-concentrator. In order to improve the detection limit of the GC system, a pre-concentrator is necessary to increase the VOC concentration level to a level that is detectable by the TCD sensor. Also, the detection limit of the micro-TCD could be improved by improving the packaging designs. The TCD needs to be installed directly in the direction of the flow stream to provide sharper peaks.

g) Implementation of a jet cooling system would improve the axial temperature profile on the chip. By integrating a helium inlet at the center of the column, a higher convection coefficient will be generated which results in a better temperature gradient.

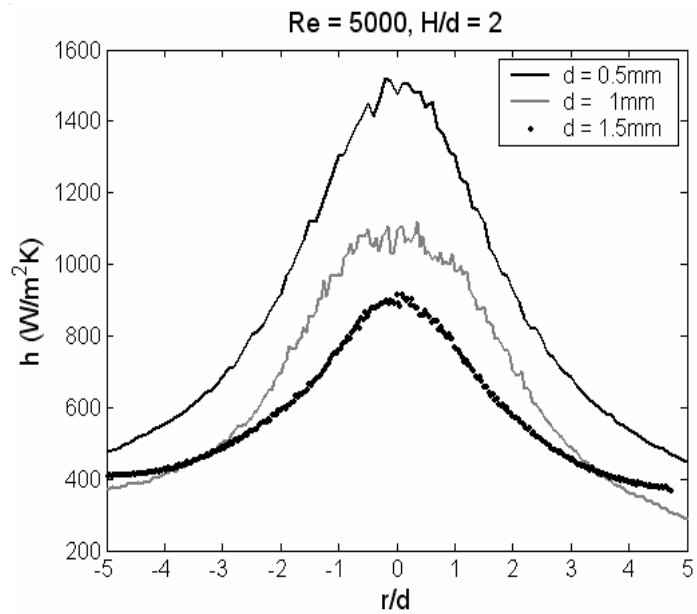
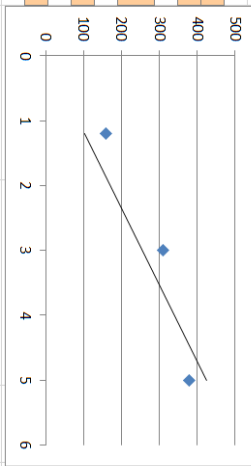


Figure 7-3: convection coefficient as a function of radius

# APPENDIX A: WAFER PROCESSING RUN SHEET FOR THE MEMS GC WAFERS

		RPM	Ramp/s	Time	Thickness Measured
<b>Resist</b>	Resist Adhesion Assist P-20	2000	500	50	
	Shipley SPR-220-7	2000	500	50	
	Pre Bake	3 min	120C		
	Thickness				
<b>Mask Aligner</b>	Alignment Gap:	50um			
	Contact Type:	Hard Contact			
	Expo Time( line 365)	Thickness/ Flux	108.5744286	Film Thickness	Photospeed(mJ/cm²)
			1.2	160	0.45
			3	310	0.9
			5	380	0.9
	<b>HOLD TIME</b>	35 min			
<b>Post Exposure Process</b>	PE Bake	3 min	110C		
	Development Time	4min	500 mL MF-319		
	Hard Bake:	10 min	110 C		



## REFERENCES

1. Guglielmo, F., et al., *A multiplex PCR-based method for the detection and early identification of wood rotting fungi in standing trees*. Journal of Applied Microbiology, 2007. **103**(5): p. 1490-1507.
2. Navaei, M., et al., *Lateral Flow Impedance Transducer for Salmonella Detection*. ECS Transactions, 2011. **35**(35): p. 27-34.
3. Mahdaviifar, A., et al., *A Nitrocellulose-based microfluidic device for generation of concentration gradients and study of bacterial chemotaxis*. Journal of The Electrochemical Society, 2014. **161**(2): p. B3064-B3070.
4. López, M., et al., *Innovative tools for detection of plant pathogenic viruses and bacteria*. International Microbiology, 2003. **6**(4): p. 233-243.
5. Bahnweg, G., et al., *DNA Isolation from Recalcitrant Materials Such as Tree Roots, Bark, and Forest Soil for the Detection of Fungal Pathogens by Polymerase Chain Reaction*. Analytical Biochemistry, 1998. **262**(1): p. 79-82.
6. *Molecular biology of the cell, 3rd ed., by Alberts et al., Garland Publishing, New York, 1994, 1,294 pp + glossary & index, \$59.95*. Molecular Reproduction and Development, 1994. **38**(4): p. 459-459.
7. Desjardin, D.E., A.G. Oliveira, and C.V. Stevani, *Fungi bioluminescence revisited*. Photochemical & Photobiological Sciences, 2008. **7**(2): p. 170-182.
8. Vydryakova, G., A. Gusev, and S. Medvedeva, *Effect of organic and inorganic toxic compounds on luminescence of luminous fungi*. Applied Biochemistry and Microbiology, 2011. **47**(3): p. 293-297.

9. Weitz, H.J., et al., *The effect of culture conditions on the mycelial growth and luminescence of naturally bioluminescent fungi*. FEMS Microbiology Letters, 2001. **202**(2): p. 165-170.
10. Isidorov, V., et al., *Gas chromatographic–mass spectrometric investigation of metabolites from the needles and roots of pine seedlings at early stages of pathogenic fungi *Armillaria ostoyae* attack*. Trees, 2008. **22**(4): p. 531-542.
11. Rock, F., N. Barsan, and U. Weimar, *Electronic Nose: Current Status and Future Trends*. Chemical Reviews, 2008. **108**(2): p. 705-725.
12. Lieberzeit, P. and F. Dickert, *Sensor technology and its application in environmental analysis*. Analytical And Bioanalytical Chemistry, 2007. **387**(1): p. 237-247.
13. Abraham, B.G. and R.G. Berger, *Higher Fungi for Generating Aroma Components through Novel Biotechnologies*. Journal of Agricultural and Food Chemistry, 1994. **42**(10): p. 2344-2348.
14. Terry, S.C., J.H. Jerman, and J.B. Angell, *A gas chromatographic air analyzer fabricated on a silicon wafer*. Electron Devices, IEEE Transactions on, 1979. **26**(12): p. 1880-1886.
15. Reston, R.R. and E.S. Kolesar, *Silicon-micromachined gas chromatography system used to separate and detect ammonia and nitrogen dioxide. I. Design, fabrication, and integration of the gas chromatography system*. Microelectromechanical Systems, Journal of, 1994. **3**(4): p. 134-146.
16. Lu, C.-J., et al., *First-generation hybrid MEMS gas chromatograph*. Lab on a Chip, 2005. **5**(10): p. 1123-1131.

17. Garg, A., et al., *Zebra GC: A mini gas chromatography system for trace-level determination of hazardous air pollutants*. *Sensors and Actuators B: Chemical*, 2015. **212**(0): p. 145-154.
18. Yamanaka, T., R. Matsumoto, and T. Nakamoto, *Study of recording apple flavor using odor recorder with five components*. *Sensors and Actuators B: Chemical*, 2003. **89**(1-2): p. 112-119.
19. Albert, K.J., et al., *Optical Multibead Arrays for Simple and Complex Odor Discrimination*. *Analytical Chemistry*, 2001. **73**(11): p. 2501-2508.
20. Serrano, G., T. Sukaew, and E.T. Zellers, *Hybrid preconcentrator/focuser module for determinations of explosive marker compounds with a micro-scale gas chromatograph*. *Journal of Chromatography A*, 2013. **1279**(0): p. 76-85.
21. Zhao, H., et al., *Characteristics of TGPGC on Short Micro Packed Capillary Column*. *Analytical Sciences*, 2002. **18**(1): p. 93-95.
22. Lambertus, G., et al., *Design, Fabrication, and Evaluation of Microfabricated Columns for Gas Chromatography*. *Analytical Chemistry*, 2004. **76**(9): p. 2629-2637.
23. Agah, M., et al., *High-Speed MEMS-Based Gas Chromatography*. *Microelectromechanical Systems, Journal of*, 2006. **15**(5): p. 1371-1378.
24. Reidy, S., et al., *Temperature-Programmed GC Using Silicon Microfabricated Columns with Integrated Heaters and Temperature Sensors*. *Analytical Chemistry*, 2007. **79**(7): p. 2911-2917.

25. Radadia, A.D., et al., *Micromachined GC Columns for Fast Separation of Organophosphonate and Organosulfur Compounds*. Analytical Chemistry, 2008. **80**(11): p. 4087-4094.
26. Radadia, A.D., et al., *The fabrication of all-silicon micro gas chromatography columns using gold diffusion eutectic bonding*. Journal of Micromechanics and Microengineering, 2010. **20**(1): p. 015002.
27. Kim, S.K., H. Chang, and E.T. Zellers, *Microfabricated Gas Chromatograph for the Selective Determination of Trichloroethylene Vapor at Sub-Parts-Per-Billion Concentrations in Complex Mixtures*. Analytical Chemistry, 2011. **83**(18): p. 7198-7206.
28. Li, Y., et al., *Improvement of column efficiency in MEMS-Based gas chromatography column*. RSC Advances, 2014. **4**(8): p. 3742-3747.
29. Haudebourg, R., et al., *Temperature-Programmed Sputtered Micromachined Gas Chromatography Columns: An Approach to Fast Separations in Oilfield Applications*. Analytical Chemistry, 2012. **85**(1): p. 114-120.
30. Navaei, M., *Quartz crystal microbalance adsorption apparatus for high pressure gas adsorption measurements in nanomaterials*. 2011.
31. Hesketh, P., et al., *High-pressure quartz crystal microbalance*. 2014, Google Patents.
32. Venkatasubramanian, A., et al., *Gas Adsorption characteristics of metal-organic frameworks via quartz crystal microbalance techniques*. The Journal of Physical Chemistry C, 2012. **116**(29): p. 15313-15321.

33. Agah, M., et al., *High-performance temperature-programmed microfabricated gas chromatography columns*. *Microelectromechanical Systems, Journal of*, 2005. **14**(5): p. 1039-1050.
34. Zimmermann, S., S. Wischhusen, and J. Mueller. *Micromachined flame ionization detector and flame spectrometer*. 1999.
35. Kuipers, W. and J. Müller, *Sensitivity of a planar micro-flame ionization detector*. *Talanta*, 2010. **82**(5): p. 1674-1679.
36. Kim, J., et al., *Development of a micro-flame ionization detector using a diffusion flame*. *Sensors and Actuators B: Chemical*, 2012. **168**(0): p. 111-117.
37. Chen, C., et al., *A wireless hybrid chemical sensor for detection of environmental volatile organic compounds*. *IEEE sensors journal*, 2013. **13**(5): p. 1748-1755.
38. Zampolli, S., et al., *Real-time monitoring of sub-ppb concentrations of aromatic volatiles with a MEMS-enabled miniaturized gas-chromatograph*. *Sensors and Actuators B: Chemical*, 2009. **141**(1): p. 322-328.
39. Collin, W.R., et al., *Microfabricated Gas Chromatograph for Rapid, Trace-Level Determinations of Gas-Phase Explosive Marker Compounds*. *Analytical Chemistry*, 2014. **86**(1): p. 655-663.
40. James, A. and A. Martin, *Gas-liquid partition chromatography: the separation and micro-estimation of volatile fatty acids from formic acid to dodecanoic acid*. *Biochemical Journal*, 1952. **50**(5): p. 679.
41. MahdaviFar, A., *Direct Numerical Simulation of Flow and Mass Transfer in Spacer-filled Channels*. 2011.

42. Mahdavifar, A., et al., *Wall proximity effects on flow over a simple membrane spacer*. Computers & Fluids, 2013. **88**: p. 180-188.
43. Sinha, A.E., et al., *Comprehensive two-dimensional gas chromatography of volatile and semi-volatile components using a diaphragm valve-based instrument*. Journal of Chromatography A, 2003. **983**(1–2): p. 195-204.
44. Golay, M.J.E., *Theory of Chromatography in Open and Coated Tubular Columns with Round and Rectangular Cross-Sections*. Gas Chromatography, 1958: p. 36-55.
45. Navaei, M., et al. *Micro Gas Chromatography System for detection of Volatile Organic Compounds Released By Fungi*. in *224th ECS Meeting (October 27–November 1, 2013)*. 2013. Ecs.
46. L. Valero, *The fundamentals of eutectic die attach*. Semicond. Int. **7**: p. 236-241.
47. Barth, P.W., *Silicon fusion bonding for fabrication of sensors, actuators and microstructures*. Sensors and Actuators A: Physical, 1990. **23**(1–3): p. 919-926.
48. Navaei, M., et al., *Micro-Fabrication of all Silicon 3 Meter GC Columns using Gold Eutectic Fusion Bonding*. Journal of Electrochemical Society, 2015. **4**(10): p. S3011-S3015.
49. in *CRC Materials Science and Engineering Handbook, Third Edition*. 1997, CRC Press. p. 255.
50. A.A. Zhukhovitskii, O.V.Z., V.A. Sokolov, N.M. Turkel'taub,, *New method of chromatographic analysis*. Dokl. Akad. Nauk SSSR, 1951. **77**: p. 435-438.

51. Jain, V. and J.B. Phillips, *High-Speed Gas Chromatography Using Simultaneous Temperature Gradients in Both Time and Distance along Narrow-Bore Capillary Columns*. Journal of Chromatographic Science, 1995. **33**(11): p. 601-605.
52. Phillips, J.B. and V. Jain, *On-Column Temperature Programming in Gas Chromatography Using Temperature Gradients along the Capillary Column*. Journal of Chromatographic Science, 1995. **33**(10): p. 541-550.
53. MahdaviFar, A., et al., *Simulation and Fabrication of an Ultra-Low Power Miniature Microbridge Thermal Conductivity Gas Sensor*. Journal of The Electrochemical Society, 2014. **161**(4): p. B55-B61.
54. MahdaviFar, A., et al. *Transient Thermal Response of Micro TCD for Identification of Gases*. in *Meeting Abstracts*. 2013. The Electrochemical Society.
55. Butts, D.A. and D. Taarea, *19 - Electrical properties*, in *Smithells Metals Reference Book (Eighth Edition)*, W.F.G.C. Totemeier, Editor. 2004, Butterworth-Heinemann: Oxford. p. 1-10.
56. Stafford, J., et al., *Flat plate heat transfer with impinging axial fan flows*. International Journal of Heat and Mass Transfer, 2010. **53**(25–26): p. 5629-5638.
57. Navaei, M., et al., *All Silicon Gas Chromatographic Column for Fast Separation of VOCs Released By Armillaria Fungus*. Meeting Abstracts, 2015(40): p. 2094-2094.
58. Navaei, M., et al., *All Silicon Micro-GC Column Temperature Programming Using Axial Heating*. Micromachines, 2015. **6**(7): p. 865.
59. Kimura, M., et al., *Application of the air-bridge microheater to gas detection*. Sensors and Actuators B: Chemical, 1995. **25**(1–3): p. 857-860.

60. Zanini, M., et al., *Fabrication and properties of a Si-based high-sensitivity microcalorimetric gas sensor*. *Sensors and Actuators A: Physical*, 1995. **48**(3): p. 187-192.
61. Lysko, J.M., et al. *Silicon thermal conductivity detector (TCD) with the Pt resistors*. 2003.
62. Cruz, D., et al., *Microfabricated thermal conductivity detector for the micro-ChemLab™*. *Sensors and Actuators B: Chemical*, 2007. **121**(2): p. 414-422.
63. V. Khanna, M.P., V. Dwivedi, C. Shekhar, A. Pankaj, and J. Basu., *Design and electro-thermal simulation of a polysilicon microheater on a suspended membrane for use in gas sensing*. *Indian Journal of Pure & Applied Physics* 2007. **45**: p. 332-335.
64. Kaanta, B.C., et al. *High Sensitivity Micro-Thermal Conductivity Detector for Gas Chromatography*. in *Micro Electro Mechanical Systems, 2009. MEMS 2009. IEEE 22nd International Conference on*. 2009.
65. Kaanta, B.C., et al. *A novel thermal conductivity detector capable of flow rate measurements*. in *Sensors, 2010 IEEE*. 2010.
66. Narayanan, S., B. Alfeeli, and M. Agah, *A micro gas chromatography chip with an embedded non-cascaded thermal conductivity detector*. *Procedia Engineering*, 2010. **5**(0): p. 29-32.
67. Mahdavifar, A., et al., *Transient Thermal Response of Micro TCD for Identification of Gases*. *Meeting Abstracts*, 2013(50): p. 2795-2795.
68. Beckman, T.G., et al., *Relative susceptibility of peach and plum germplasm to Armillaria root rot*. *Hortscience*, 1998. **33**(6): p. 1062-1065.